THE EFFECTS OF HARDNESS, TOUGHNESS, MICROSTRUCTURE AND THERMOMECHANICAL HEATING ON THE EROSION OF CERAMIC AND ULTRAHARD MATERIALS

by

R A VAUGHAN

A thesis submitted to the Faculty of Engineering, University of Cape Town, in fulfillment of the Degree of Master of Applied Science.

December 1991

Department of Materials Engineering

ACKNOWLEDGEMENTS

I wish to thank all my friends and colleagues who have assisted me during the course of this work. In particular I would like to mention the following people:-

Professor A Ball, my supervisor, for his untiring encouragement and support.

Mrs T Tintinger and Miss K Botha for their assistance with the manuscript.

Messrs B Greeves and J Petersen for the photographic work.

Messrs N Dreze, D Dean, G Newins and R Hendricks for their help with mechanical problems.

I also want to thank my fellow students for their interest and advice, with special thanks to C Lang and S Wilson.

Finally, I am grateful to the De Beers Diamond Research Laboratories and Dr R Caveney for their sponsorship and the Structural Ceramics Group at the Division of Materials Science and Technology of the CSIR for providing specimens.

ABSTRACT

Nine different ceramic and ultrahard materials have been eroded by four different erodents under standardised experimental conditions. The target materials range from the soft stabilised zirconias to the very hard polycrystalline diamond composites. The four erodent particles used were: soft, friable silica, sharp alumina, tough silicon carbide and very hard, synthetic industrial diamonds.

The steady state erosion rates of the different target/erodent combinations were measured. The erosion for each combination was studied by examining the target surfaces at progressive stages of erosion and the erodent particles after impact. Special attention has been paid to the morphology of impact sites, the amount of material lost and the mechanisms of erosion.

The ceramic materials eroded by an elastic/plastic process: irreversible deformation is followed by lateral fracture. The ultrahard materials erode by a complex process involving deformation and extrusion of the softer phases and fracture and loss of the harder crystallites.

The relative hardness of the target and erodent is a determining factor in erosion. When the hardnesses are similar, the ease of initiation and propagation of lateral fracture determines the rate of material removal. When the erodent particles are much harder than the target material, initiation of fracture is inevitable and the ease of crack propagation determines the rate of material removal. This is controlled by the sharpness of the particles and the microtoughness of the target material. The microtoughness is a function of grain size, porosity and defect density.

Melting features, seen in many of the eroded surfaces, are thought to arise from a combination of plastic deformation and frictional heating under high contact stresses. The amount of heat dissipated is determined by the erodent and target hardness and friction coefficients. The rate at which the heat diffuses away from the impact zone is determined by the thermal diffusivities, heat capacities and densities of the target and the erodent.

NOMENCLATURE

a	Contact area
A16	Alumina grade 16
A17	Alumina grade 17
AlN	Aluminium nitride
BN	Boron nitride
Br	Brittle
BSE	Backscattered Electrons
c	Cubic
C	Heat Capacity
CBN	Cubic boron nitride
d	Sliding distance
E	Young's Modulus
EDS	Energy Dispersive Spectroscopy
F	Particle flux
fr	Fracture
HCP	Hexagonal close packed
H_e	Erodent Hardness
hip	Hot isostatic pressing
H_t	Target Hardness
k	Thermal diffusivity
K_c	Toughness/stress intensity factor
KE	Kinetic energy
m	Monoclinic
m	Mass
MgPSZ	Magnesia partially stabilised zirconia
P	Indentation pressure
PCBN	Polycrystalline cubic boron nitride
PCD	Polycrystalline diamond
P_E	Elastic loading pressure
Pl	Plastic
r	Particle radius
R	Alumina grade RCHPDBM
SEM	Scanning Electron Microscopy
SPE	Solid Particle Erosion
t	Tetragonal

t ..... Time
T ..... Temperature
t_c ..... Contact time
t_E ..... Elastic loading time
T_m ..... Melting temperature
TZP ..... Tetragonal zirconia polycrystals
V ..... Velocity
w ..... Feed rate
W_f ..... Frictional work
x_d ..... Thermal diffusion distance
x_p ..... Plastic zone size
Y ..... Yield stress
YAG ..... Yttrium aluminium garnet
ρ ..... Density
ΔT ..... Temperature rise
ϵ ..... Strain rate
μm ..... Micrometer
ν ..... Poissons Ratio

CONTENTS

CHAPTER ONE: INTRODUCTION

The word erosion is derived from the Latin word "rodere - to gnaw" and may be used to describe a number of destructive processes that result in material loss and property degradation of exposed surfaces (1). Erosion is encountered in the weathering of rocks and soil by wind, water and ice, the damage of aircraft by rain, hail and dust, material removal by liquid cavitation in pipes, and the loss of material from a surface due to the impingement of solid particles entrained in a fluid medium. The latter, known as solid particle erosion, is the subject of this research.

In many industrial situations the loss of material and decay of mechanical properties due to erosive wear of critical components is a factor which significantly decreases the lifetime and efficiency of machinery. The development of materials with an increased erosion resistance would therefore be of great benefit to industry and mankind.

Erosion can be very destructive. One third of all tube failures in coal-fired boilers, fluidised beds, geothermal and magnetohydrodynamic power systems are the result of erosion damage due to the action of impinging ash particles (2). The ingestion of dust clouds can reduce the lifetime of helicopter engines by as much as 90% (3). In pneumatic transport of materials through pipes, erosive wear at bends can be fifty times higher than in straight sections (4). Other diverse cases include the wearing of rocket motor tail valves (5), gas turbine blades (4), and boiler tubes exposed to fly ash (6). Erosion may be put to good use, for example, in sand blasting, abrasive deburring and erosive drilling of hard materials.

Ceramic materials, considered for their high wear resistance, generally have low toughnesses. Erosion can create surface flaws and cause small changes in the geometry of a component which may be critical where precise geometries are required, for example in poppet valves. This may ultimately cause premature failure and system downtime.

A better understanding of the processes that occur during the erosion of ceramics and the factors that control erosion could result in the design of materials with improved wear resistance and this, in conjunction with advanced design configuration, would result in the optimisation of materials usage.

This study involves a systematic approach to the effect of target hardness and toughness on the mode and rate of erosion in ceramic and ultrahard materials. Special attention has been given to the effect of the microstructure of the target materials and the properties of erodent particles and the thermomechanical effects of erosion.

The target materials were selected on the basis of their wide range of mechanical, physical and microstructural properties. Briefly they consist of :-

(i) three grain sizes of high density, sintered, polycrystalline alumina, namely R, A16 and A17

(ii) partially stabilised zirconia doped with approximately 10% magnesia (MgPSZ)

(iii) fully stabilised tetragonal zirconia polycrystals (TZP) containing 3% yttria dopant

(iv) Sialon ceramic, Syalon 501, supplied by Lucas Cookson Research

(v) two modifications of polycrystalline diamond (PCD), trade name Syndite, supplied by the De Beers Diamond Research Laboratories. The two samples differ in the size of the diamond polycrystals prior to sintering. The nominal pre-sintering sizes were 2 microns, (Syndite 002), and 25 microns, (Syndite 025)

(vi) polycrystalline boron nitride (PCBN), trade name Amborite, supplied by the De Beers Diamond Research Laboratories.

These materials are described in Chapter Four in terms of development, microstructural features, porosity, hardness and toughness. The erodent particles are also characterised in Chapter Four.

CHAPTER TWO: LITERATURE REVIEW

2.1 DEFINITIONS

Solid particle erosion is described as the progressive loss of original material from a solid surface due to mechanical interaction between that surface and impinging solid particles (7). Impingement is defined as a process resulting in a continuing succession of impacts between particles and a solid surface.

A virgin surface is one that has not yet been eroded, and an eroded surface is one that has any number of impacts on it. The erosion rate is defined as the mass or volume loss of a material per gram of erodent. A particle stream consists of particles entrained in a moving column of air. The nominal impact angle is the angle between the target surface and the particle stream. An impact site may be defined as a depression or region of damage on a surface as a result of impact, the entrance side of the impact being the side at which the tip of the particle first enters the target surface and the exit side being the side from which the particle leaves.

2.2 MODES OF EROSION

Erosion may be broadly divided into two categories: ductile erosion, involving the removal of material by plastic deformation and brittle erosion involving the removal of material by fracture processes.

DUCTILE EROSION

The erosion of soft, tough materials is predominantly ductile and may be separated into two major processes: cutting wear due to glancing impact and extrusion and fragmentation due to normal impact. In reality, ductile erosion may occur by a combination of different processes.

Cutting wear

Ductile erosion is low for normal impact and reaches a maximum for glancing impact. Finnie (8) proposed a theory for cutting wear involving chip formation and removal by the machining action of impacting particles (fig. 2.1). He assumed that the particles remained intact after impact and the particles left the target surface

when their perpendicular velocity was zero. Finnie's theory correlates well for low angle/glancing erosion but estimates zero erosion for normal impact.

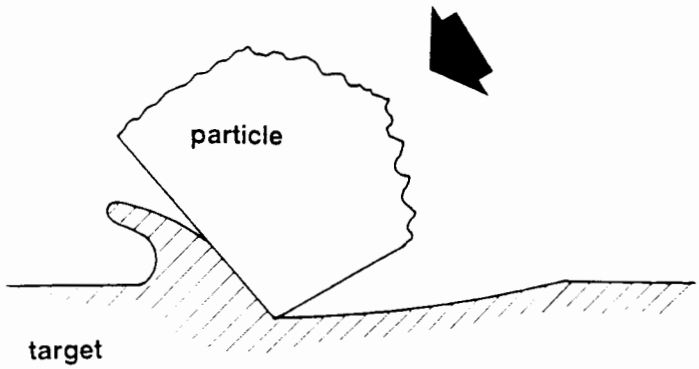

Figure 2.1 *A schematic diagram of Finnie's theory of cutting wear (after Finnie (8)).*

Bitter (9) considered the energy balance and extended his analysis to include brittle and ductile erosion for the same material. Thus the erosion not accounted for by Finnie was said to occur by a brittle process.

Bitter's approach was later simplified by Neilson and Gilchrist (5) who arrived at an easily adjustable erosion term based on brittle cracking and ductile cutting. The equations correlated well with impact angle but wrongly predicted the velocity exponent. Subsequent observations revealed that other forms of erosion do occur.

Extrusion and fragmentation

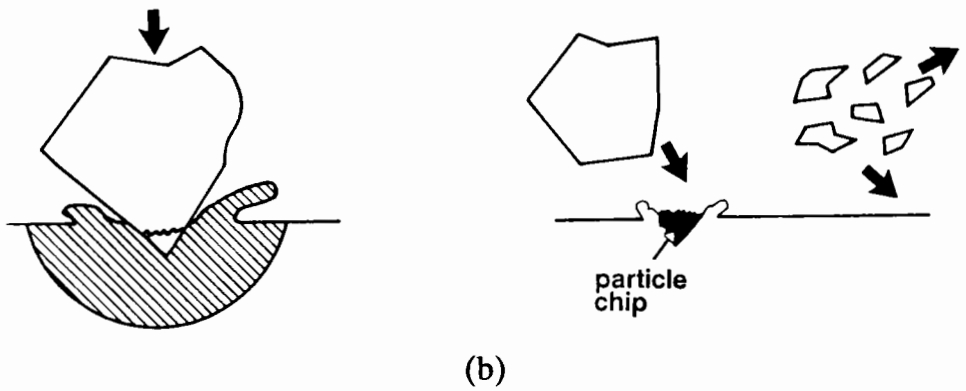

Figure 2.2 *Tilly's two stage mechanism of ductile erosion involving (a) extrusion and lip formation and (b) secondary erosion by particle fragmentation (after Tilly (10)).*

In studying single impact erosion, Tilly (10) noticed that material was extruded to the edge of the damage zone to form lips that were vulnerable to subsequent

impact. He also noted that hard erodent particles often broke up into fragments that scoured the surface. This led to Tilly developing a two stage mechanism of ductile erosion (fig. 2.2) involving a primary stage of extrusion and a secondary stage due to particle fragmentation. He noted that threshold values of velocity and particle size were important. He accepted that other processes take place such as localised melting and chip removal by cutting.

Platelet formation

Levy (11, 12) recently developed a three stage theory of ductile erosion by platelet formation. Initially, an impacting a particle forms a crater with extruded lips, the displaced material is further deformed by subsequent impact and work hardened and, finally, it becomes so severely strained that ductile fracture occurs.

BRITTLE EROSION

Brittle erosion occurs by the formation and intersection of a network of subsurface cracks. In order for material removal to occur the surface stress must reach a critical value to initiate microfracture and the microcracks must propagate in order to release chips of material. It follows from this that for a material to be resistant to brittle erosion it must be tough enough to inhibit crack propagation.

Two major crack systems operate in the brittle regime: blunt particles travelling at low velocities set up Hertzian elastic stresses and sharp particles travelling at high velocities cause inelastic deformation which subsequently causes median/lateral cracking.

Hertzian fracture

Hertzian stresses occur at low strains, under blunt indenters or in amorphous materials, under conditions of essentially elastic loading (8).

Finnie (8) analysed ring crack formation (fig. 2.3) in terms of the Hertzian stresses developed. These stresses have a maximum tensile value at the surface and in radial directions. He suggests that in the early stages of erosion, each impact produces a ring crack which flares out beneath the surface. With further impacts, the cracks interact and fragments of material are removed. Variations of the strike

angle produce Hertzian crack diameters proportional to the normal component of the strike velocity.

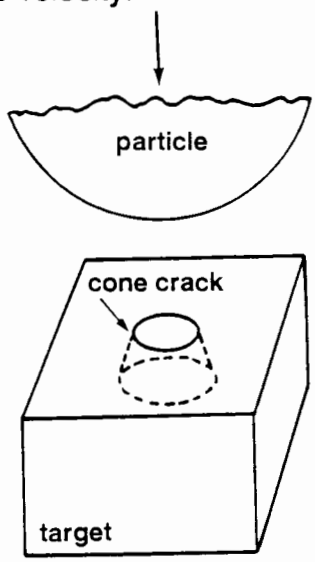

Fig. 2.3 A schematic diagram of erosion by ring and cone crack formation due to elastic of a blunt indenter (after Finnie (8)).

Bitter (9) stated that Hertzian fracture could only occur if the elastic limit was exceeded and that repeated impacts caused work hardening and raised the elastic limit of the material until a stage was reached where the stresses exceeded the strength of the material and cracking occurred. He named this deformation wear.

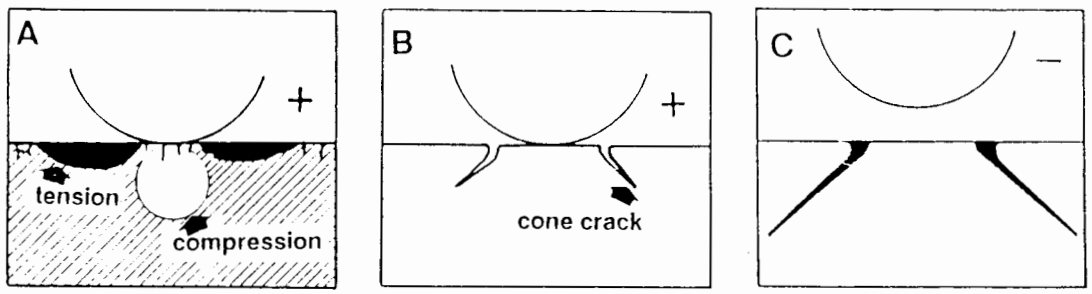

Figure 2.4 *A schematic representation of the stress fields and cracking associated with the loading of a blunt indenter (after Lawn and Marshall (14)).*

The loading cycle for Hertzian indentation is shown in fig. 2.4. On loading, a compressive field is set up directly beneath the indenter and a strong thin tensile surface skin develops outside the contact surface (A). The tensile field expands on further loading and, on reaching a critical Griffith configuration with a surface flaw, initiates a ring crack which runs around the contact area. Further loading causes the tensile stress to accumulate until a major instability is attained and the ring crack spontaneously develops into a Hertzian cone crack (B). On unloading the

cone crack tries to heal but is prevented by mechanical obstruction (C). If the unloading is rapid the cone crack may turn upwards in a hat brim fashion.

The surface finish is very important in determining the load at which ring cracks initiate and ultimately the erosion rates. As erosion proceeds, the ring cracks intersect and chips of material are released.

Median/lateral fracture systems

Sharp particles and/or high particle velocities result in elastic/plastic contact analogous to quasi-static loading of brittle materials by diamond indenters. In this regime either Palmquist or half-penny cracking (fig. 2.5) can occur and dislocation plasticity is experienced below the impact site.

Palmquist cracking occurs in the lower loading regimes when $c/a<2$. The half-penny or median/radial crack system operates in higher loading conditions and in materials with low toughnesses. The median/radial system is thought to dominate in the loading of the ceramics tested during the course of this work.

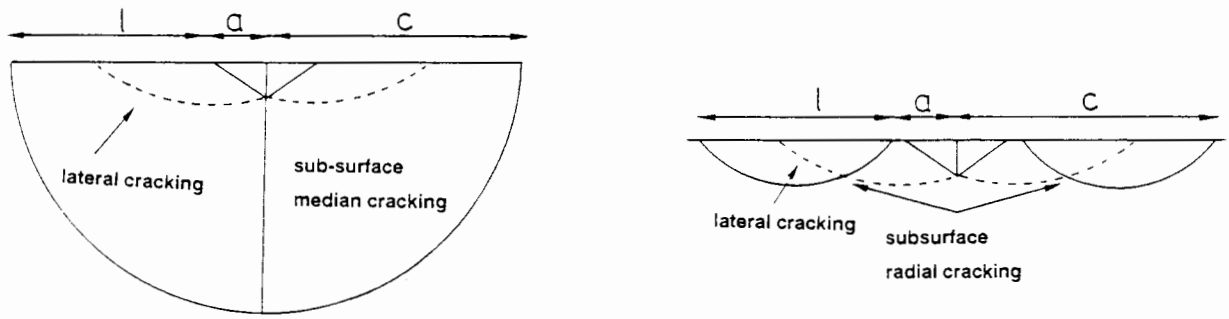

(a) (b)

Figure 2.5 *A schematic representation of the crack systems that result from elastic/plastic indentation by sharp indenters (a) Palmquist cracking and (b) half-penny cracking (after Ponton and Rawlings (13)).*

The indentation loading cycle of a sharp indenter is described by Lawn and Marshall (14) and is shown schematically in fig. 2.6. On loading (A), a plastic field set up beneath the indenter point subjects sub-surface flaws to a yield controlled level of tensile stress. This field grows until it reaches a critical configuration and initiates sub-surface median cracking. On further loading the median cracks propagate downwards, beneath the indenter (B) and upwards to intersect with the

surface and with radial traces from the sharp corners of the indenter. On unloading, the median cracks move together but do not heal.

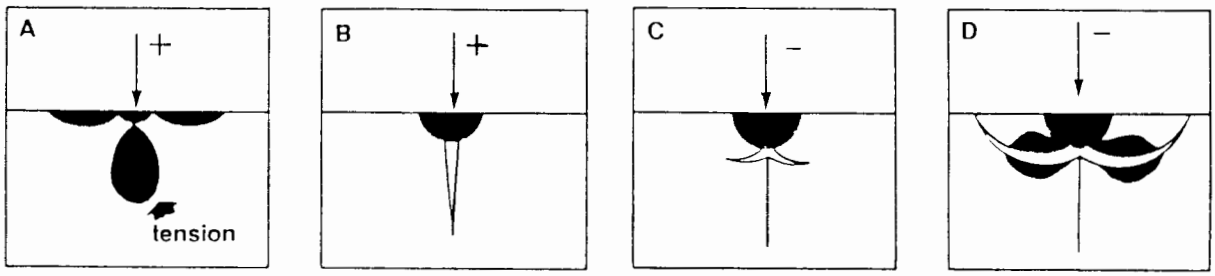

Figure 2.6 *A schematic diagram of the loading cycle under a sharp indenter (after Lawn and Marshall (14)).*

The elastic/plastic field is modified by the residual stress field. On unloading the residual stress begins to dominate and prior to full unloading the residual stress may become sufficient to nucleate lateral cracks at the elastic/plastic interface (C). These cracks propagate parallel to the surface and may intersect with the surface to cause material removal by chipping or spallation. The residual stress field is due to the constraint of the plastic zone as a result of elastic zone relaxation on unloading (D).

Spallation and chipping is the most effective form of material removal in brittle materials and thus it is important to understand the impact conditions that affect initiation and propagation of lateral cracks. Pre-existing flaws are not required for lateral crack initiation as nucleation can occur as a result of highly localised shear deformation beneath a sharp indenter. Impact by blunt particles, or particles prone to blunting, would modify such shear processes and repeated impacts would be required to cause an accumulation of inelastic deformation and subsequent lateral cracking. This would account for threshold effects in particle velocity and particle size and also for the incubation periods often encountered with blunt or soft indenters.

Far field effects, namely the size and velocity of the erodent particles, determine the amount of energy available for the propagation of the lateral cracks. As the initiation of lateral crack in brittle materials is almost inevitable, the most important factor in determining the erosion rate is the resistance to irreversible deformation

and propagation of lateral cracks. Propagation is not affected by particle blunting that affects the near field nucleation.

SUMMARY

A summary of the modes of wear that can operate during solid particle erosion is shown in fig. 2.7. The mode of erosion is very important in determining the amount of material removed during erosion and is dependant on impact conditions, material and particle properties. A combination of mechanisms can operate simultaneously, although in general one may be predominant, under given experimental conditions for a certain target and erodent.

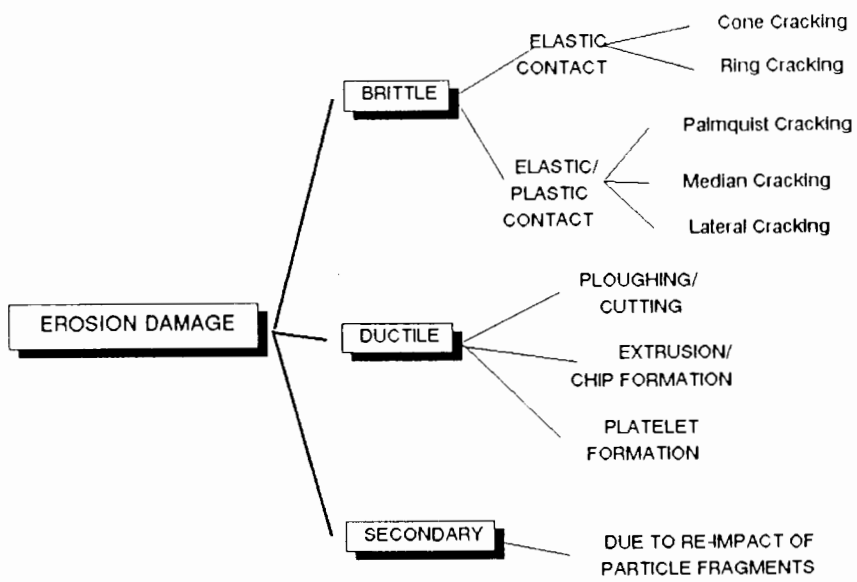

Figure 2.7 *A summary of some of the modes and mechanisms that can operate during erosion.*

2.3 THE ENERGY APPROACH

A moving particle has an inherent kinetic energy due to its mass and velocity. On impact, this energy is apportioned between the target and the particle. The amount of energy transferred to the target surface depends on the impact conditions and the target and particle properties. The energy transferred to the target is expended in elastic and/or plastic deformation fracture and heat. The extent of material lost from the surface will be determined by the mode of damage and the mechanical and thermal properties of the target material. The remaining energy is expended in particle damage and the rebound velocity of the particle and/or fragments. The energy dispersal mechanisms are summarised in fig. 2.8.

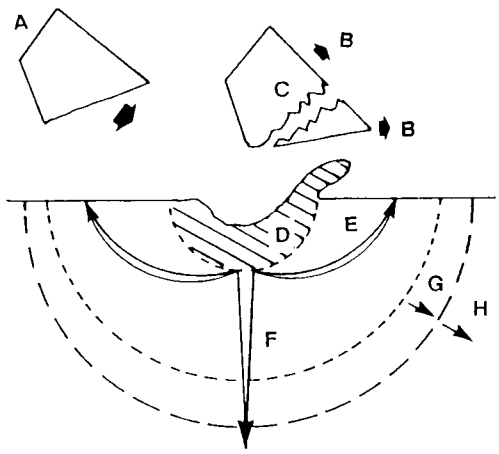

Fig. 2.8 A schematic representation of the possible mechanisms of energy dispersal during particle impact: (A) initial kinetic energy (B) kinetic energy lost in rebound velocity of fragments (C) particle fracture, deformation and/or heating (D) plastic deformation and heating (E) lateral spallation (F) median venting (G) shear wave (H) compressive wave (from Doyle (15)).

Head and Harr (16) concluded in their "model for erosion by natural contaminants" that:-

(i) provided the mode of erosion remains constant, the steady state erosion rate is directly proportional to the energy transmitted to the target.

(ii) a threshold energy must be exceeded before erosion can occur.

(iii) the major factors that influence the transmission of energy are the velocity, shape and hardness of the particles and the hardness and ability of the target to absorb energy.

The damage mode in the target material is important in determining its ability to absorb energy. Plastic deformation is very effective in absorbing energy while brittle fracture requires less energy and tends to result in more extensive material loss. Thus a material's resistance to plastic deformation and fracture is important.

2.4 THERMOMECHANICAL EFFECTS

Melting features, in the form of stringers and tear drops, have been reported for a number of erosion processes (17, 18, 19, 20, 21, 22).

The melting features seen in the impact sites of metals are generally accompanied by large shear lips suggesting that heating is due to adiabatic shear deformation (23). Sudden, severe plastic deformation occurs in a localised region around contact points of an impacting particles resulting in intense local heating. If the plastic zone exceeds the root mean square thermal diffusion distance, then

adiabatic conditions will prevail and melting will occur if the melting point of the material is exceeded (22).

Localised adiabatic heating may cause recovery of strained material which could account for the absence of strain, work hardening and phase transformations in some eroded surfaces.

In addition to this, heating may be the result of the frictional work involved in a particle sliding across the surface of a material on impact resulting in the formation of a glassy viscous phase between the particle and the target surface.

2.5 VARIABLES AFFECTING EROSION

The response of a target material to solid particle erosion is a complicated function of the physical, mechanical and thermal properties of the target surface and the eroding materials and the conditions of erosion.

TARGET MATERIAL VARIABLES

The effects of target hardness, toughness and grain size on erosion are listed below. In addition, Ball (24) postulates that a high workening rate together with high strain to fracture is essential for high wear resistance. Hutchings and Field (25) state that the effects high strain rates, work hardening, thermal softening and hydrostatic pressures involved in elastic/plastic impact further complicate the erosion process.

The thermal properties of the target materials are important in determining the amount of heat dissipated from the impact zone during the erosion process.

Target hardness

Brittle materials generally exhibit an inverse relationship between target hardness and erosion rates (26, 27). Hardness is a measure of a material's ability to resist plastic deformation. A high hardness will reduce the amount of irreversible deformation at the impact site and therefore the driving force for lateral crack formation will be lower. In addition to this, particle blunting will occur more readily on striking a hard material.

Srinivasan and Scattergood (28, 29) state that the relative hardness of the target material is important. The erosion resistance of brittle materials goes through a marked transition as the target to particle hardness ratio approaches unity. They found that single impact events involving a softer erodent striking a harder target had a plastic punching type morphology whereas a harder erodent caused lateral cracking in a softer target. However, the steady state erosion mechanisms of alumina surfaces by softer alumina and harder silicon carbide erodents were similar and involved intergranular crack propagation, suggesting that a damage accumulation process was operative. The softer alumina erodent particles were prone to crushing and flattening on impact effectively, reducing their erosion efficiency.

In the event of adiabatic impact, the target material may soften in the impact zone due to plasticity induced heating or frictional heating. The hardness of the target material is a major determinant of the amount of plasticity induced heating that will occur. Heating is greater in harder materials.

Target toughness and microstructure

The critical stress intensity factor or toughness, Kc, indicates a material's resistance to macroscopic crack propagation. In the erosion of brittle materials, where material removal occurs as a result of cracking one would expect that a materials resistance to crack initiation and propagation to be of prime importance. The size, density and distribution of defects in the microstructure will determine the ease of initiation and the toughness of a material will determine its resistance to crack propagation. As fracture initiation in the erosion of brittle materials is almost inevitable, the ability of a material to minimize crack propagation is of prime importance (30).

Indentation toughness measurement is used extensively on brittle materials (31). Advantages of this method include: the easy preparation of small samples; the relative ease of measuring crack length and the fact that testing is performed on universally accepted equipment. Thus, comparable results may be obtained by quick, cost effective means. However, complications arise in accurate crack length measurement and identification of the operating crack systems. A large number of equations are reported in the literature and there is often a discrepancy between indentation toughness and other fracture toughness tests. It was thought that, due to the similarity between indentation and particle impact, the indentation fracture

toughness would be the most appropriate, although the strain rates involved in elastic/plastic impact are much greater than those encountered in quasi-static diamond indentation.

R-curve and T-curve effects

The fracture toughness of ceramic materials is not unique, but is dependent on the crack size. Many materials exhibit increasing resistance to fracture with increasing crack extension. This is referred to as R-curve behaviour (32, 33). The measured fracture resistance also shows a decreasing tendency for increased toughness with increasing crack propagation and results in a plateau level of macro-toughness.

The pronounced R-curve behavior of the toughened zirconias is linked to the size of the transformation zone around and in front of the crack tip (34). For small crack lengths the process zone and the amount of transformation is small, and therefore the effect of transformation toughening is minimized.

Cho et Al (35) found that the wear resistance of aluminas was low for the coarser grained materials which had the highest macrotoughness. This they attributed to the T-curve behaviour of aluminas which is described as a function of the toughness vs crack size. T-curve behaviour in aluminas is linked to the bridging behaviour of restraining interlocking grains of opposing intergranular crack interfaces. The key to this is the internal stresses due to thermal expansion mismatch in the non-cubic alumina matrix. For small crack sizes the microcracks tend to propagate in regions where the residual stresses are tensile, effectively reducing the intrinsic grain boundary toughness. For large crack lengths the compressive component of the internal stress leads to increased crack restraint by resisting the pull out of the bridging grains.

Thus the non-correlation between macroscopic toughness values and erosion resistance may be attributed to R- and T-curve effects. For small crack lengths associated with erosive wear the fracture resistance of materials will tend to their minimum value and toughness is often overrated.

Grain size

Erosive damage in brittle materials is on a similar scale to microstructure and grain size. Thus one would expect grain size to play an important part in the erosion process. In brittle materials that erode by intergranular fracture, small grained materials require more surface energy for fracture and therefore the erosion rates are lower.

The strength of non-cubic polycrystalline ceramics is strongly dependent on grain size. This is linked to the internal stresses that arise from thermal expansion anisotropy (36) which also explain the T-curve effects seen in alumina. Thermal expansion mismatch has been known to cause spontaneous cracking in very large (~400 microns) grained aluminas (35).

Thermal properties

The thermal properties are important in solid particle erosion where localised heating may occur within the impact sites. The conductivity of a material will determine the rate at which the heat is dissipated from the impact site. The specific heat capacity and density of the target material will determine the ultimate temperature increase within the impact site. Localised heating results in increased plasticity of material within the impact site and a resultant decrease in hardness and a small increase in toughness due to plastic blunting of sharp crack tips in brittle materials.

ERODENT PARTICLE VARIABLES

The initial kinetic energy of the particles and their ability to effectively transfer this energy to the target surface are important in erosion and are controlled by various erodent properties.

Particle hardness

Hardness is often used as a measure of the strength and integrity of a particle (37). Soft particles are prone to particle blunting and there is a decreased tendency for plastic deformation beneath blunt indenters, making lateral crack initiation less likely and favouring Hertzian fracture. Harder particles are more likely to maintain their integrity on impact and are more able to concentrate energy in a surface.

Wada and co-workers have shown that the properties of the erodent particles affect the erosion rates and crack morphologies of brittle materials and that the erosion rates inrease with increasing particle hardness (72).

When a soft brittle erodent particle strikes a harder surface, plastic deformation and fracture may occur in the erodent particle decreasing the amount of energy available for target damage. A hard tough particle, silicon carbide for example, would be more successful in transferring kinetic energy to the target surface. When the erodent hardness is much greater than the target hardness, it would seem unlikely that a further increase in erodent hardness would be important and by the same argument, the relative wear resistance should show less variation as the relative hardness increases.

Particle size

Larger particles have a higher kinetic energy by virtue of their size and therefore have the potential to do more erosive damage. In addition to this they induce large contact areas and large stress fields bringing the size effect into play. This interaction of a stress field with a critically sized flaw may result in fracture. The possibility of this occurring increases with the size of the stress field. Thus brittle materials can undergo a transition from a brittle to a semi-brittle response as the particle size decreases below a critical value (43).

For ductile erosion the erosion rate is independent of size for large particles and drops steadily at a threshold diameter of about 20 microns (38, 39, 40).

When particles are accelerated under the same pressure differential, finer sized particles cause higher erosion rates because of their considerably higher velocity and the strong dependence of erosion rate on particle velocity (39).

The distribution of particle sizes within a mixture is important . The erosion rate of a particle mixture prepared by mixing different sized particles together has been found to be considerably higher than the erosion rates of the component particles (39). Thus if the experimental particle size distribution is narrower than that of the in-service particles, there is the possibility of underestimating erosion rates (41).

Another important aspect of particle size is the strain rate induced in the target material. For purely elastic loading the strain rate is inversely proportional to

particle radius and only varies slightly with velocity. The strain rate (ε) for perfectly plastic impact is given as (from Hutchings (42)):

$$\varepsilon = (2^{2/3} v^{1/2} (3P/2\rho)^{1/4})/5\pi r$$

where v is the particle velocity
P is the target hardness
ρ is the erodent density
and r is the particle radius.

For example, the strain rate encountered for an alumina particle striking an alumina surface is in the region of 6×10^5 s^{-1} (v=40 m/s, r=50 microns). Thus very high strain rates are experienced during the impact of small particles and these effect the mechanical response of the target material.

Particle shape

Sharp particles have a greater capacity to degrade surfaces (30). In the glancing impact of a ductile surface, sharp particles are more effective at machining chips and erosion rates are higher. In the erosion of brittle materials sharp particles are more able to concentrate stresses and induce irreversible deformation and subsequent lateral cracking. Blunt particles set up Hertzian stress fields which act on surface flaws while sharp, angular particles induce the median/lateral crack systems which are associated with higher erosion rates.

Bahadur and Badruddin (40) found that the erosion rate of steel increased with increasing angularity and decreasing particle elongation.

Particle density

When particles are of the same size and shape, their density determines their kinetic energy and thus affects the loading conditions. Thus the denser a particle, the higher its kinetic energy and the greater the potential for surface damage.

The particle density is important in determining the particle flux and for a particle mass feed rate (w), the particle flux (F) may be defined for spherical particles as:

$$F = w/(4/3\ \pi r^3 \rho)$$

where F is in particles per second
w is in mass per second

ρ is the particle density
and r is the particle radius.

Thus silica will have a higher flux than alumina because it is less dense. The particle flux is important in determining the amount of thermal reinforcement between impacts on the same site.

Thermal properties

The thermal properties of the erodent particles will control the rate of external heat flow from the impact zone during the contact period. Particles with a high thermal conductivity and heat capacity will 'cool' the impact zone and decrease the influence of thermomechanical effects.

EXPERIMENTAL VARIABLES

Impingement angle

The angle at which maximum erosion occurs is a good indication of the erosion process. Ductile erosion occurs most effectively at glancing impact angles while brittle erosion occurs most effectively at normal impact. Small particle impact and high temperatures have been known the change the ductile/brittle transition angle.

Wiederhorn et Al (44) found that strength degradation in crown glass surfaces decreased at more oblique impact angles and that the scale of impact damage was smaller although the damage patterns showed a marked elongation in the direction of impact.

Particle velocity

Particle velocity is considered to be a prime controlling variable in erosion. The velocity exponent, defined as the power to which velocity is raised in the erosion equation, tends to decrease with increasing particle size (45). High particle velocities result in high kinetic energies and loading pressures and have the potential to do more damage. Lateral cracking will be more prevalent at high velocities, resulting in greater erosion rates. Velocity exponents vary with material properties and experimental conditions and, for brittle materials have been measured in the range of 2 to 6. The velocity exponent appears to be insensitive to microstructure but dependent on the mode of erosion. The possibility of

secondary erosion occurring due to the re-impact of particle fragments is greater for higher airstream velocities.

The mechanism of erosion depends strongly on the impact velocity. The velocity regime may be described by the damage number, 'D in s^{-2} ', where $D=\rho v^2/Y$ and v is the impact velocity, ρ the erodent density and Y the yield stress of the target material (Field and Hutchings (25)).

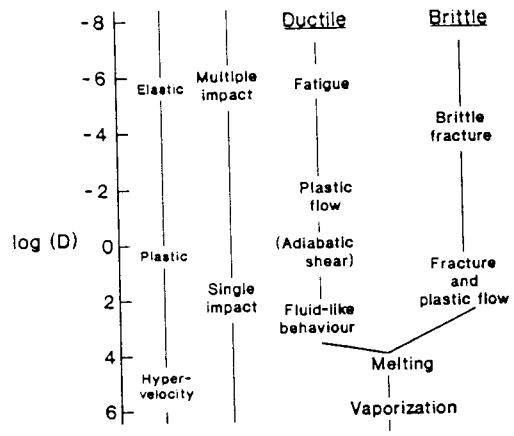

Fig. 2.9 Diagram indicating how the principal modes of deformation and mechanisms of erosion change with the damage number (D) (after Field and Hutchings (25)).

The modes of deformation and the dominant erosion mechanisms for ductile and brittle materials are summarised in fig. 2.9. For low values of D multiple impacts are required for material removal to occur. In the ordnance regime for very high velocities (500 m/s to 3 km/s and beyond) individual impacts cause substantial damage and material removal. Solid particle erosion is concerned with the damage in the sub-ordnance regime where velocities range from 5 to 500 m/s and impacts on metals cause plastic deformation and impacts on brittle materials result in elastic/plastic loading.

Aerodynamic effects

There is much literature available on the prediction of aerodynamic flow of a two-phase fluid mechanical system (46, 47, 48, 49, 50). However the effect of the turbulence created by placing the specimen holder in the airstream is assumed to remain constant, although small variations due to particle size, shape and density are to be expected.

Laitone (49) defines two limiting cases of particle flow:-

(i) in the case of extremely small particles, and when the particle density approaches that of the fluid, the particles will not impact a surface because they are completely entrained in the fluid and follow the fluid streamlines.

(ii) as the momentum of the particles increases, so the particles deviate from the streamlines. In the limit of very high momentum particles the particle trajectories follow straight lines as determined by initial conditions.

In practice, the most common flows lie between the two limits and the particle trajectories deviate from the fluid streamlines. It is incorrect to assume that the particle velocity on impact is the same as that measured far from the surface. The deviation of the particle impact angles is the result of drag forces acting tangentially to the surface (49) and increases from a central stagnation point (fig. 2.10) and the examination of eroded surfaces was performed in this area.

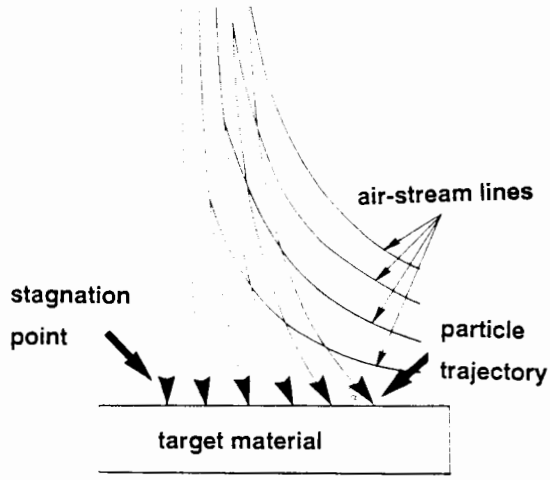

Fig. 2.10 The variation of the true impact angle due to turbulence created by the target.

Particle concentration

For a standard mass feed rate, the particle concentration, or flux, (in particles per second) is determined by particle size and density. High particle concentrations can complicate erosion studies due to particle/particle interference. Tilly suggests a decrease in erosion rates with particle concentration (26).

Particle concentration is important in determining the amount of thermal reinforcement due to impacts in the same site: the probability of thermal reinforcement increases with increasing particle concentration.

Erosion time

In some materials there is an incubation period during which the erosion rate stabilises to a steady state situation. In soft, ductile materials the incubation period is pronounced and involves particle embedment, strain hardening and surface roughening. The incubation period in brittle materials is generally very small or absent. Under low stress conditions the damage accumulation may be required before crack propagation can proceed.

Time of impact

When a particle strikes a surface, the time of contact depends on the size and geometry of the particles and surface, their mechanical properties and the mode of deformation in the contact region (25). The ratio of the contact duration to the time taken for the stress waves to traverse the target is critical in determining the loading rate and the materials response to loading.

In addition to this the time of contact is important in determining the amount of heat dissipation during impact and the strain rates. The time of impact for purely plastic loading is inversely proportional to the particle radius (42). The time of impact (t_p) for plastic loading is defined by Tabor (51) as:

$$t_p = \pi r(2\rho/3P)^{1/4}/2$$

where ρ is the erodent density
P is the mean indentation pressure
and r is the particle radius.

CHAPTER THREE: EXPERIMENTAL TECHNIQUES

3.1 MATERIALS CHARACTERISATION

Porosity evaluation

The target materials were polished to a 0.25 μm finish. The average percentage porosity was measured out by lineal analysis of optical micrographs of the polished surfaces. Care was taken in the polishing of the surfaces as the possibility of grain pullout occurring during automatic diamond polishing could result in an overestimation of the porosity. The porosities of the ultrahard materials were assumed to be negligible due to their dual phase nature and manufacturing techniques.

Grain size determination

The grain sizes of the ceramic materials were calculated from SEM micrographs of polished and etched surfaces (Table 3.1). Difficulty was encountered in etching TZP and Syalon and intergranular fracture surfaces were studied instead. Clinton's guide to ceramic etching (59) provided useful hints on technique. The grain sizes of the Syndite specimens were assumed to be similar to the pre-sintered diamond grit size.

Table 3.1 The etching techniques performed to reveal the microstructures of the ceramic and ultrahard materials

Material	Etching technique
MgPSZ, alumina	Boiling, concentrated phosphoric acid 4-6 mins
TZP, Syalon (glassy phase)	Boiling, concentrated phosphoric acid, 6 mins
PCBN	Boiling, 10% $NaOH/H_2O$ solution
Syndite	Boiling, 20% H_2SO_4 solution

3.2 MECHANICAL TESTING

The hardnesses and toughnesses of the target materials were measured using indentation techniques. The hardnesses of the ultrahard materials were provided by the De Beers Diamond Research Laboratories.

The average hardnesses and toughnesses of the ceramic materials were measured on polished surfaces under a 20 kgf load. Toughness was calculated according to the Method of Evans and Charles (App. 1). The hardnesses and toughnesses of the ultrahard materials were provided by the De Beers Diamond Research Laboratory.

Hardness measurement

Indentation of ceramic materials must be approached with care due to their brittle nature and susceptibility to cracking. The surface preparation is important. The surface layers that have been affected by grinding techniques must be polished away, these include layers of transformed zirconia, work hardened Syalon and microcracked alumina. Grinding of the toughened zirconias results in a compressive surface layer due to the volume increase associated with the t-m transformation and an increase in the microtoughness. Grinding of the brittle aluminas introduces microcracking in the surface layers and a decrease in the microtoughness.

Two additional problems are encountered during indentation of hard, brittle materials. Firstly, cracking during indentation may absorb some of the energy of indentation resulting in uncharacteristically high hardness measurements. Secondly, there is the possibility of the diamond indenter being deformed or damaged during indentation. To combat these problems, hardness measurements taken under various loads were compared, and the diamond indenter was routinely recalibrated between indentations.

Microhardness

Microhardness indents were made on polished target specimen surfaces using a Shimadzu Microhardness Tester fitted with a Vickers diamond indenter under indentation pressures of 500g and 1000g. The diameters were measured optically and in the SEM and compared.

Macrohardness

Macrohardness measurements were carried out on polished target material surfaces using an Eseway Hardness Tester fitted with a Vickers diamond indenter under loads of 20 and 30 kgf.

Toughness measurement

Indentation toughness was determined from direct crack measurement of an average of six hardness indents under each load regime. The method of toughness calculation is outlined in App. 1.

Due to the similarity between the quasi-static loading mode of indentation and particle impact, the indentation toughness was thought to be the most likely toughness to correlate with erosion.

3.3 SOLID PARTICLE EROSION

Target material preparation

With the exception of the ultrahard materials, all target specimens were manually ground down to a 1200 grit finish on silicon carbide papers. They were then ultrasonically cleaned in alcohol and polished on diamond impregnated pads in an automatic polisher using successively finer diamond grits, 15, 7, 2.5 and 0.25 microns, for 1.5, 1, 0.5 and 0.5 hours respectively. The long automatic polishing times are required to remove the surface layers that have been altered by grinding.

Erodent particle preparation

The alumina, silicon carbide and CDA industrial diamond erodents were utilised in the graded, clean condition in which they were received. The silica was obtained from the Consolidated Glassworks quarry and ranged in size from 20 to 300 microns. It was sieved, and the fraction between 104 and 115 microns was utilised. SEM in conjunction with EDS revealed the silica sand to be relatively free of contaminants.

Solid particle erosion was carried out on material surfaces that had been polished to a 0.25 micron finish using four different erodent types under standardised

experimental conditions. A simple gas-stream erosion rig was employed for the erosion tests. The damage in the target surface was examined in progressive stages of erosion.

The erosion rig

A simple, conventional air blasting type rig was utilised for the experiments (fig. 3.1). Air is fed into the inlet tube (A) under controlled pressure. Particles are fed via a feeding nozzle into the air stream (B) via a Venturi Valve (C). The particles accelerate in the airstream along a 3 m stainless steel acceleration tube. They reach a constant terminal velocity determined by air pressure (D), and particle density, shape and size. The average particle velocity was determined by the double rotating disk method of Ruff and Ives (App 2). The orientation of the target with respect to the airstream, the exposed target area and the distance between the accelerating tube and the target may be varied (E). The air leaves the erosion chamber (F) and particles are collected for examination (G).

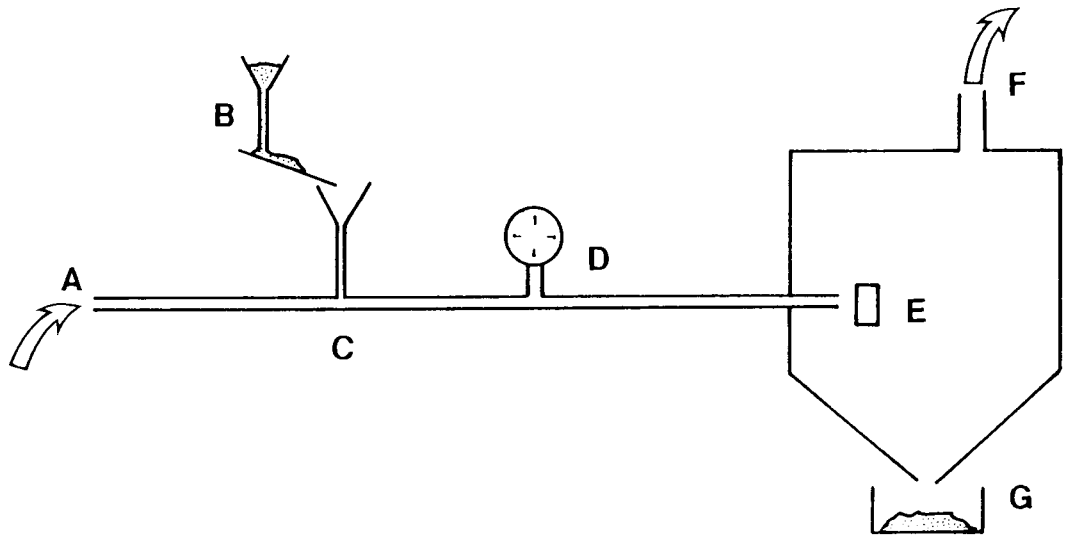

Figure 3.1 *A schematic representation of the gas-jet erosion rig.*

The standardised experimental conditions are listed in Table 3.2 below. The nozzle diameter controls the particle feed rate which may be calibrated by measuring the time of passage of 1 g of particles through the feeding nozzle.

Table 3.2 Standard operating parameters of the erosion rig

VARIABLE	RANGE
Particle velocity	40 m/s
Angle of attack	90 °
Operating temperature	room temperature
Erodent type	SiO_2, Al_2O_3, SiC, CDA
Average erodent size	100 microns
Particle feed rate	0.166 g/s
Length of tube	3 m
Tube diameter	10 mm
Exposed target area	47 mm^2

Particle flux

The standard particle feed rate was designated in mass per unit time. For a standard velocity of 40 m/s, the total kinetic energy of the four erodent particle types will be the same. The rate at which kinetic energy is delivered to the target surface may be calculated from KE = 1/2 m v^2, and for standard experimental conditions is 0.133 J/S. However, the amount of energy delivered to the surface for a single impact is a function of the erodent size and density. The particle flux also differs with density for the four erodents, assuming that the average sizes of the particles remain the same. For a standard mass feed rate (w) the particle flux may be defined as:

$$F = w / (4/3)\pi r^3 \rho$$

where F is the particle flux (particles per second)
$(4/3)\pi r^3$ is the volume of a spherical particle
ρ is the particle density
and r is the average particle density.

Thus for the dense alumina particles, the particle flux is low but the initial kinetic energy of the individual particles is high.

Single impact testing

In order to study the morphology of single particle impact on virgin target surfaces, polished target surfaces were subjected to erosion with <0.25 g of erodent under standard experimental conditions. The specimens were ultrasonically cleaned and prepared for viewing in the SEM.

Steady state erosion testing

The target material surfaces were repolished and subjected to erosion under standard experimental conditions by measured amounts of erodent particles. After each erosion run the target specimens were ultrasonically cleaned in alcohol, thoroughly dried and weighed on a gravitational balance accurate to five decimal places. The cumulative mass loss was calculated as a function of mass of erodent used and converted to volume loss per gram of erodent in order to compare the erosion rates of materials with different densities. The steady state erosion rate was taken after ten constant, consecutive erosion rates were recorded.

Ultrasonic cleaning was found to aggravate lateral spallation in the alumina target materials and was kept to a minimum. The more porous ceramics retained the cleaning alcohol by capillary action of the pores and were dried and reweighed until constant masses were recorded in between each erosion run.

At the start of the erosion testing, a repeatability test was performed on two specimens of MgPSZ using SiC grit under standard conditions (App 3). A maximum variation of less than 4% was recorded after ten erosion cycles. The tests were thought to be repeatable.

3.4 FRACTOGRAPHY

Optical microscopy

The optical microscope was utilised in the preliminary examination of the target and erodent materials, the examination of the surface finish of the polished surfaces and for the qualitative survey of deformation and subsurface cracking under polarised light.

Due to the nature of the eroded surfaces and the high magnifications required, the resolution and depth of field of the light microscope was found to be insufficient for the survey of the impact sites.

Scanning Electron Microscopy

The scanning electron microscope (SEM) was found to be an invaluable tool for the assessment of damage both in the eroded target surfaces and the spent erodent particles.

To prevent charging in the microscope due to the nonconductive nature of the materials, they were mounted on aluminium stubs and gold/palladium sputtercoated for four minutes and a low accelerating voltage was used (10-20 kV). The erodent particles were mounted in colloidal graphite prior to sputtercoating. The backscattered electron (BSE) detector was used extensively to increase topographical detail and prevent flaring from sharp edges. Energy dispersive spectroscopy (EDS) was used to identify and distinguish between target and erodent debris in the impact sites and to qualitatively assess the nature of the stringer and tear drop formations observed on some of the target materials.

CHAPTER FOUR: MATERIALS CHARACTERISATION

4.1 TARGET MATERIALS

The nine target materials used for the erosion studies are listed in Table 4.1, together with their measured porosities, densities, grain sizes and mechanical properties. The materials were chosen for the spread of hardness and toughness values and the different characteristics of their microstructures. It was hoped that this would transpire in a wide variety of erosion modes and give insight into the different mechanisms by which erosion occurs. Each of the target materials are described in the following paragraphs in terms of their development, crystal structure, microstructure, phase stability and mechanical properties.

Table 4.1 **A summary of the target materials, their densities, Young's Moduli and grain sizes.**

Material	Tradename	Porosity (%)	Density (Mg/m^3)	Grain size (microns)	Youngs Modulus	Hardness (HV20)	Toughness ($MN/m^{3/2}$)
Partially stabilised zirconia	MgPSZ*	4.0	5.7	48	205	1049	7.5
Alumina A17	A17*	5.0	3.89	6.7	380	1396	2.9
Sialon	Syalon**	3.2	3.3	2.0	288	1584	4.2
Tetragonal zirconia* polycrystals	TZP	1.5	6.1	0.5	207	1585	14.5
Alumina A16	A16*	2.2	3.94	4.2	380	1750	3.1
Alumina R	R*	1.5	3.98	2.0	380	1892	4.1
PCBN	Amborite#	0.0	3.4	7.0	680	3200	9
PCD	Syndite 002#	0.0	4.2	2.0	750	5000	10
PCD	Syndite 025#	0.0	3.9	25	810	5000	10

* *DMST*
** *Lucas Cookson*
\# *De Beers Diamond Research Laboratories*

ZIRCONIA

Pure zirconium oxide is ionic in nature and consists of three major polymorphs that are stable at different temperatures. From room temperature to 1000°C zirconia

exists as a baddelyte structure with a monoclinic unit cell. At 1000°C there is a martensitic transformation to a tetragonal structure resulting in a 3-5% volume contraction. At 2280°C the coordination becomes regular resulting in a transformation to a cubic unit cell of the fluorite type. This structure persists to the melting point at 2850°C.

Pure zirconia, on cooling, undergoes a martensitic t-m transformation at 1000°C causing a 3-5% volume expansion which cannot be accommodated by the matrix and results in catastrophic failure. This transformation may be advantageous if it can be controlled and made to transform heterogenously. The two methods have been developed to control the transformation and are outlined below.

The zirconia may be alloyed with appropriate elements to increase the mean cation radius and form a suitable radius ratio for cubic coordination at the exclusion of the tetragonal and monoclinic crystal forms. Alternatively, a combination of alloying and heat treatment may be used to form single domain particles of tetragonal zirconia below the critical radius ratio (~1 micron). Small quantities of the rare earth oxides, magnesia, ceria, yttria and calcia, are typically used for full or partial stabilisation of zirconia.

Partially stabilised zirconia (MgPSZ)

MgPSZ consists of a dispersion of fine lathe shaped tetragonal and larger monoclinic precipitates in a cubic matrix. It is formed by adding insufficient dopant for full stabilisation and/or by suitable heat treatment of the fully stabilised form (52). There are two mechanisms for improving the mechanical properties.

If the tetragonal precipitates are smaller than the critical radius they are retained at room temperature due to the constraint of the matrix. An advancing crack tip projecting a tensile stress field ahead of itself may induce a t-m transformation by counteracting the matrix constraint. The resultant increase in volume causes a net compressive stress around the precipitate. This restricts crack propagation by counteracting the tensile stress and effectively closing the crack tip and thereby enhancing the toughness of the material.

If the tetragonal precipitates form close to the critical radius then, on cooling, there is a t-m transformation with an accompanying volume increase and shear. This sets up tangential stresses around the precipitate and microcracking is induced in

the surrounding matrix in order to accommodate the larger monoclinic phase. These microcracks interact with propagating cracks and cause crack bifurcation, decreasing the fracture energy and increasing the inherent toughness of the zirconia.

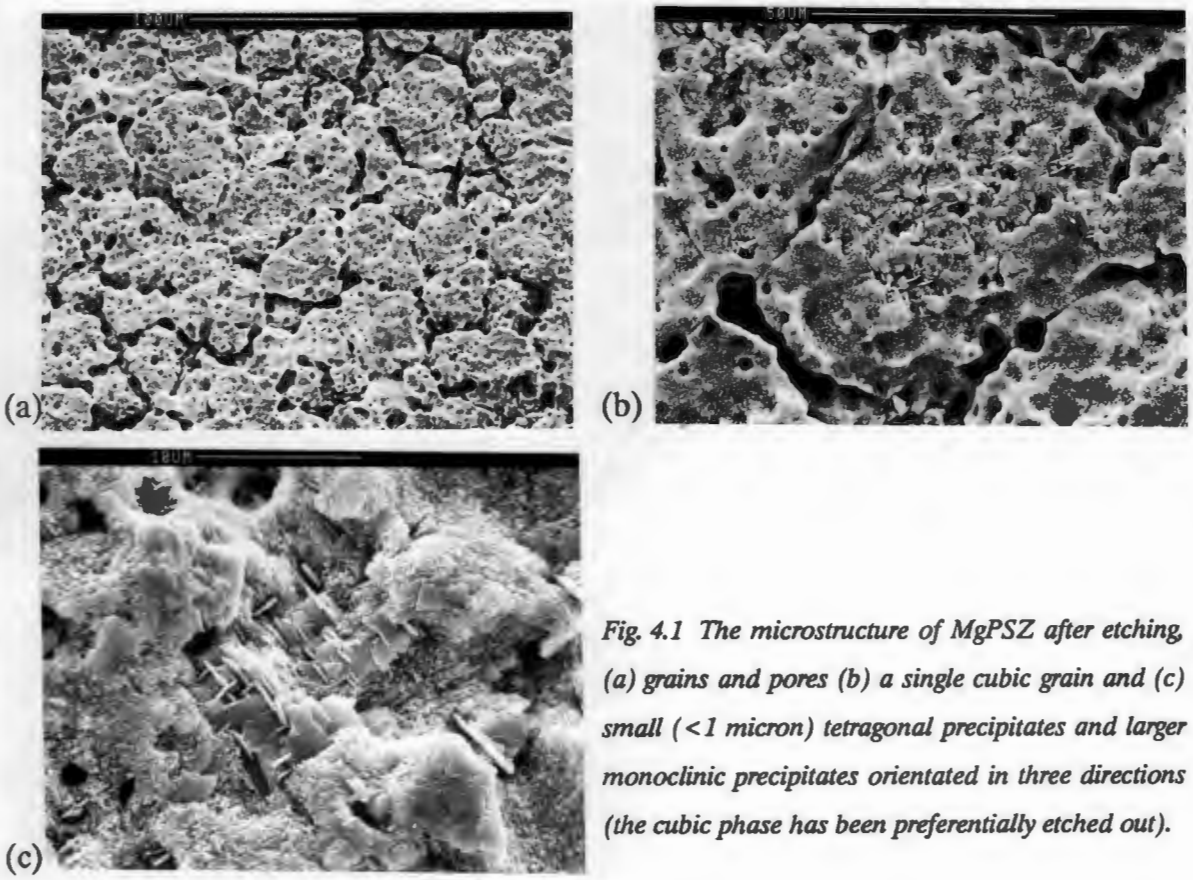

Fig. 4.1 The microstructure of MgPSZ after etching, (a) grains and pores (b) a single cubic grain and (c) small (<1 micron) tetragonal precipitates and larger monoclinic precipitates orientated in three directions (the cubic phase has been preferentially etched out).

The MgPSZ used during the course of this study contained 10 molar percent of magnesia dopant. It consists of large cubic grains containing small crystallographically orientated tetragonal lathes (fig. 4.1) and larger lenticular monoclinic grains.

Tetragonal zirconia polycrystals (TZP)

The addition of sufficient amounts of dopant (0-10 mol %) results in complete stabilisation of zirconia. The resultant material has a toughness which is unprecedented in ceramics. Cracks propagating through the matrix cause the transformation of the tetragonal phase in the crack process zone. The volume expansion and shear strain set up compressive stresses ahead of the crack tip and extra energy is required to move the crack through the matrix accounting for the high toughness (53). In addition, grinding of the surface causes wholesale

transformation setting up a large biaxial compressive stress resulting in a toughened surface layer.

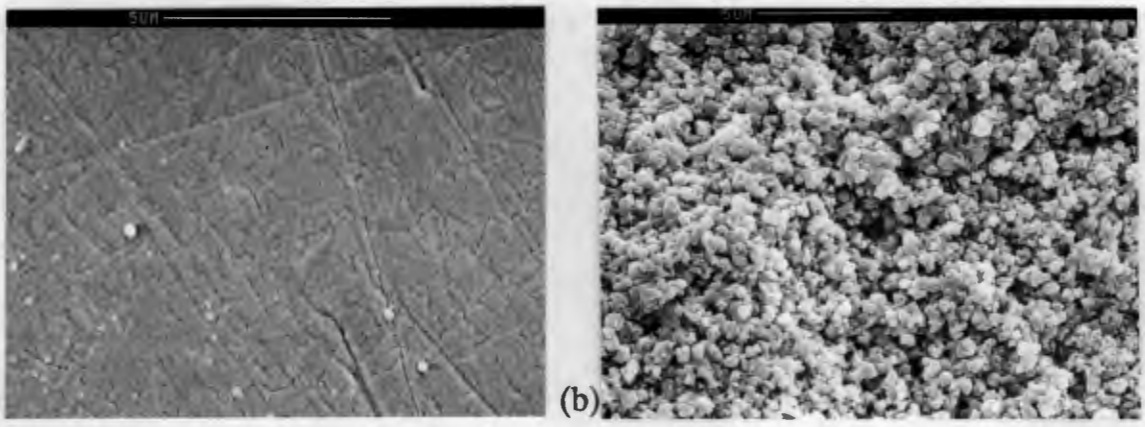

Figure 4.2 *Microstructure of TZP (a) after slight etching of the intergranular glassy phase and (b) intergranular fracture surface showing grain size and shape.*

The addition of yttria progressively decreases the temperature of the t-m transformation relative to the pure material for up to 5mol% (54). The fully stabilised zirconia used in this project contains 3mol% yttria dopant and has a very fine metastable tetragonal grain structure and a small amount of intergranular glassy phase (fig. 4.2).

SIALON CERAMIC

The development of a strong, tough high temperature ceramic suitable for the mass production of complex shaped components led to the discovery of a family of ceramic materials generically named Sialons. The sialon alloy system is produced by the partial stoichiometric substitution of aluminium and oxygen in a β-silicon nitride, Si_3N_4, resulting in $Si_{(6-z)}Al_zO_zN_{(8-z)}$, hence its name. This results in a strong pressureless sintered material which is chemically stable and has better high temperature properties than β-silicon nitride. The alumina has important implications in processing and manufacturing as it lowers the vapour pressure allowing conventional sintering techniques to be carried out at relatively low temperatures. This reduces the time-at-temperature and minimises grain growth resulting in a fine grained microstructure and improved mechanical properties.

The degree of substitution of alumina into the β-silicon nitride lattice determines the composition and volume fraction of the intergranular phase. Low degrees of substitution produce materials with an expanded beta (β') phase in a matrix of glass. Highly substituted materials consist of an expanded β' lattice and an

intergranular yttrium aluminium garnet (YAG) phase. The β'glass materials exhibit high strength up to 1000°C after which softening of the glassy phase produces a rapid decline in strength. β'YAG materials have a slightly lower room temperature strength but retain 75% of this strength at 1400°C and also have a high creep resistance at elevated temperatures (55).

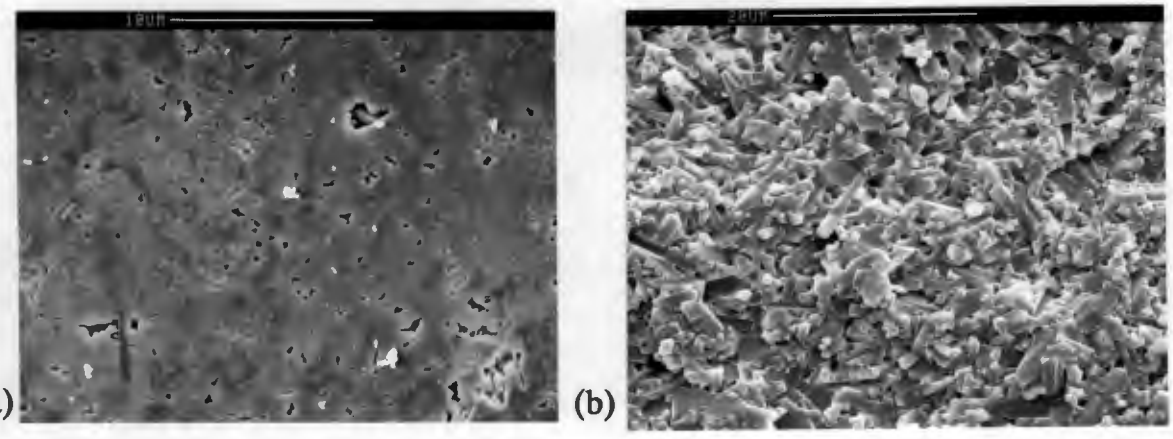

Figure 4.3 *Microstructure of Syalon (a) after slight etching of the intergranular YAG phase (b) intergranular fracture surface showing the size and shape of the β' grains.*

Yttria has been used as a sintering aid in the production of Syalon, classified as a β'YAG sialon, by Lucas Cookson (PTY) Ltd. It has a very fine grain structure and is susceptible to work hardening.

ALUMINA

Alumina has a distorted close packed hexagonal crystal structure and a small amount of intergranular glassy phase. Its expected ionic nature is slightly modified by the presence of small highly charged Al^{3+} ions which result in ~40% covalent nature. Large plastic and thermal anisotropies are encountered due to the distortion of the HCP structure.

Three modifications of high purity, high density alumina have been used in the course of this work (fig. 4.4). They differ in porosity, density grain size and purity and allow a systematic investigation into the interdependence of these variables. The alumina target materials were the only ceramics tested that did not undergo phase transformation or work hardening and therefore could be considered model ceramics.

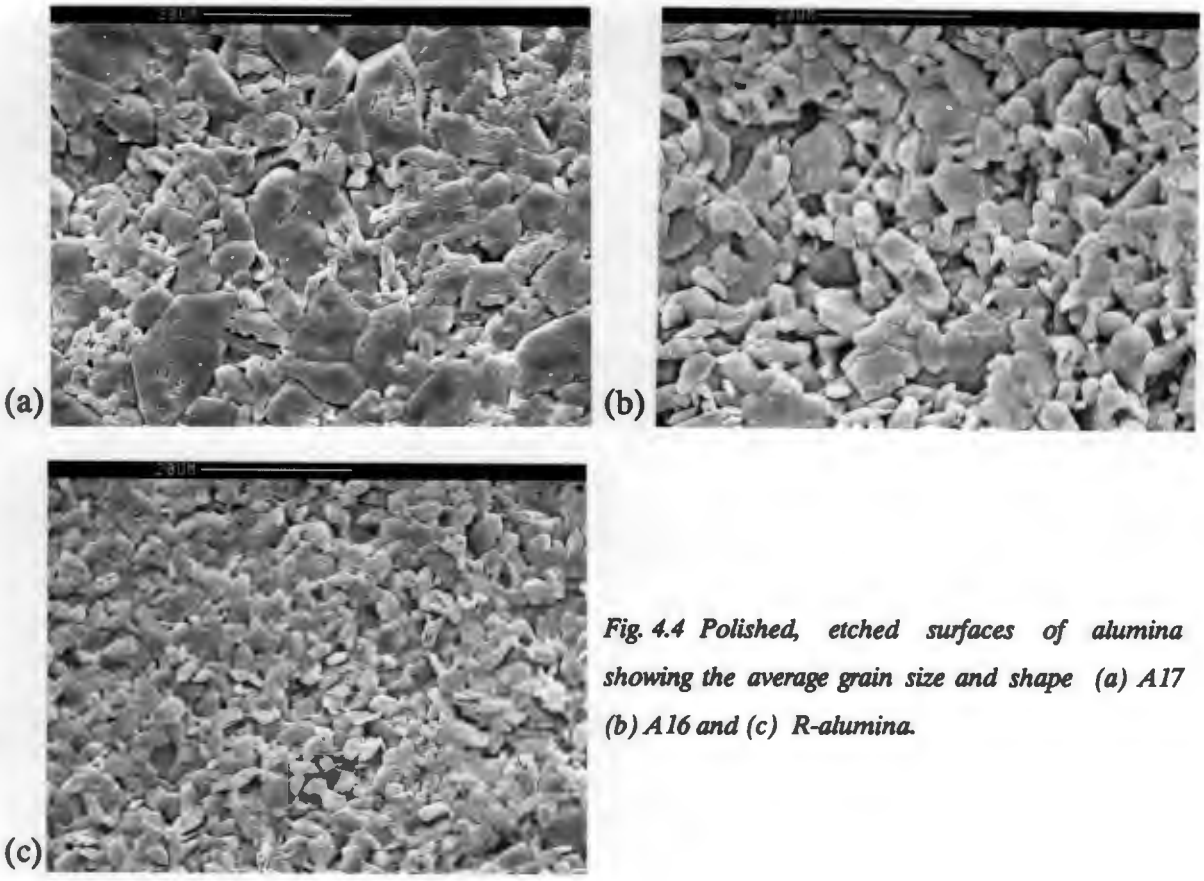

Fig. 4.4 Polished, etched surfaces of alumina showing the average grain size and shape (a) A17 (b) A16 and (c) R-alumina.

The strength of alumina is largely dependent on the purity, porosity, grain size and finishing conditions. Tests have shown that bending strength increases with alumina content (56). The strength is strongly dependent on microstructure and the presence of critical flaws resulting in a scattering of the strength values of up to 20%. Fractures originate from inhomogeneous regions such as grain boundaries, pores, large grains and impurity inclusions. The strength is also dependent on surface conditions. Maximum stress is usually at the surface and fracture can originate at defects introduced by surface machining.

The strength of aluminas is also related to temperature. There is a gradual increase in the strength of alumina up to 800°C followed by an abrupt decrease in the strength. This is thought to be due to an increase in the stresses generated by the thermal expansion mismatch of the crystalline and glassy phases and the blunting of sharp crack tips resulting in smaller stress concentrations. The sudden decrease in strength is due to local plastic deformation of the glassy phase, relieving the internal stresses (56).

POLYCRYSTALLINE CUBIC BORON NITRIDE (PCBN)

Cubic boron nitride (CBN) is the second hardest material known to man and is used for the cutting of ferrous alloys where diffusion wear of diamond composites is a problem. Amborite is a polycrystalline born nitride manufactured by the De Beers Industrial Diamond Division (PTY) Ltd.

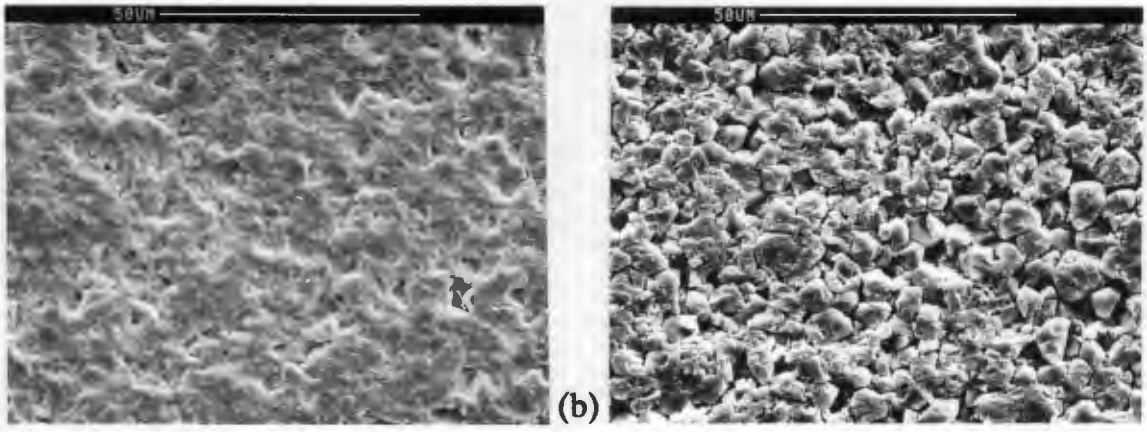

Figure 4.5 *Surface of Amborite (a) as received (b) after etching out the aluminium binder phase to reveal the CBN grains.*

Amborite is made by subjecting fine, randomly orientated amber boron nitride particles to high temperatures and pressures in the presence of aluminium. The CBN reacts with the aluminium to form a thin aluminium nitride skin and a residual binder phase of aluminium diboride resulting in a fully dense tough polycrystalline structure. During sintering, deformation and fracture of CBN grains occurs, and this, in conjunction with the polycrystalline structure, results in a transgranular fracture path (57).

The Amborite used in this work has a nominal CBN grain size of 8 microns (fig. 4.5) and 18% of aluminium was admixed before sintering resulting in a final binder content of 12%.

POLYCRYSTALLINE DIAMOND (PCD)

The mechanical and physical properties, such as hardness, elastic constant, wear resistance and cleavage, are highly orientation dependent in a single crystal diamond. Diamond crystals cleave easily along the weak octahedral planes. Thus the development of a fine, randomly orientated polycrystalline structure to improve toughness. Syndite, a PCD manufactured by the De Beers Industrial Diamond Division (PTY) Ltd., is an extremely tough intergrown mosaic of diamond on a

tungsten carbide base, and may be regarded as a composite combining the hardness of diamond with the toughness of the WC base.

Fig. 4.6 Diamond bridges formed during the sintering of diamond particles in the presence of a cobalt catalyst (Syndite 002).

Syndite is manufactured by hot isostatic pressing (hip) of fine synthetic or natural diamond grit in the presence of a cobalt solvent/catalyst. The graded diamond grits are consolidated at temperatures and pressures similar to those at which they were originally synthesised (1500-2000°C, 5-7 GPa).

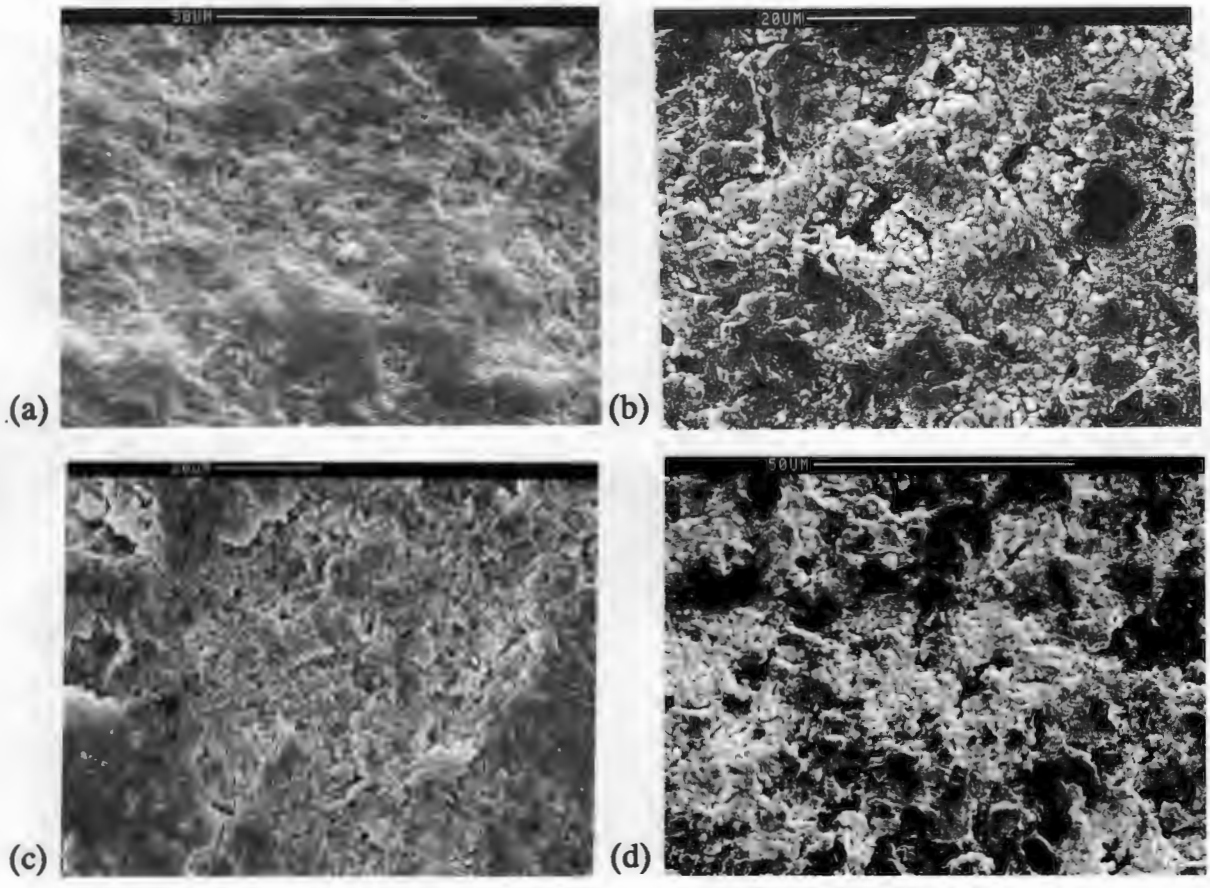

Figure 4.7 *(a) Syndite 002 as received and (b) after etching, (c) Syndite 025 as received and (d) after etching out cobalt binder.*

During sintering, plastic deformation of the diamond and graphite takes place, and at high temperatures, a small amount of surface diamond reconverts to graphite and diffuses into the cobalt catalyst. Reprecipitation of the diamond causes extensive grain intergrowth resulting in a contiguous skeletal mosaic structure of diamond (fig. 4.6) with a cobalt filling. It has the hardness of diamond but an isotopic toughness superior to that of diamond.

Two modifications of Syndite were used: Syndite 002 with a grit size of 2 microns and Syndite 025 with a nominal grit size of 25 microns (fig. 4.7). Toughness is influenced by grain size, cobalt content and the degree of plastic deformation and fragmentation of the diamond grains during synthesis.

4.2 THE ERODENT PARTICLES

Four different erodent particle types were used in the solid particle erosion experiments. They were chosen for the spread of hardness values exhibited and had an average grain size of 100 microns. They are listed in Table 4.2, together with the estimated angularity as seen in the SEM. Each erodent is briefly characterised in the following paragraphs.

Table 4.2 **A summary of the erodent particles, their hardness and angularity.**

Erodent Particles	Hardness (HV)	Angularity	Density (Mg/m^3)	Av. KE per part. ($X10^{-6}J$)
SILICA	1100	ROUNDED	2.63	1.1
ALUMINA	1800	SHARP	3.99	1.67
SILICON CARBIDE	2500	ANGULAR	3.21	1.34
DIAMOND (CDA)	8000	BLOCKY	3.51	1.47

SILICA

The silica erodent grit was obtained from the Consolidated Glassworks quarry, Phillipi, Cape Town. It consists of rounded porous grains of 'clean' silica sand. The rounded nature is thought to the result of wind and wave action on the sand. The particles have an irregular crystal size, a large amount of surface asperity and are very friable. The silica was sieved prior to use and the faction between 105-115 microns was used.

Fig 4.8 SEM micrograph of the rounded silica sand grains.

ALUMINA

Alumina particles were obtained from Cumar Abrasives (PTY) Ltd. The particles are sharp, flint-like and elongated with an average particle diameter of 100 microns and an intergranular glassy phase.

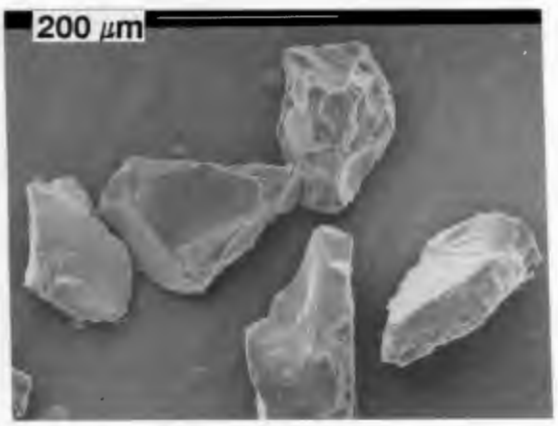

Fig. 4.9 SEM micrograph of the flint-like alumina particles.

SILICON CARBIDE

The silicon carbide particles were supplied by Cumar Abrasives (PTY) Ltd. and are marketed under the tradename Carborundum. The particles are very sharp and angular with surface asperities. The SiC particles were the most tough (4.1 MN $m^{-3/2}$) and least friable erodent particles utilised and have a high thermal conductivity. Silicon carbide particles have a thin oxide skin.

Fig. 4.10 SEM micrograph of the sharp angular silicon carbide particles.

CDA INDUSTRIAL DIAMONDS

CDA is a synthetic industrial diamond manufactured by the De Beers Industrial Diamond Division (PTY) Ltd. The particles have a very irregular shape and a large number of inherent crystal cleavage planes. This results in the controlled breakdown of the particles at regular intervals during use resulting in new, sharp cutting surfaces being formed. CDA is used for grinding and machining hard alumina and non-oxide ceramics and non-ferrous metals (58) and the cutting and polishing of cement, concrete and marble.

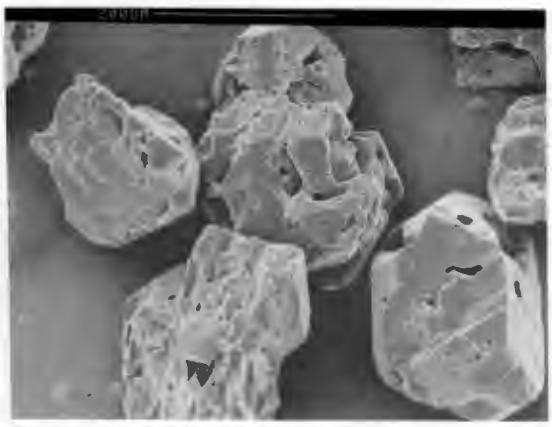

Fig. 4.11 SEM micrograph of the irregularly shaped CDA industrial diamond particles.

CHAPTER FIVE: RESULTS

5.1 MATERIALS TESTING

A summary of the relevant material properties and the steady state erosion rates are listed in Table 5.1. The materials have been listed in order of increasing hardness.

Table 5.1 **A summary of the properties of the target materials and their steady state erosion rates.**

Material	Porosity (%)	Density (Mg/m^3)	Grain size (microns)	Youngs Modulus (GPa)	Hardness (H_V20)	Toughness ($MN/m^{3/2}$)	Steady state erosion rate ($X10^{-5}$ cm^3/g)			
							SiO_2	Al_2O_3	SiC	CDA
MgPSZ	4.0	5.7	48	205	1049	7.5	0.30	0.63	3.02	2.98
A17	5.0	3.89	6.7	380	1396	2.9	11.40	6.70	11.0	24.00
Syalon	3.2	3.3	2.0	288	1584	4.2	0.019	0.18	1.33	1.79
TZP	1.5	6.1	0.5	207	1585	14.5	0.009	0.18	1.52	1.10
A16	2.2	3.94	4.2	380	1750	3.1	3.1	3.0	6.27	14.7
R	1.5	3.98	2.0	380	1892	4.1	0.01	0.14	2.66	4.83
PCBN	0.0	3.4	7.0	680	3200	9*	#	0.096	0.17	3.43
PCD002	0.0	4.2	2.0	750	5000	10*	#	0.054	#	1.20
PCD025	0.0	3.9	25	810	5000	10*	#	0.058	#	1.65

* *Toughness was provided by the De Beers Diamond Research Laboratory*
\# *No significant weight loss was recorded*

The steady state erosion rates of the target materials were calculated from a plot of cumulative target mass loss vs mass of erodent used, after ten constant consecutive mass losses were recorded. The erosion rates were converted to volume loss per gram of erodent in order to compare the erosion rates of materials of different densities. The incubation periods were found to be very small or nonexistent.

There are twelve different erosion responses that can expected in the erosion of ceramic and ultrahard materials. These are listed in fig. 5.1.

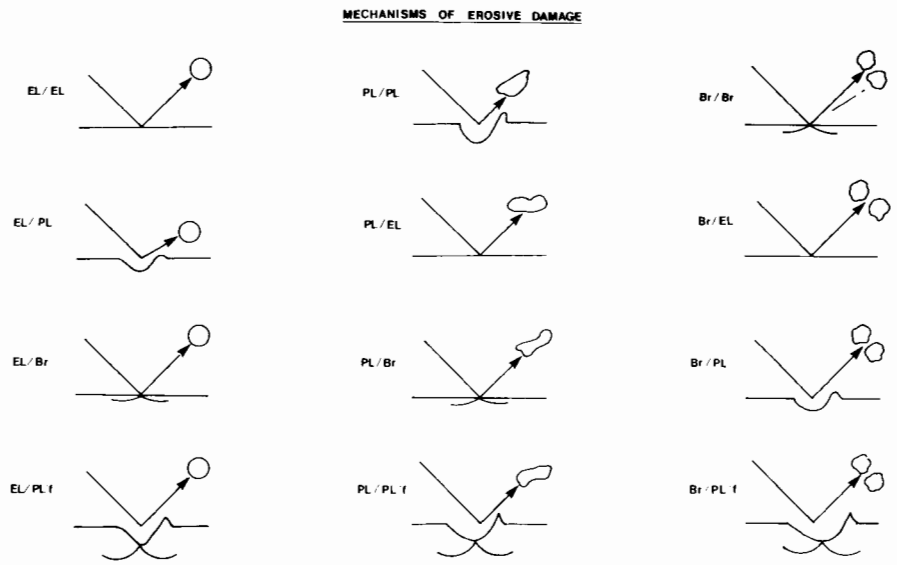

Figure 5.1 *The twelve different erosion responses that are anticipated in the erosion of ceramic and ultrahard materials (where El=ealstic, Pl=Plastic and fr=fracture).*

In addition to a purely elastic response, the target and the erodent particles may deform plastically and/or exhibit fracture processes. The comparative target and erodent properties that result in the twelve different erosion responses are listed in Table 5.2. For example, the impact of a hard tough particle on a soft tough target will result in a plastic cutting process reminiscent of the erosion of metals by hard particles. If the particles are soft or brittle then the damage process is apportioned and the amount of damage to the target is reduced.

Table 5.2 **The comparative properties of the erodent and target materials that result in the twelve different erosion responses outlined in fig. 5.1.**

	Target properties			
Erodent properties	Hard Tough	Hard Brittle	Soft Tough	Soft Brittle
Hard, tough	El/El	El/Br	El/Pl	El/Pl, fr
Hard, brittle	Br/El	Br/Br	Br/Pl	Br/Pl, fr
Soft, tough	Pl/El	Pl/Br	Pl/Pl	Pl/Pl fr

where Pl= Plastic, Br= Brittle and fr= fracture

5.2 FRACTOGRAPHY OF SINGLE IMPACT SITES

Invaluable information was obtained from studying single impact sites on polished target surfaces. For each erodent/particle combination, a variation in the size and morphology of the impact sites was encountered due to slight differences in the size, geometry and orientation of the erodent particles, the rotation of particles on impact, the presence of critical flaws and the effect of turbulence on particle flow.

The most representative micrographs for each erodent/target combination have been presented in the following pages in order of increasing target hardness. Where possible, the average sizes of contact zones, plastic deformation and cracking, estimated from a number of impact sites, have been included as a guide to the extent of damage.

Tear drop formations, rivulets and stringers are considered to be features that arise from the heating and melting of material during solid particle erosion.

No damage was seen in the ultrahard target surfaces after erosion by small amounts of erodent particles and examination of the erosion damage was confined to the steady state surfaces of these materials.

MgPSZ

The impact of the softer silica particles on MgPSZ results in small plastic punching-type craters (5-15 microns). A large number of flattened debris flakes were visible on the target surface and no cracking was evident (fig. 5.2a).

The impact of the harder alumina particles on MgPSZ results in elongated, cutting-type, plastic craters (10-20 microns). Material is extruded in lips at the sides there is often tearing in the highly deformed lip material (fig. 5.2b). There is no evidence of concoidal fracture although a small amount of lateral cracking can be seen to initiate from surface pores.

The impact of the harder silicon carbide and CDA diamond particles on MgPSZ results in large, well defined, plastically deformed craters and transgranular concoidal fracture (fig. 5.2c&d). The impact of silicon carbide particles causes extensive lip formation and tearing of the highly deformed lip material. The ratio of plastic deformation to fracture is lower for the impact of the CDA particles.

Secondary erosion due to reimpacting CDA particle fragments results in small plastic craters (1 micron).

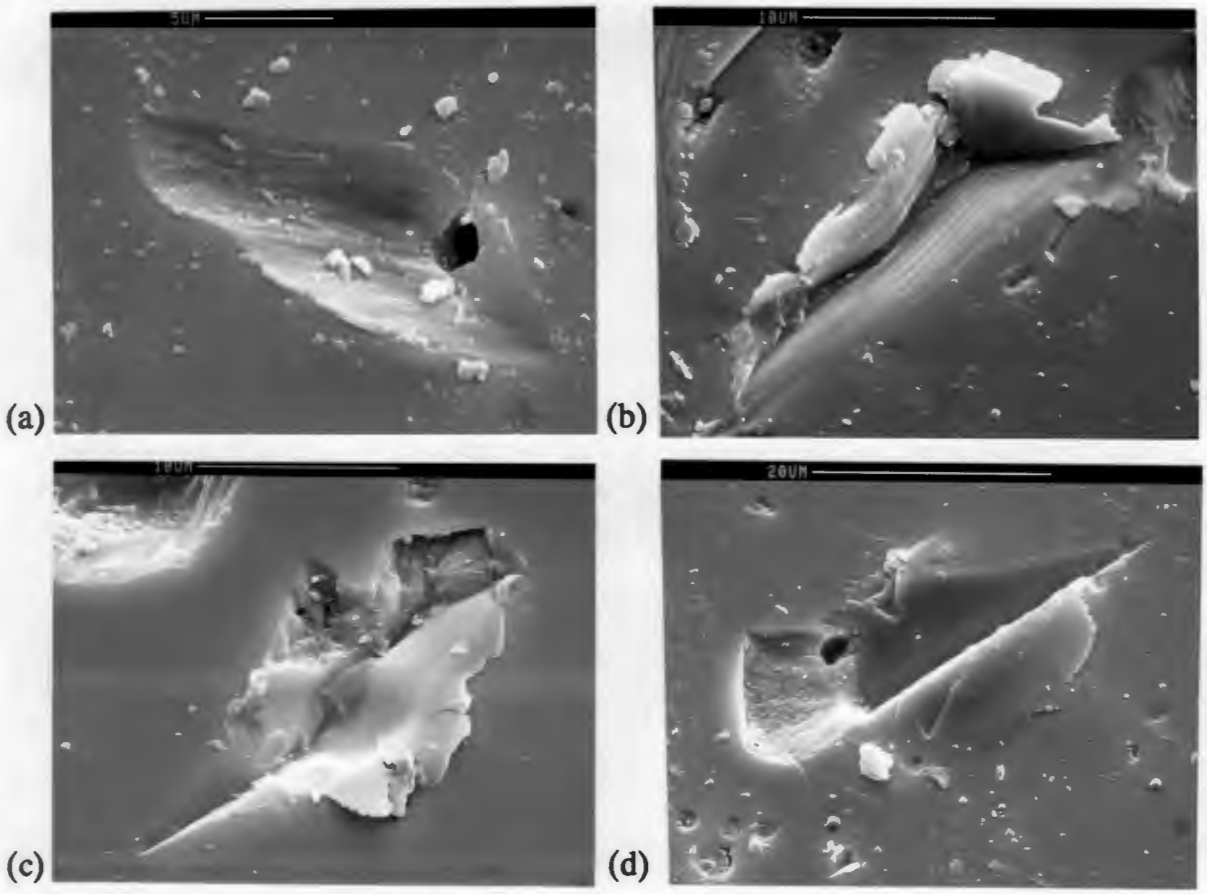

Figure 5.2 ***SEM micrographs of single impact sites on polished MgPSZ resulting from impact of (a) silica (b) alumina (c) silicon carbide and (d) CDA industrial diamond particles.***

ALUMINA A17

Alumina A17 has a large grain size and high porosity and is susceptible to grain pull-out during automatic polishing, hence the nature of the polished A17 surfaces in the micrographs (fig. 5.3).

The impact of silica particles on A17 results in an elastic target material response with no evidence of cracking or grain ejection. Damage, in the form of crushing and fracture of the erodent particles, resulted in extensive pile-up of silica debris at the perimeters of the contact zones (fig. 5.3a).

The impact of alumina particles on A17 results in small contact areas (5-10 microns) surrounding a central shallow region of plastic deformation (fig. 5.3b).

Evidence of tear drop formation and particle tip fracture has been seen in isolated impact sites.

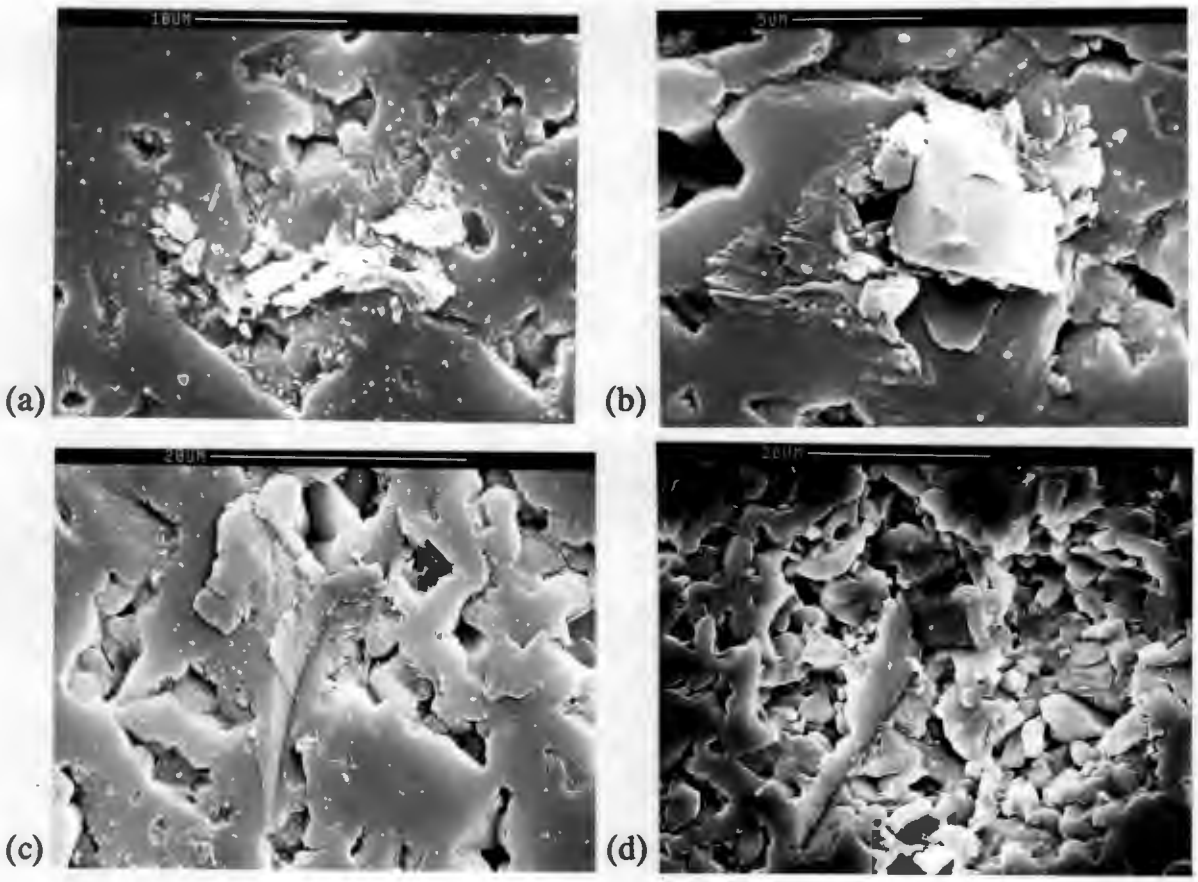

Figure 5.3 *SEM micrographs of single impact sites on polished A17 surfaces resulting from the impact of (a) silica (b) alumina (c) silicon carbide and (d) CDA industrial diamond particles.*

The impact of silicon carbide particles on A17 results in long, narrow impact sites (10-20 microns)(fig. 5.3c). Grain ejection and lateral cracking (<5 microns) can be seen in some impact sites.

The impact of the ultrahard CDA diamond particles results in a small central region of plastic deformation surrounded by extensive intergranular lateral spallation and grain ejection (fig. 5.3d).

SYALON

The impact of silica particles on Syalon results in an elastic target material response and fracture of the erodent particles resulting in the formation of flattened platelet-like debris (fig. 5.4a).

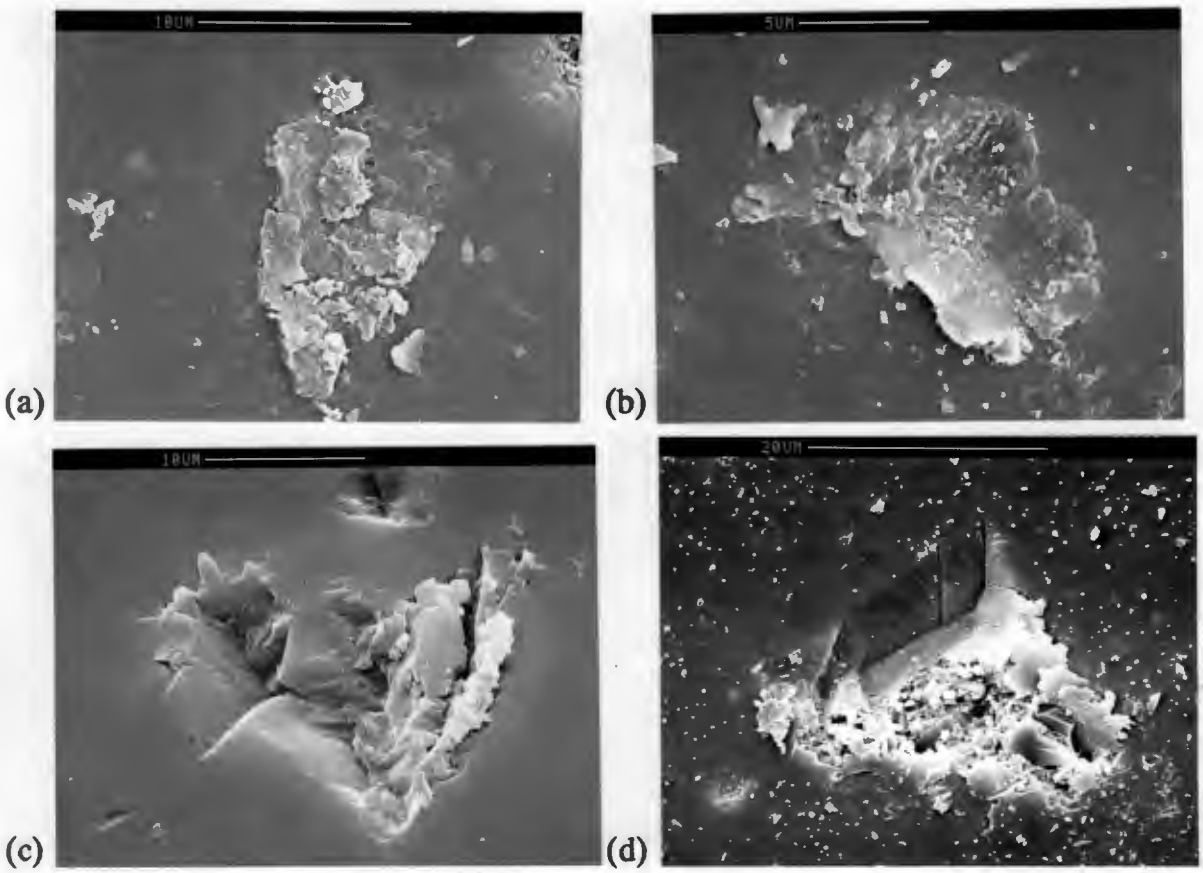

Figure 5.4 *SEM micrographs of single impact sites on polished Syalon surfaces due to the impact of (a) silica (b) alumina (c) silicon carbide and (d) CDA industrial diamond particles.*

The impact of alumina particles on Syalon results in superficial plastic deformation and limited lip formation. Abrasive wear, adhesion of flattened erodent debris and melting features can be seen in many of the impact sites (fig. 5.4b).

The impact of silicon carbide particles on Syalon results in extensive lip formation and grain flattening (fig. 5.4c). A small amount of lateral spallation (1-2 microns) can be seen at the sides of some impact sites.

The impact of CDA particles on Syalon results in deep indentations (15 microns) surrounded by limited lateral cracking (< 10 microns) and spallation (fig. 5.4d).

TZP

Soft silica particles impacting on TZP cause a small amount of superficial plastic deformation. The eroded surface is covered in flattened plates of erodent debris (fig. 5.5a).

Impacting alumina particles on TZP cause elongated plastic cutting-type craters (10-15 microns) with extensive lip formation, grain flattening and intergranular tearing. Rumpling of the surface occurs ahead of the exit side (fig. 5.5b). Tear drop and stringer formation, particle tip fracture and limited intergranular spallation can be seen in isolated impact sites.

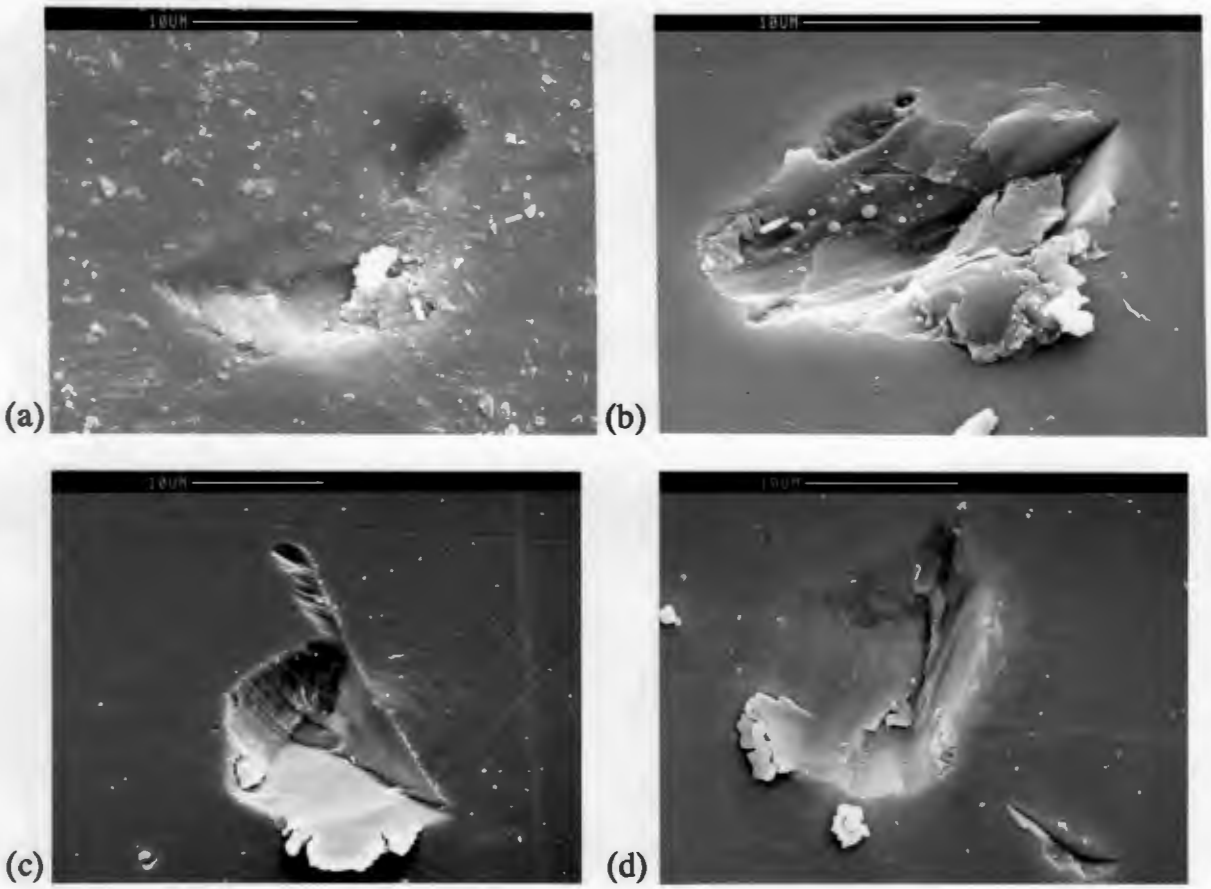

Figure 5.5 ***SEM micrographs of single impact sites on TZP polished surfaces resulting from the impact of (a) silica (b) alumina (c) silicon carbide and (d) CDA industrial diamond particles.***

The impact of the hard silicon carbide and CDA diamond particles on TZP cause elongated punching-type craters and the formation of small lips of material. There is evidence of abrasive wear, surface rumpling and grain flattening in isolated impact sites. There is a small amount of secondary erosion due to the reimpact of CDA fragments (fig. 5.5c&d). CDA diamond particles cause less plastic

deformation in the impact sites compared with the impact of silicon carbide particles.

ALUMINA A16

The impact of the softer silica and alumina particles cause superficial damage in the surfaces and there is no evidence of fracture. Particle damage, in the form of plastic deformation and fracture, results in flattened erodent debris adhering to the target surfaces (fig. 5.6a&b). Melting features were seen in both instances.

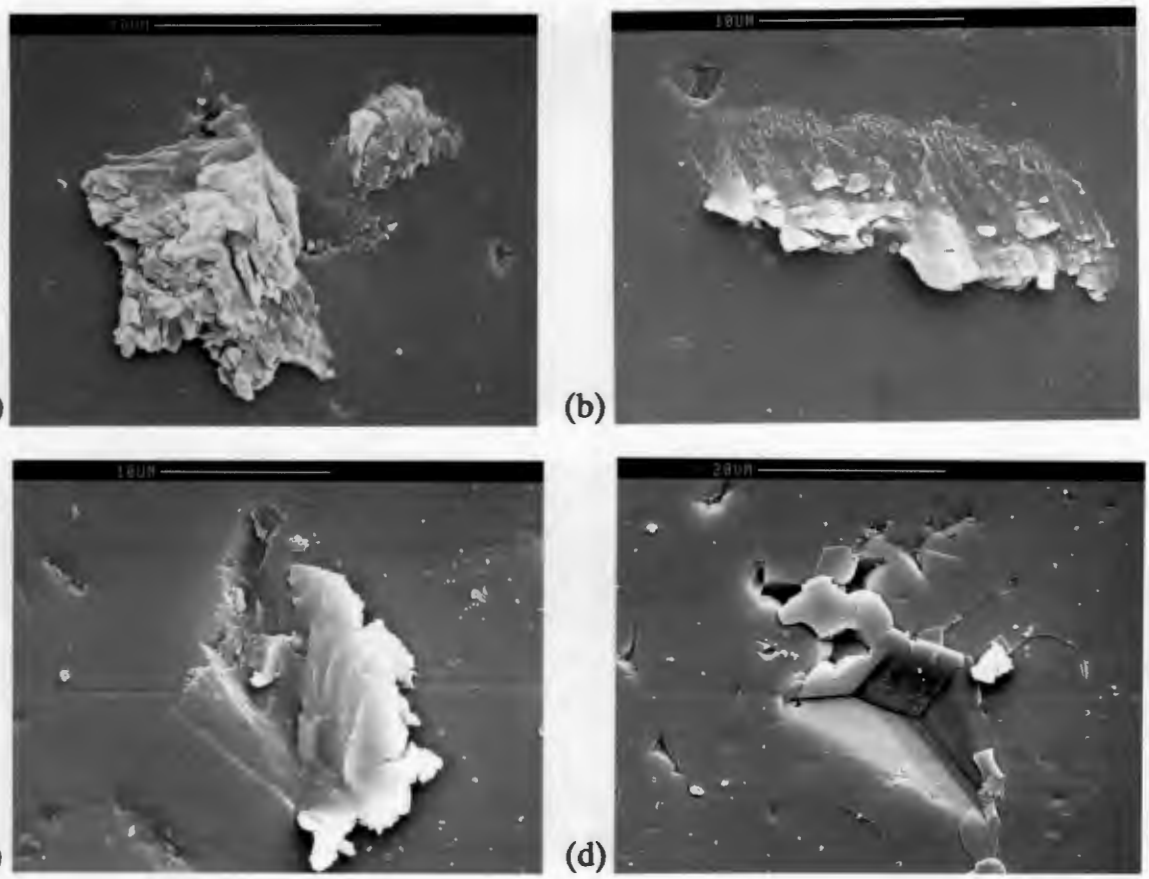

Figure 5.6 *SEM micrographs of single impact sites on polished A16 surfaces due to the impact of (a) silica (b) alumina (c) silicon carbide and (d) CDA industrial diamond particles.*

The impact of silicon carbide particles on A16 results in small, deep plastic craters (10 microns) surrounded by inter- and trans-granular lateral cracking (fig. 5.6c). Abrasive wear and melting features can be seen in some of the impact sites.

The impact of CDA particles on A16 results in well defined plastic indentations (15-20 microns) surrounded by extensive intergranular lateral cracking and grain

ejection (fig. 5.6d). There is evidence of slip on the surfaces of some grains at the exit sides of the impact sites.

R-ALUMINA

The soft silica and alumina particles cause superficial damage on impact on R-alumina. In both instances, the adhesion of crushed erodent debris to the target surface indicates extensive particle fracture (fig. 5.7a&b). Melting features were seen in isolated impact sites.

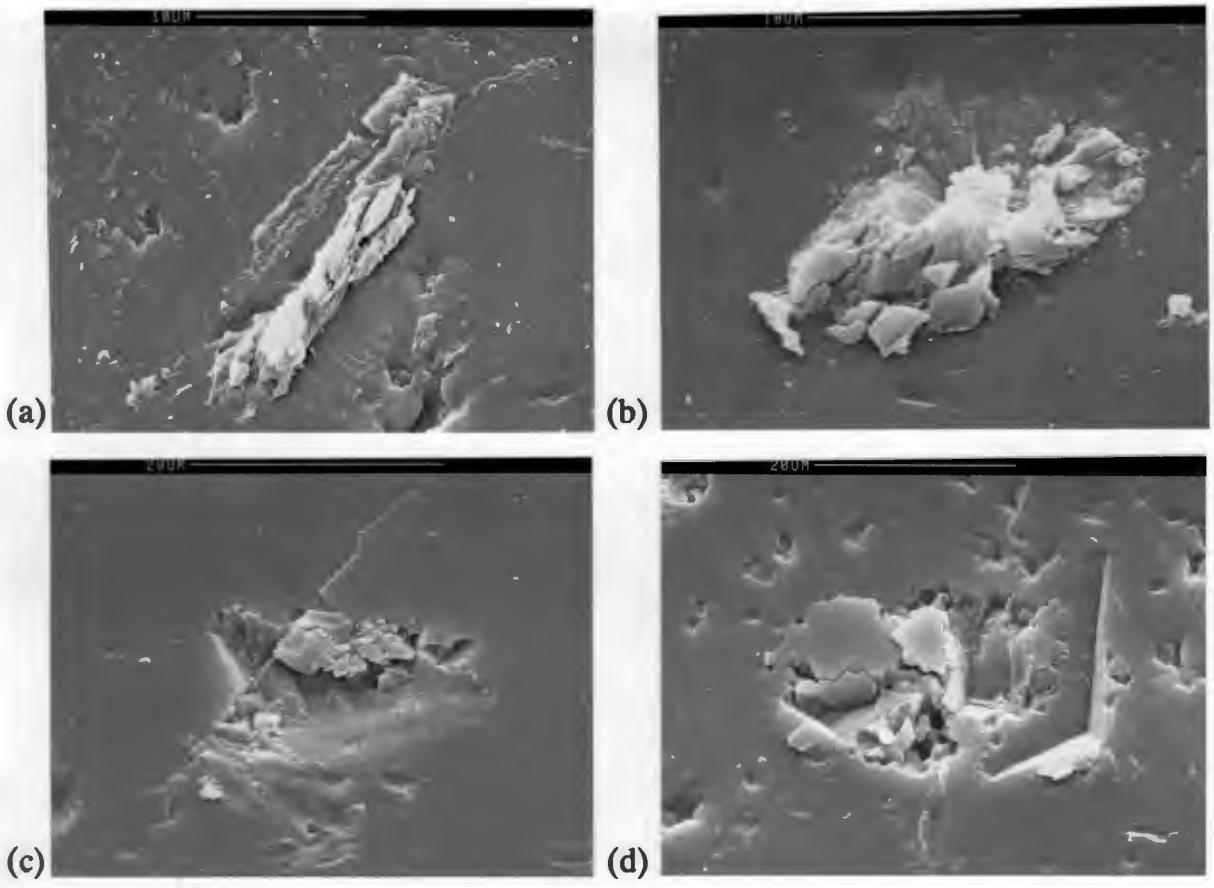

Figure 5.7 *SEM micrographs of single impact sites on polished R-alumina surfaces due to the impact of (a) silica (b) alumina (c) silicon carbide and (d) CDA industrial diamond particles.*

The impact of silicon carbide particles on R-alumina is characterised by central regions of shallow plastic deformation surrounded by trans- and inter-granular lateral cracking (5 microns), radial cracking and grain ejection (fig. 5.7c). Tear drop and stringer formations can be seen in isolated impact sites.

The impact of CDA particles on R-alumina results in well defined plastic indentations (10-15 microns) surrounded by extensive intergranular spallation

(20 microns)(fig. 5.7d). There is evidence of secondary erosion in the form of indentation and cracking (<2 microns) due to the reimpact of CDA fragments.

5.3 FRACTOGRAPHY OF STEADY STATE EROSION SURFACES

The steady state erosion rate of a material is determined by the dynamic properties of the surface layer. The virgin surface is altered by the successive impact of erodent particles which cause strain hardening, residual stresses, microfracture, the inclusion of particle fragments, surface roughening and possibly dynamic recovery.

SEM examination of the steady state surfaces of the target materials provided information about the modes and mechanisms of erosion. It was found that although the steady state damage was similar to single impact damage sites there were significant differences. The soft, tough materials experienced enhanced surface plasticity and lateral cracking was much more prevalent in the brittle aluminas. Some SEM micrographs have been selected to demonstrate the topography of the steady state surfaces.

THE EROSION OF MgPSZ, SYALON AND TZP

The steady state surfaces of the softer, tougher target materials namely, MgPSZ, Syalon and TZP were very plastic and similar in appearance to eroded metallic surfaces.

Fig. 5.8 Steady state erosion surface of MgPSZ after erosion by CDA particles showing two plastic gouging indents, shearing of the highly deformed material and a 'machined' chip (bottom left). There is a small amount of transgranular fracture beneath the deformed material (bottom right).

The removal of material from MgPSZ appears to arise from a mechanism of shearing and chip formation reminiscent of the machining of metals and to a lesser extent from transgranular concoidal fracture (fig. 5.8). The transgranular fracture

surfaces were hard to distinguish from the deformed material due to their rough and porous nature.

Syalon erodes by a combination of intense surface plasticity, intergranular spallation (fig. 5.9) and the formation of platelet-like debris. The plasticity of Syalon is very obvious in the steady state surfaces and may be assisted by heating of the material during impact.

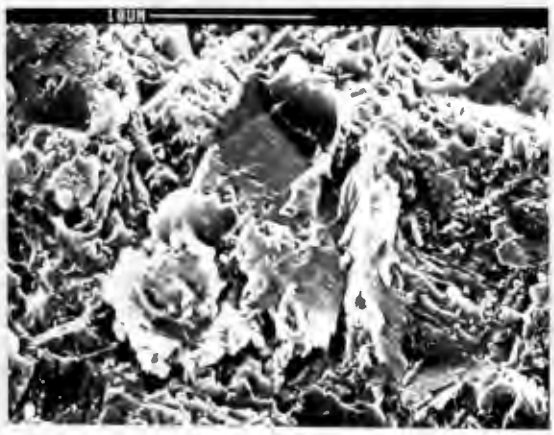

Fig. 5.9 Steady state surface of Syalon after erosion by CDA particles demonstrating the intense surface plasticity of this material. The plastic zone is surrounded by a small zone of intergranular fracture.

TZP erodes by a combination of surface plasticity and intergranular spallation. The surface plasticity is not as marked as in the Syalon and is confined to a thin surface layer (fig. 5.10) as are the shallow lateral vents.

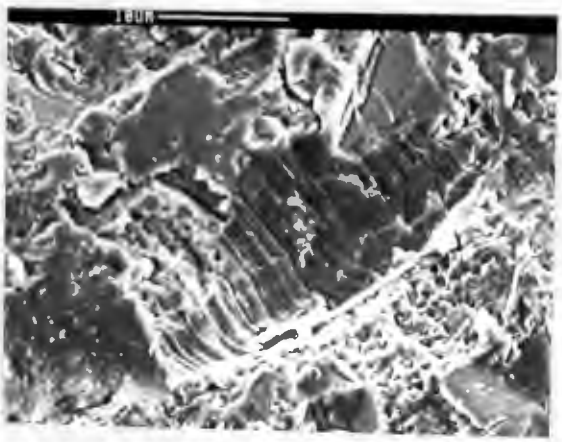

Fig. 5.10 Steady state erosion surface of TZP after erosion by CDA diamond particles showing the thin skin of surface plasticity overlying a zone of intergranular fracture.

THE EROSION OF ALUMINA

The steady state erosion surface of alumina A17 after impact by silica particles consists of a large areas of intergranular spallation surrounding small areas of irreversible deformation (fig. 5.11).

The erosion of R-alumina and alumina A16 by the soft, rounded silica particles results in the formation of a layer of crushed and deformed erodent and target debris and isolated grain ejection (fig. 5.12).

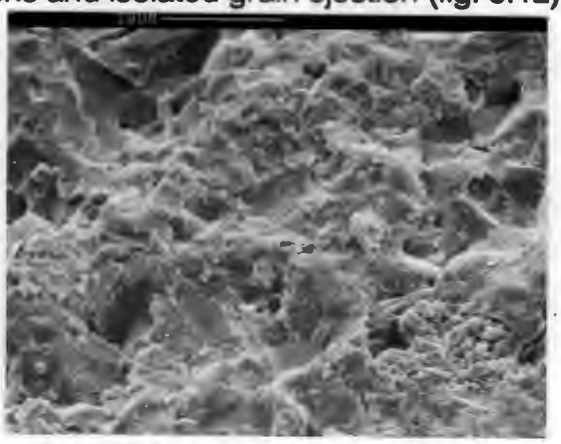

Fig. 5.11 Steady state surface of A17 after erosion by silica particles resulting in small regions of plastic deformation and compaction surrounded by extensive intergranular spallation.

The steady state erosion surfaces of the alumina target materials after erosion by alumina, silicon carbide and CDA diamond particles are epitomised by small central regions of plasticity surrounded by extensive intergranular spallation (fig 5.13&14). The extent of the plasticity and spallation varies slightly with each erodent/target combination.

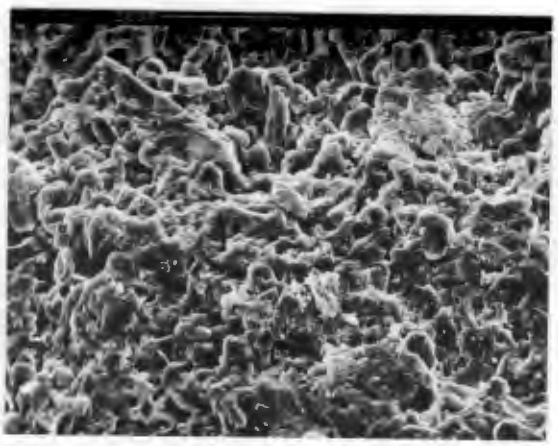

Fig. 5.12 The steady state erosion surface of A16 after erosion by silica particles. There is a surface layer of crushed and plastically deformed material and grain ejection.

Erosion by alumina and silicon carbide particles cause similar amounts of plasticity in the A16 and R-alumina surfaces (fig. 5.13). These central zones of plasticity are often associated with melting features and it is probable that heating enhances the surface plasticity (fig 5.13b).

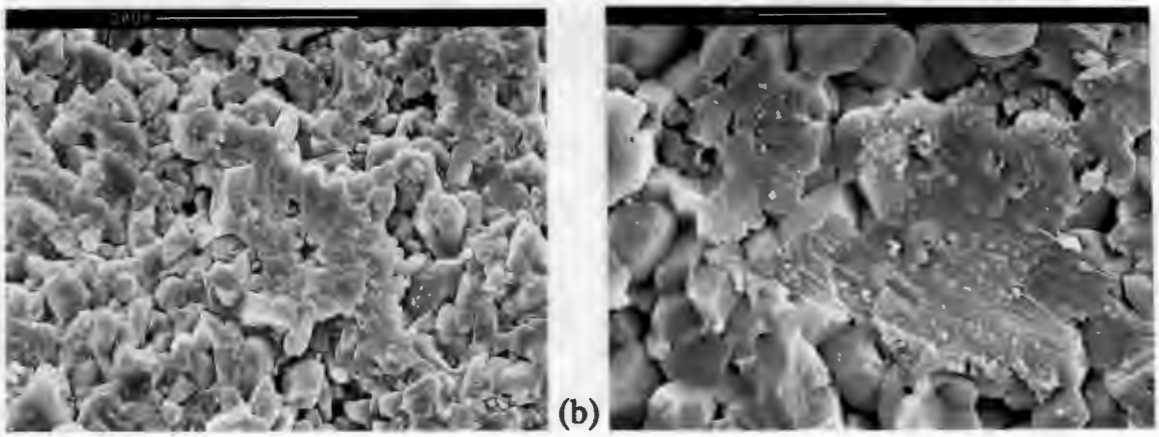

Figure 5.13 *SEM micrographs of the steady state surfaces of (a) A17 eroded by alumina particles and (b) R-alumina eroded silicon carbide particles.*

No melting features were seen in the steady state surfaces of the alumina target materials after erosion by CDA particles. The central zones of plasticity are smaller and intergranular spallation is more extensive (fig. 5.14).

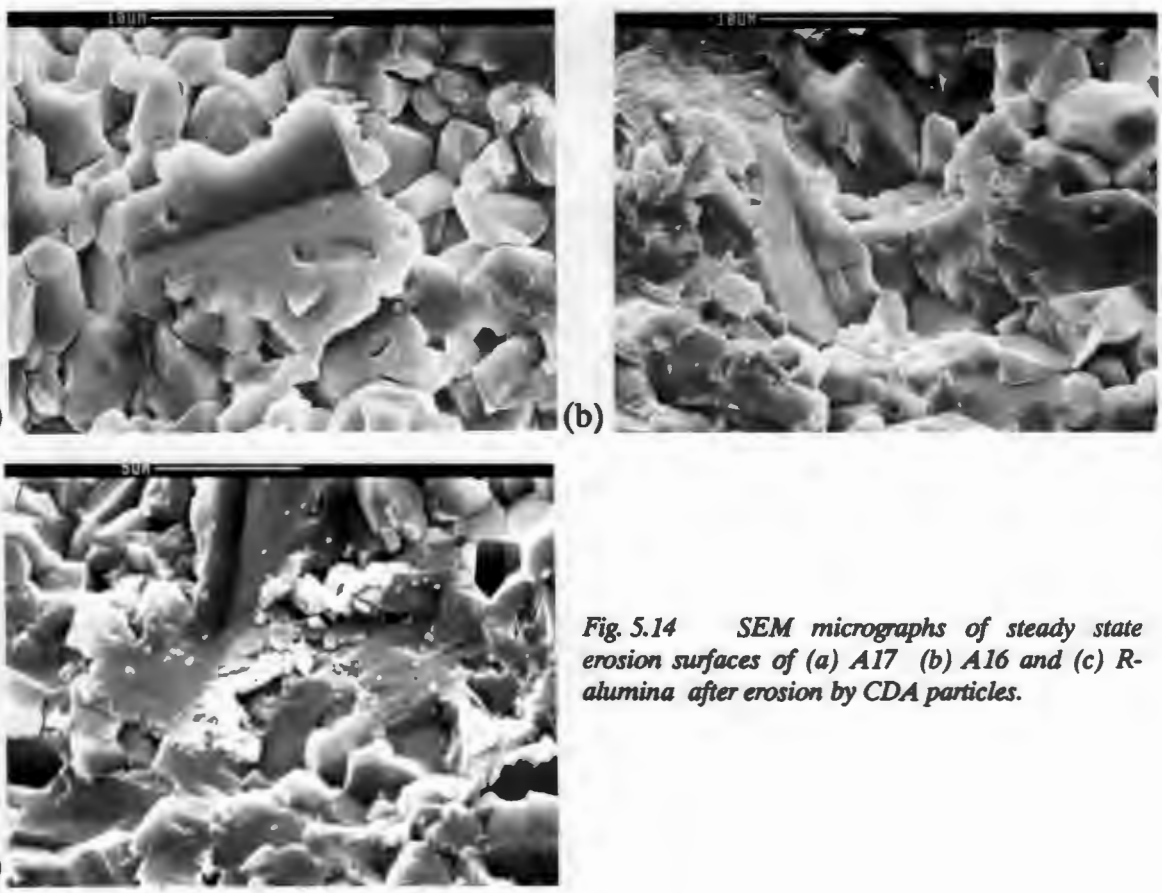

Fig. 5.14 *SEM micrographs of steady state erosion surfaces of (a) A17 (b) A16 and (c) R-alumina after erosion by CDA particles.*

THE EROSION OF THE ULTRAHARD MATERIALS

The erosion of the ultrahard materials is complicated by the presence of two or more phases. The hard crystalline phases resist indentation and the soft, tough phases resist crack propagation. This results in minimal surface damage and very low erosion rates.

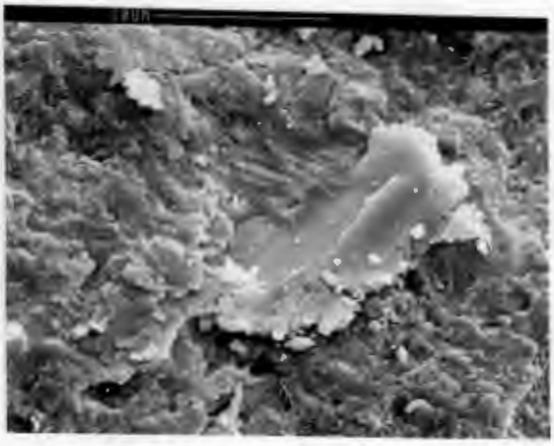

Fig. 5.15 The impact of silicon carbide particles on Syndite 002 results in smearing of the softer cobalt phase and/or the erodent.

After erosion by copious amounts of silica erodent there was no apparent damage in the surfaces of the ultrahard materials and no significant mass losses were recorded ($<10^{-7}$ cm^3/g). The silica particles were prone to crushing and fragmentation on impact resulting in piles of silica debris that did not adhere to the surfaces and were easily removed by ultrasonic cleaning.

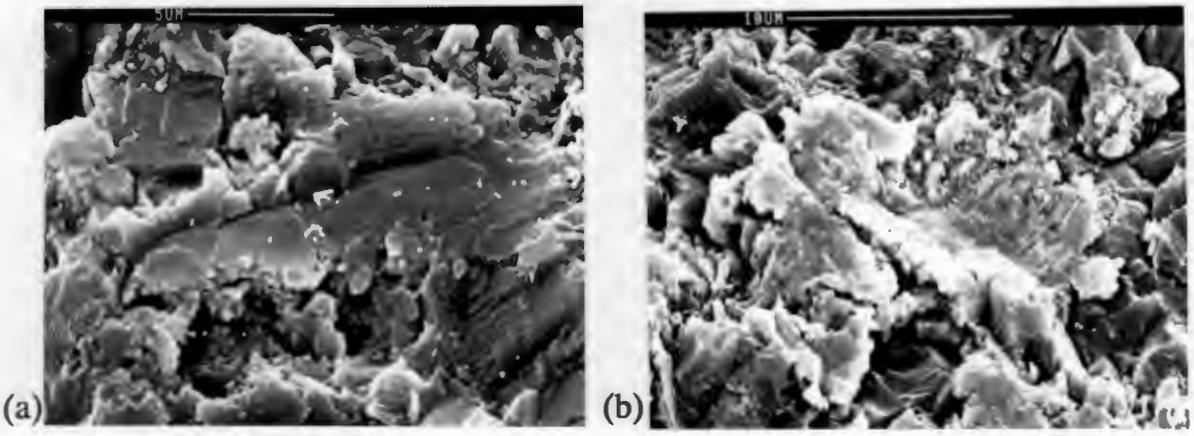

Figure 5.16 (a) The impact of CDA particles on Amborite results in smearing and extrusion of the aluminium binder phase and fragmentation and ejection of the CBN grains (b) The impact of CDA particles on Syndite 025 resulting in plastic deformation of the cobalt binder and fragmentation and ejection of the hard diamond skeleton.

The erosion of the ultrahard materials by alumina particles caused no evident damage in the hard, crystalline phases, extrusion of the softer cobalt phase and

smearing of the softer alumina particles across the surface. It is probable that the low mass losses recorded were due to the extrusion of the softer cobalt phase.

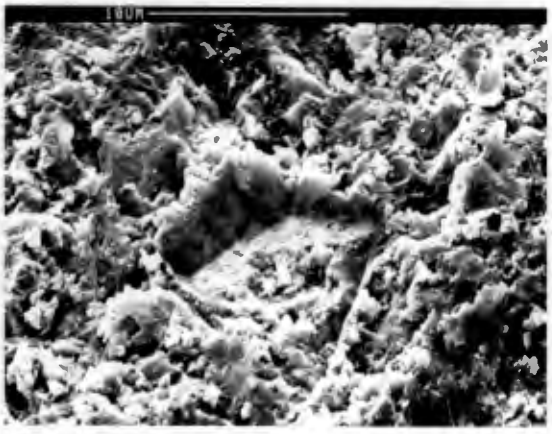

Fig. 5.17 The impact of CDA particles on Syndite 002 results in isolated punching-type indents due to crushing of the diamond and deformation of the cobalt binder.

The erosion of the ultrahard materials by silicon carbide particles resulted in smearing and extrusion of the softer phases and/or the erodent particles and slight crushing of the harder crystalline phases (fig. 5.15). No significant mass losses were recorded, and it is thought that the embedment of silicon carbide particle tips counteracted any target mass losses.

The erosion of Amborite and Syndite 025 by CDA diamond particles resulted in extrusion and plastic deformation of the softer phases and crushing and ejection of the exposed crystallites (fig. 5.16). Syndite 002 has a small mean path distance between the hard diamond skeleton and the cobalt binder phase is effectively shielded from particle indentation. The impact sites are smaller and the erosion rates are substantially lower (fig. 5.17).

5.4 FRACTOGRAPHY OF THE SPENT ERODENT PARTICLES

Examination of the spent erodent particles provided an insight into the amount of damage that occurred in the erodent particles during impact.

The silica particles were prone to damage in the form of large scale particle fragmentation on impact of all the target materials. The most extensive damage was seen in the silica particles that had struck the tough TZP target (fig. 5.18). Very little damage was seen in silica particles that had impacted the softer MgPSZ target surface.

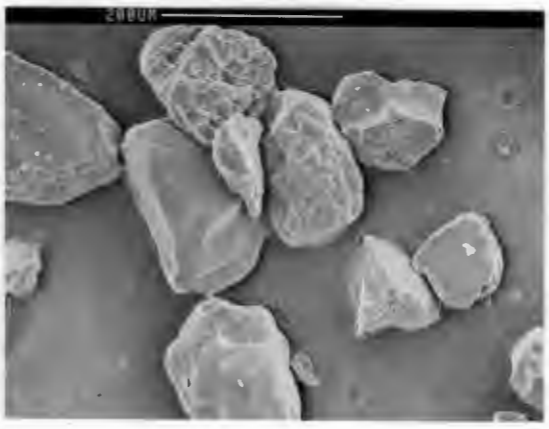

Fig. 5.18 SEM micrograph of spent silica particles after impacting TZP, showing the small silica chips that result from large scale fragmentation.

The sharp alumina particles were susceptible to edge chipping and concoidal fracture on impact, again the most damage was seen in the alumina particles that had impacted TZP (fig. 5.19).

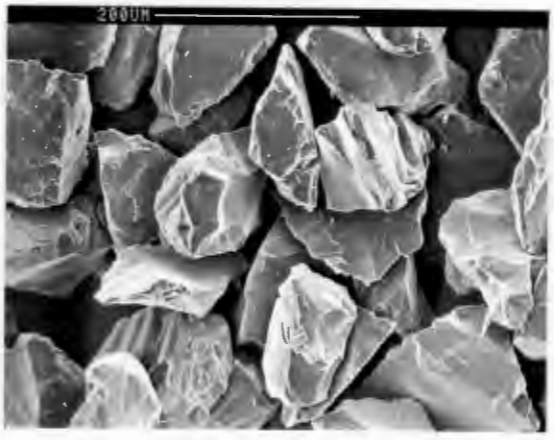

Fig. 5.19 SEM micrograph of alumina particles after impact on TZP showing the concoidal fracture that occurs in the particle tips.

No obvious damage was seen in the spent silicon carbide particles, although small (<5 microns) silicon carbide particle tips were seen embedded in eroded target surfaces. The chipped nature of the virgin particles meant that it was hard to discern any edge chipping in the spent erodent particles.

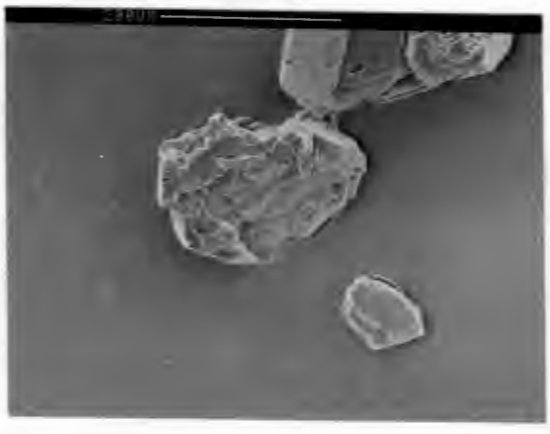

Fig. 5.20 SEM micrograph of a CDA particle fragment formed due shattering on impact on TZP.

The CDA particles were prone to shattering on impact resulting in the small particle fragments that were found among the spent erodent particles after impact on all the target surfaces (fig. 5.20). Secondary erosion damage was a frequent consequence of this fragmentation.

5.5 THERMOMECHANICAL EFFECTS

Tear drop formations, stringers and rivulet markings are considered to be features that occur in impact sites as a result of heating and melting of material during solid particle erosion.

Several micrographs have been selected to illustrate the melting features seen in the impact sites of the eroded surfaces.

FRACTOGRAPHY OF MELTING FEATURES

Extensive survey of a large number of impact sites containing melting features has revealed that melting features are generally seen at the entrance side of the impact sites where the particles are travelling fast, strain rates are high and maximum shear is encountered. The tear drop formations are aligned away from the center of the impact sites (fig. 5.21) and parallel to the direction of particle motion.

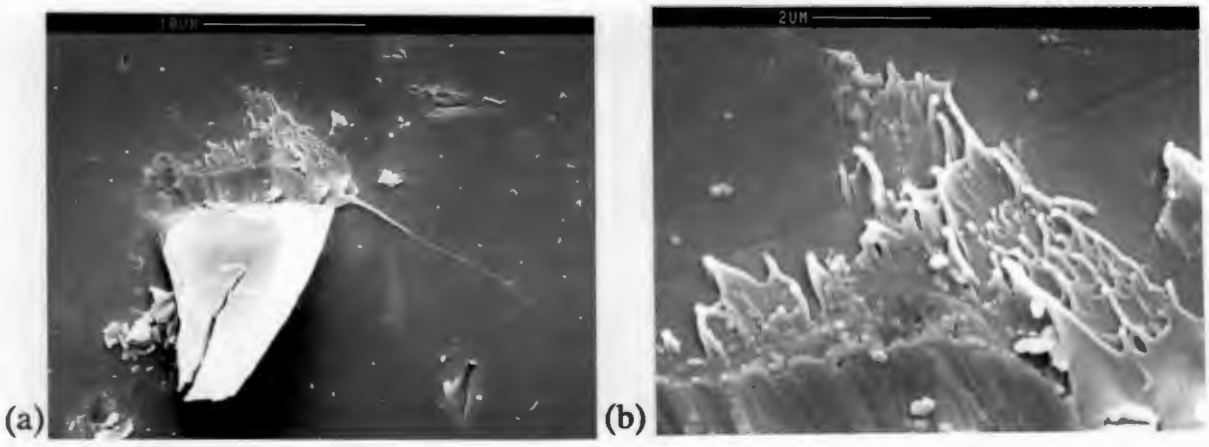

Figure 5.21 *(a) SEM micrograph of an impact site in TZP after erosion by alumina particles. There are globular tear drops at the entrance side and a large alumina chip has adhered to the exit side. There is a long stringer trailing off the right hand side of the impact zone. (b) A closer view of the tear drop formations seen in (a). The tear drops are aligned parallel with the direction of particle motion and away from the center of impact.*

Melting features are often accompanied by the adhesion of erodent particle debris at the exit side of the impact sites and are not always associated with large scale target plasticity (fig. 5.22).

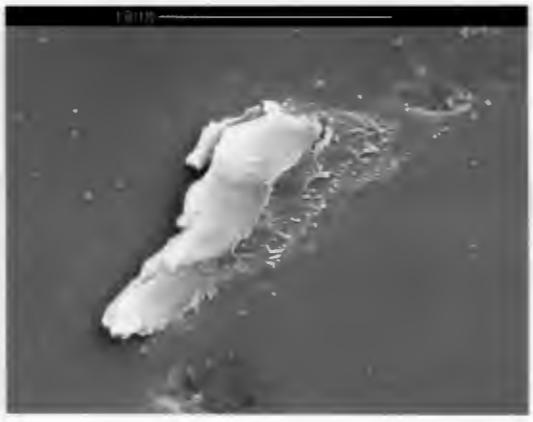

Fig. 5.22 Melting features produced by the impact of alumina particles on alumina A16. There is little plastic deformation of the target surface and erodent particle debris has adhered to the exit side of the impact zone.

Melting features were seen in the three alumina target materials after erosion by silicon carbide particles (fig. 5.23) and these were accompanied by compaction and plastic deformation of surface material. No melting features were seen in any of the other target materials after impact by silicon carbide particles.

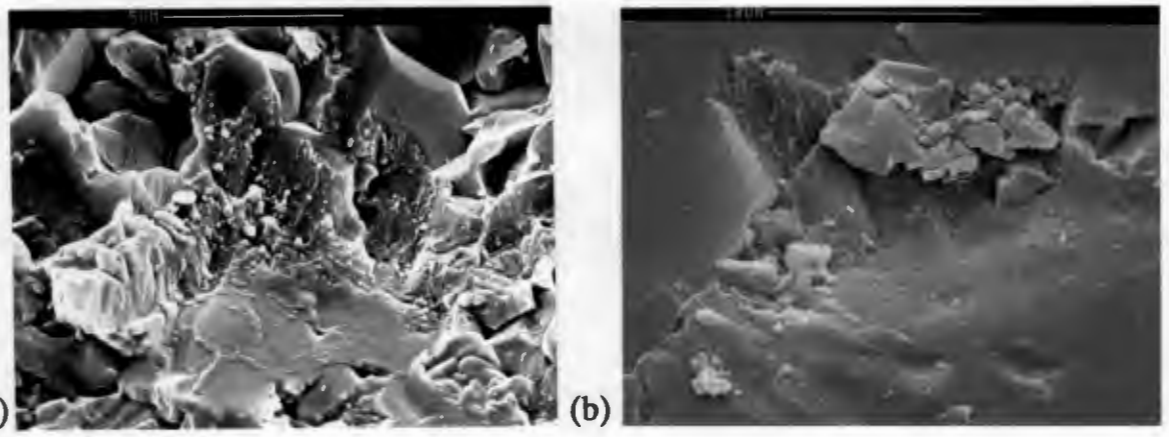

Figure 5.23 Melting produced by the impact of silicon carbide particles on (a) alumina A17 and (b) R-alumina.

No melting was seen in any target materials after by CDA diamond particles. The erodent particle/target combinations in which melting features were seen are listed in Table 5.3. No melting features were seen in the eroded surfaces of the soft MgPSZ or the ultrahard Amborites and Syndites.

Table 5.3 **Melting features were seen in the impact sites of the erodent/target combinations marked (X) below.**

	Target Material					
Erodent	MgPSZ	A17	Syalon	TZP	A16	R-alumina
Silica		X	X	X	X	X
Alumina		X	X	X	X	X
SiC		X			X	X
CDA						

ADDITIONAL EXPERIMENTS

Several experiments were performed in an attempt to measure the temperature rise. A small, quick response thermocouple was connected to the rear of a 1 mm of R-alumina. A 3°C rise in temperature was recorded during repeated erosion tests with silicon carbide particles under standard experimental conditions. Thermal tabs and thermal paint placed on the surface and at the rear of thin sections of target materials did not respond to any temperature increases. It was found that, in the absence of sophisticated equipment, the measurement of the temperatures of hot spots on the target surfaces was precluded by the small areas in which heating occurred.

The erosion tests were viewed in the dark. It was found that most of the target materials emitted a pinkish glow during erosion. The intensity of these light emissions varied for the different erodent/target combinations but was too low to record photographically. Rebounding silicon carbide particles were found to glow after impact on the harder target materials.

5.6 ANALYSIS OF EROSION RESULTS

The steady state erosion rates have been calculated in volume loss of target material per gram of erodent and have been plotted against various target and erodent properties.

THE EFFECT OF TARGET HARDNESS

Erosion by Silica and Alumina

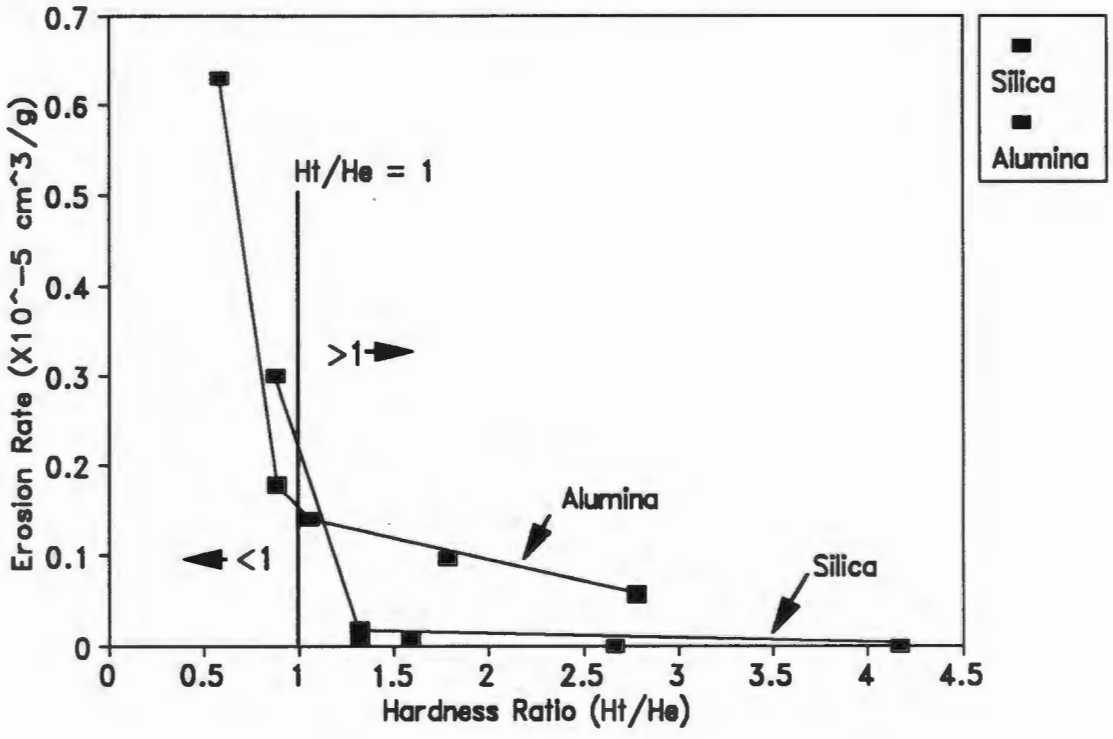

Figure 5.24 *The steady state erosion rates of the target materials have been plotted against target hardness for the two softer erodents, silica and alumina.*

The erosion rates of the target materials have been plotted against target hardness for the two softer erodents, silica and alumina (fig. 5.24). The erodent particles have similar hardnesses to the ceramic target materials (1100 and 1800 H_v for silica and alumina respectively). The erosion rates of the A16 and A17 aluminas are high and have been omitted from the graph for the sake of clarity.

When the erodent particles are slightly harder than the target materials, the erosion rates are relatively high. There is a sudden decrease in erosion rate correlating with a hardness ratio of about unity, after which there is a slight decrease in erosion rate with increasing target hardness. The erosion rates for the alumina erodent particles are consistently higher than the erosion rates for the silica erodent particles.

Erosion by Silicon Carbide and CDA diamond

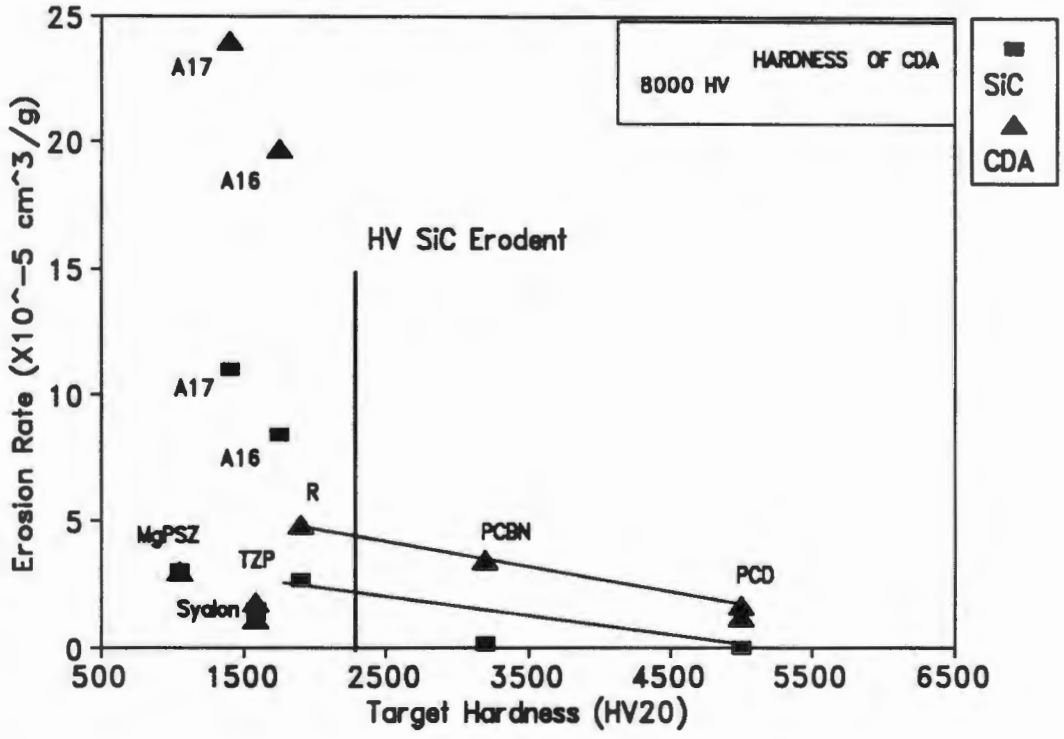

Figure 5.25 *The steady state erosion rates have been plotted against target hardness for the two harder erodents, silicon carbide and CDA diamond.*

Erosion rate has been plotted against hardness for the two harder erodents, the silicon carbide and CDA diamond particles (fig. 5.25). The silicon carbide and CDA diamond erodent particles are harder than the Syalon, zirconia and alumina ceramic target materials (2400 and 8000 H_v respectively).

There is no simple relationship between target hardness and erosion rate. When the target materials are much softer than the particles, the target hardness does not appear to be of importance. However, as the target hardnesses approach the

erodent hardnesses, for example in the erosion of the ultrahard target materials, there is a gradual decrease in the erosion rate with increasing target hardness.

The erosion rates of the three soft, tough ceramic materials, MgPSZ, TZP and Syalon, are low while the erosion rates of the brittle aluminas are an order of magnitude higher. The erosion rates of the ultrahard materials are similar to those of the tough ceramic target materials and decrease slightly with increasing target hardness. The CDA diamond particles are generally more erosive than the silicon carbide erodent particles.

THE EFFECT OF TARGET TOUGHNESS

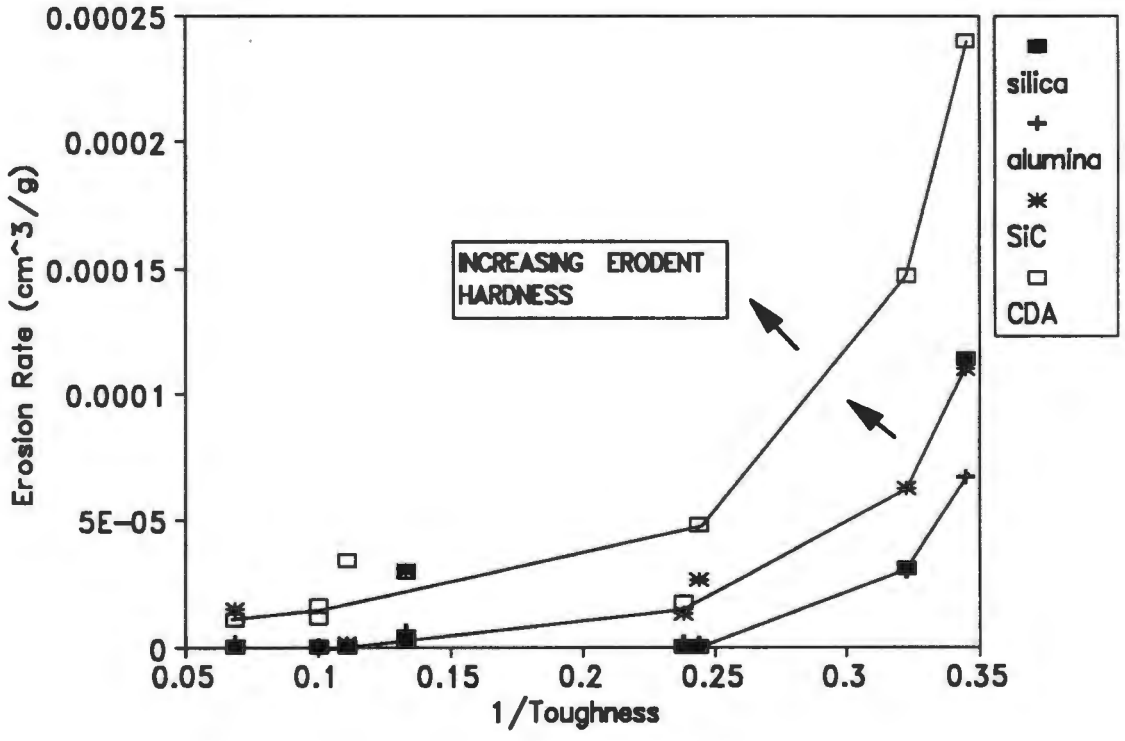

Figure 5.26 *The steady state erosion rates of the target materials plotted against the inverse of target toughness in $MNm^{-3/2}$.*

The steady state erosion rates have been plotted against the inverse of target toughness in $MNm^{-3/2}$ (fig. 5.26). There is an increase in erosion rate with decreasing target toughness. This relationship is most pronounced for erosion by CDA diamond where there is an exponential increase in the erosion rate with

decreasing target toughness. The effect of target toughness on erosion becomes less pronounced with decreasing erodent hardness.

THE EFFECT OF TARGET MODULUS

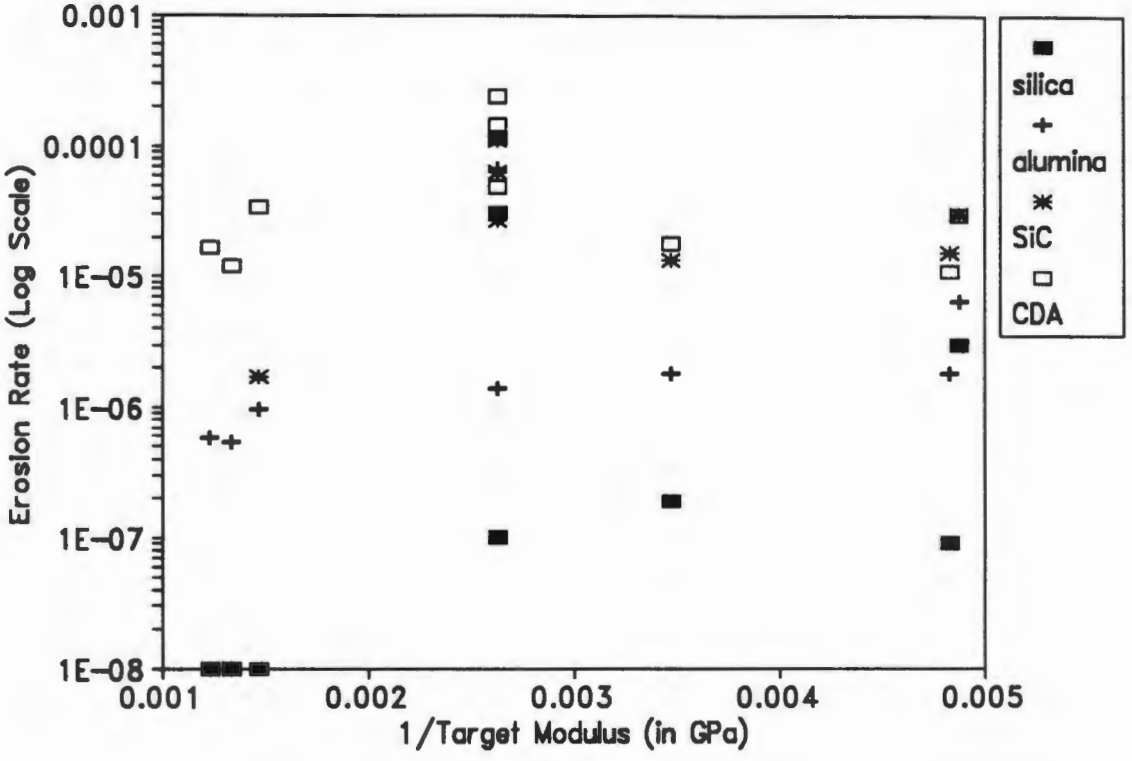

Figure 5.27 *The steady state erosion rates of the target materials plotted against the inverse of target Modulus in GPa.*

The inverse of modulus has been plotted against steady state erosion rate (fig. 5.27). There appears to be no direct relationship between the modulus and the erosion rate. However, it is interesting to note in this logarithmic plot that the erosion rates due to the different erodents become separated out and the silica and alumina particles are much less erosive than the silicon carbide and diamond particles.

THE EFFECT OF GRAIN SIZE

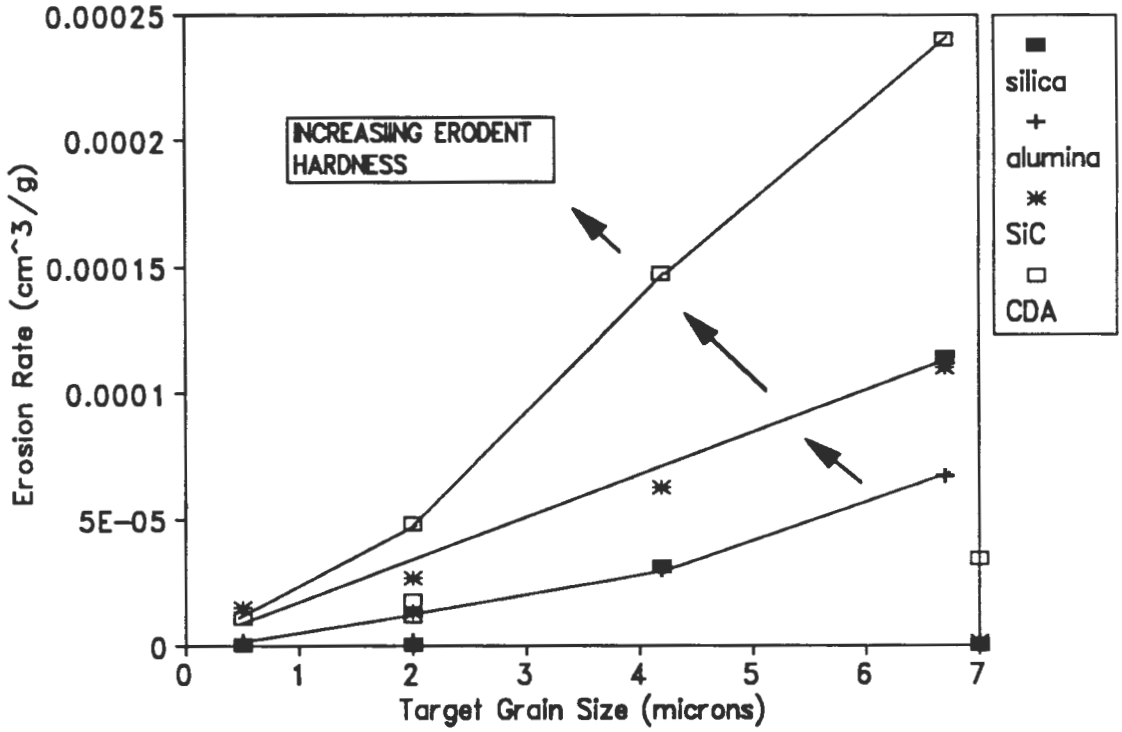

Figure 5.28 *The steady state erosion rates of the target materials have been plotted against the average grain size in microns.*

The steady state erosion rates have been plotted against grain size for the target materials (fig. 5.28). MgPSZ and Syndite 025 have large grain sizes and have been omitted from the graph. With the exception of Amborite, there is an increase in the erosion rate with increasing grain size. This is most prominent in the case of erosion by CDA diamond particles where the relationship is almost linear. The effect of grain size on erosion rate decreases with decreasing erodent hardness.

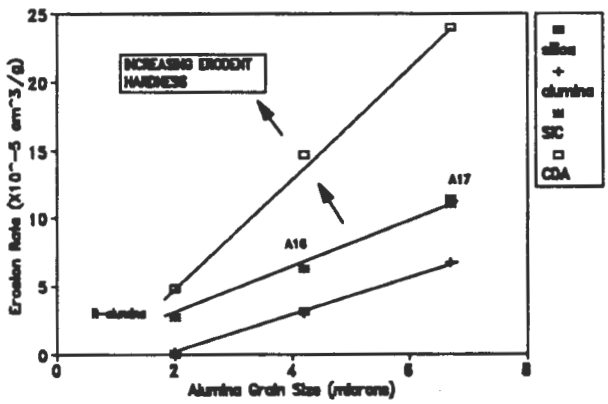

Fig. 5.29 The effect of grain size on the steady state erosion rates of the alumina target materials.

The effect of grain size on erosion is pronounced in the erosion of the non-cubic alumina target materials (fig. 5.29).

THE EFFECT OF POROSITY

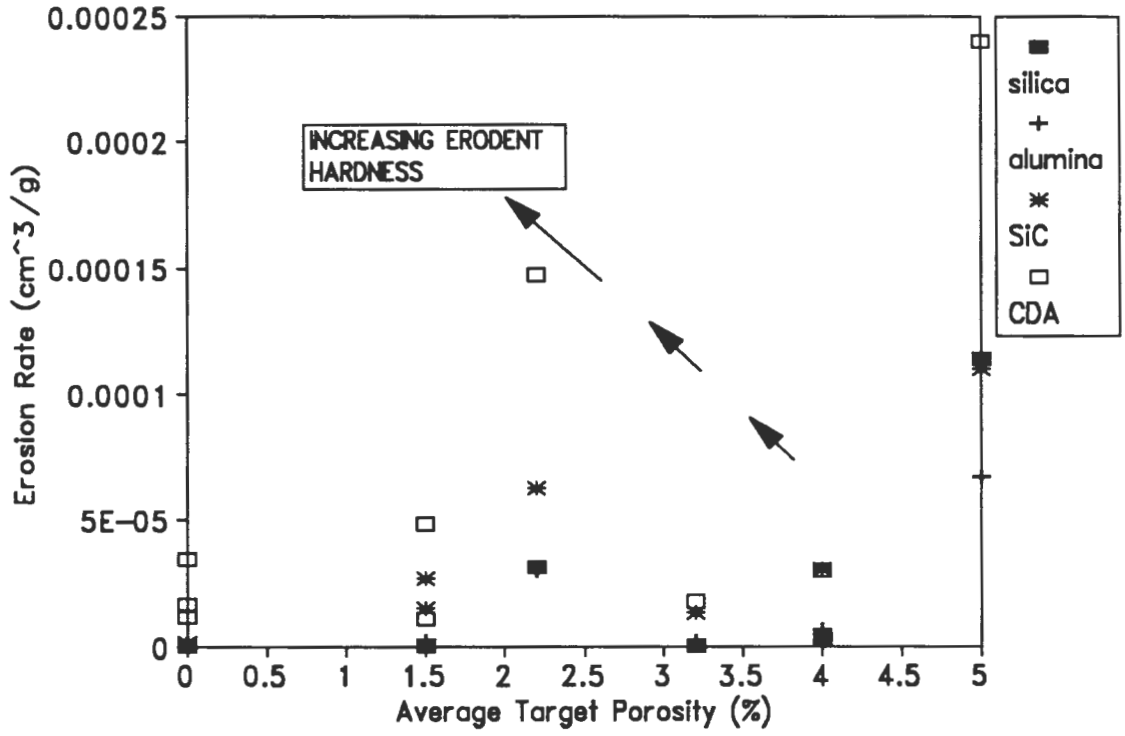

Figure 5.30 *The steady state erosion rates of the target materials have been plotted against their average percentage porosity.*

The percentage porosity of the target materials has been plotted against their erosion rates (fig. 5.30). The ultrahard materials have been assumed to be fully dense. There is a diffuse but general increase in the erosion rates with increasing porosity. This is most obvious for erosion by the hardest erodent, CDA diamond. The porosity becomes less important for the softer erodents.

THE EFFECT OF ERODENT HARDNESS

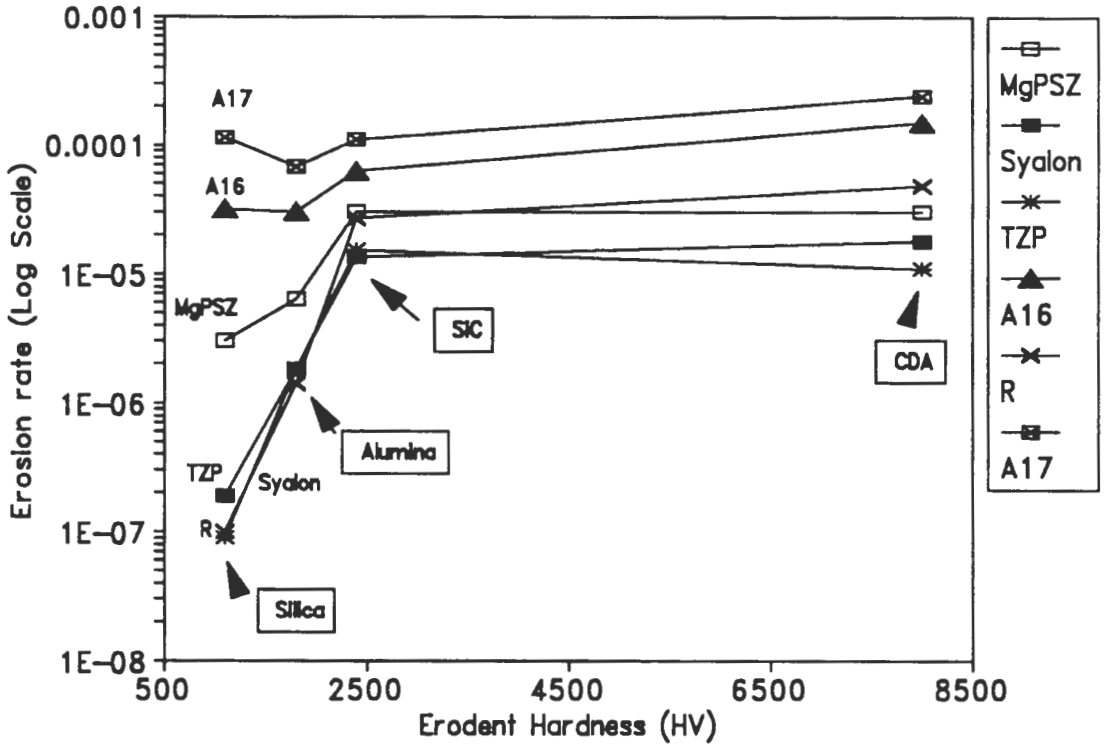

Figure 5.31 *The steady state erosion rates of the ceramic target materials have been plotted against erodent hardness.*

The volumetric erosion rates of the ceramic target materials have been plotted against erodent hardness (fig. 5.31). The erosivities of the two softer erodents, silica and alumina, are low and the erosion rates increase with increasing erodent hardness. There is a saturation point at an erodent hardness of H_v 2400, the hardness of silicon carbide, after which, with the exception of the aluminas, an increase in the erodent hardness has little effect on the erosion rate. The increase in erosion rate with erodent hardness is most pronounced for the most brittle materials, R-alumina and alumina A16. There is a slight decrease in erosion rate from the silicon carbide to the CDA diamond erodents in the toughened zirconia target materials (MgPSZ and TZP).

It is interesting to note that the aluminas become increasingly susceptible to erosion by the soft silica particles as their hardnesses and microtoughnesses decrease and that the silica particles are more erosive than alumina particles for the erosion of alumina A17.

CHAPTER SIX: DISCUSSION

It was found that material removal during the erosion of brittle ceramic materials occurs by a process of dynamic elastic/plastic loading and lateral crack formation. The lateral cracks intersect with each other and the target surface to release chips of material.

6.1 LATERAL CRACK-BASED EROSION

The erosion rate depends primarily on the hardness, toughness and microstructure of the target material and the shape and hardness of the erodent particles. The size and velocity of the particles are assumed to be constant.

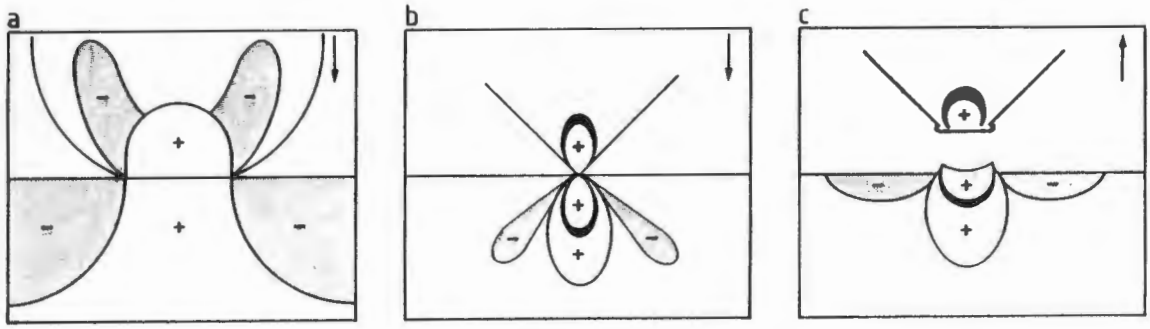

Figure 6.1 *A schematic representation of the stress fields arising from indentation of (a) a blunt indenter and (b) a sharp indenter and (c) the residual stress field after indentation by a sharp indenter (+ compression, - tension and black shading - strong tension).*

The stress fields arising from indentation by differently shaped particles have been simulated by static compression of perspex cutouts and are illustrated in fig. 6.1. The strain rates are much higher for dynamic particle erosion than static indentation but one would expect the pattern of the surface stresses to be similar. Blunt particles have a tendency to induce purely elastic loading and shallow tensile stress fields. Sharp particles are more likely to induce plastic deformation and deeper tensile stresses due to their ability to concentrate the loading forces.

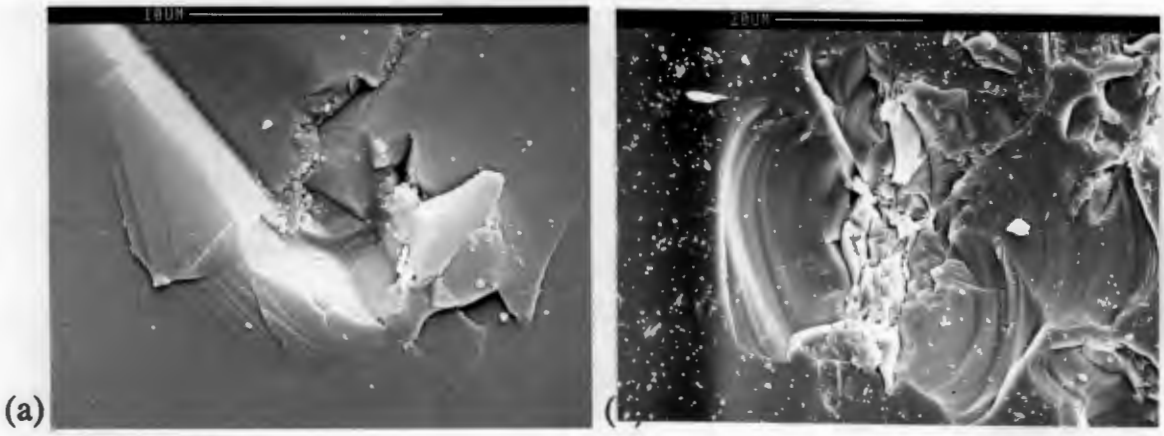

Figure 6.2 ***Single impact morphology of (a) CDA diamond particles on alumina A16 showing a central zone of plastic deformation surrounded by lateral cracking and (b) silicon carbide particles on quartz showing a central zone of crushed material surrounded by lateral fracture The circular patterns are due to semi-circular arrest of the lateral cracks during loading (65).***

The material directly beneath the indenter is subjected to intense compression and may become crushed or plastically deformed. Advanced engineering ceramics are strong in compression and plastic deformation occurs (fig. 6.2a). The extent of plastic deformation is dependent on the loading pressure, the hardness of the erodent, the target hardness and the amount of thermomechanical heating. In amorphous materials and materials that are weak in compression the central zone consists of crushed material (fig 6.2b). The radially orientated mist and hackle patterns on the lateral fracture surfaces of the quartz (fig. 6.2b) clearly indicate that lateral fracture originates from the boundary of the crushed material (64).

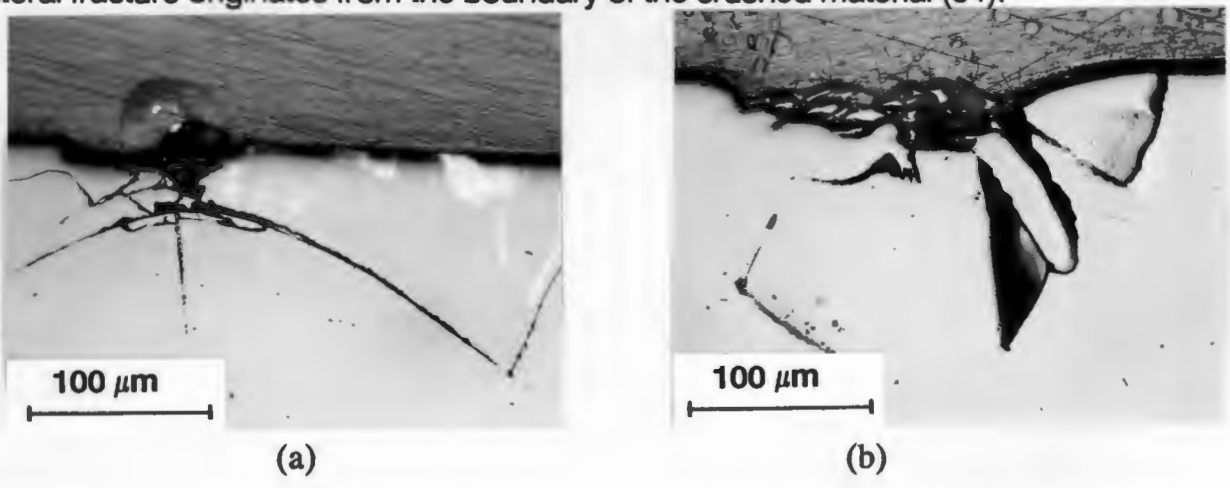

Figure 6.3 ***Cross sections of Vickers indents on polished silica glass under loads of (a) 20 kgf showing Palmquist-type cracking and shallow lateral cracks originating from the interface of the crushed material and (b) 50 kgf resulting in half-penny type cracking and deep lateral cracks.***

On unloading, the material around the central zone of deformation relaxes but cannot return to its original geometry. This causes a residual stress field that arises from elastic/inelastic mismatch at the boundary of the deformed material. Higher loads are required to induce irreversible deformation under blunt or soft indenters. The residual stress fields provide the driving force for lateral crack propagation.

Cross sections of Vickers hardness indentations in glass have been prepared to illustrate the subsurface crack systems associated with elastic/plastic loading. Lateral crack formation may be accompanied by radial cracking at lower loads (fig. 6.3a), and median/radial half-penny cracking at higher loads (fig. 6.3b). Median and radial cracking cause additional material loss due to crack intersection and also introduce deep, subsurface cracks that act as defects for lateral crack initiation. The lateral cracks can be seen to originate from the boundary of the crushed material and propagate parallel to the target surface. Ceramics are weak in tension and the lateral cracks propagate along lines of maximum tensile stress.

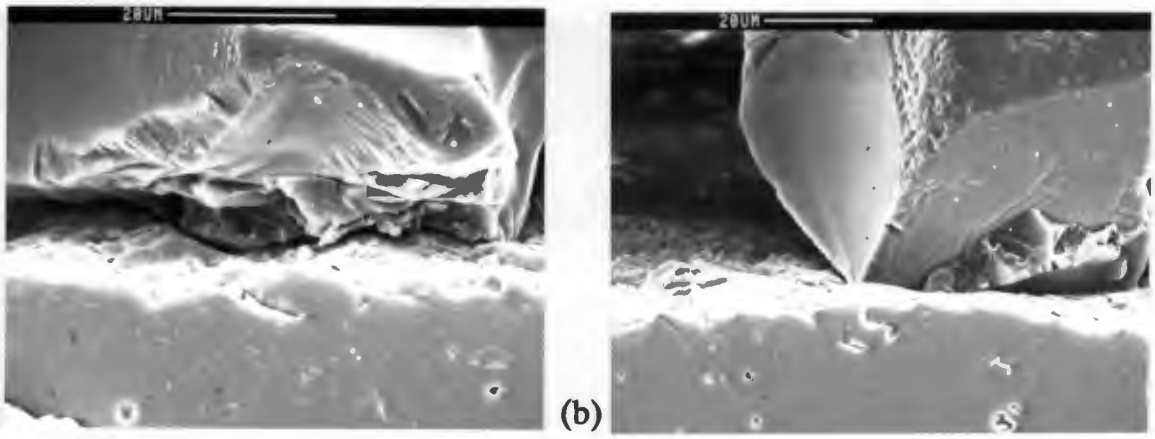

Figure 6.4 ***Cross section of the steady state erosion surface of MgPSZ after erosion by silica particles. The particles have adhered to the surface and illustrate the extent of deformation and cracking in relation to particle size. (a) A blunt particle has a large contact area and very little penetration, note the particle fracture parallel to the contact zone. (b) A sharp particle has a smaller contact region and deeper penetration in the target surface.***

At low loads and during impact by blunt, soft particles the tensile stress fields and associated lateral cracks are located close to the surface resulting in small volumes of material being removed. At higher loads the zones of deformation and tensile stress fields are deeper and lateral cracks initiate and propagate further below the surface releasing larger volumes of material and resulting in higher erosion rates. Cross sections of the steady state erosion surfaces were prepared and examined in the SEM (fig. 6.4). It was found that the scale of damage in relation to the size of the impacting particles was very small.

6.2 THE EFFECT OF TARGET AND ERODENT PROPERTIES ON EROSION

The target and erodent properties that play an important part in erosion are discussed in the following section. The velocity and size of the erodent particles have been assumed to remain constant throughout experimental testing.

THE EFFECT OF TARGET HARDNESS

The hardness of the target material is important in determining the amount of plastic deformation in the impact zone. This, in turn, determines the size and extent of the residual stress fields and ultimately the amount of lateral fracture and material removal.

When the erodent hardness is similar to the target hardness the ease of crack initiation is a rate controlling factor of erosion. In soft, tough materials, for example metals, lateral cracks are nucleated in regions of intense localised shear. In ceramic materials lateral cracks are initiated at defects on the elastic/plastic boundary beneath the zone of irreversible deformation.

Soft particles striking a hard target are themselves prone to plastic deformation and fracture on impact and the initial kinetic energy is apportioned between the target and the particles and less energy is available for erosion. The ability of blunt or rounded particles to concentrate stresses is low and the zones of irreversible deformation are small and shallow. Repeated impacts are required to build up sufficient residual stress to initiate lateral fracture and the erosion rates are low. There is a rapid decrease in the erosion rates as the relative hardness approaches unity (fig. 5.24).

Relatively harder particles are less prone to plastic deformation and fracture on impact, more energy is available for erosion. The particles maintain their integrity on impact and their ability to concentrate stress and initiate fracture is enhanced. Fewer impacts are required to initiate fracture and the erosion rates are higher.

When the erodent particles are much harder than the target material, crack initiation is inevitable and the ease of crack propagation becomes the rate controlling factor (fig. 5.25). A small change in target hardness will not effect the size of the plastic zone or the erosion rate. The ease of crack propagation

depends on the initial energy available for erosion and the resistance of the microstructure to crack propagation. The toughness, grain size and defect density of the target material and the density and shape of the erodent particles become the controlling factors of erosion. Thus the soft, tough target materials, TZP, MgPSZ and Syalon, are more resistant to erosion by hard particles than the harder, less tough aluminas (fig. 5.25).

Thermomechanical heating in the impact zone will result in enhanced plasticity in the impact zone which promotes lateral cracking and soft brittle materials, which soften further during erosion, are most susceptible to erosion, for example A17.

THE EFFECT OF TOUGHNESS

There is a inverse relationship between target toughness and the erosion rate (fig. 5.26). The target toughness and microstructure determine the critical stresses required for crack initiation and resistance to crack propagation.

The importance of target toughness on erosion increases with increasing erodent hardness and is most important in erosion by the ultrahard CDA diamond particles. When the erodent particles are much harder than the brittle ceramic materials, crack initiation is inevitable and the erosion rate is determined by their resistance to crack propagation. As the erodent hardness decreases, the ease of lateral crack initiation becomes the rate controlling factor of erosion and target toughness becomes less important.

The critical stress for lateral crack initiation in a target material is determined by its defect size, toughness and brittleness index $(K_C/H)^2$ (73). The critical stress required for fracture initiation in a tough material is high. A soft, brittle material will be the most susceptible to erosion because the residual stress due to plastic deformation is large and the critical penetration depth for crack initiation is small. In the erosion of alumina A17, for example, crack initiation occurs at lower threshold values than expected.

THE EFFECT OF GRAIN SIZE

The size and aspect ratio of the target grains determine to a small extent the ease of lateral fracture initiation and propagation.

The average defect size in ceramics is usually related to grain size and the largest defects are found in large grained materials. The critical stresses required for lateral initiation will be much smaller in the presence of large defects. The probability of crack initiation will increase with increasing defect density.

Grain size appears to be most important in determining the far field effects of erosion, or the ease of crack propagation, and the effect of grain size on erosion is most pronounced for erosion by the ultrahard CDA diamond particles (fig. 5.28). Intergranular fracture surfaces of fine grained materials have large surface areas and require more fracture surface energy of formation. Interlocking and bridging of grains between opposing fracture surfaces inhibits crack extension. These processes are most effective in materials with fine grained microstructures and irregularly shaped grains with high aspect ratios, for example in TZP and Syalon.

The dependence of the erosion rate on grain size is most pronounced for the erosion of the alumina target materials (fig 5.29). Thermal expansion mismatch of the non-cubic alumina arises in the development of internal stresses when the materials are cooled after sintering. These stresses are greatest in materials with large grain sizes. For the small crack lengths associated with lateral cracking, the microcracks tend to propagate in regions where the internal stresses are tensile, effectively reducing the intrinsic grain boundary toughness of the material. Thus A17 alumina has a large grain size and low erosion resistance.

THE EFFECT OF POROSITY

The porosity of the target materials appears to play a minor role in determining the far field effects of solid particle erosion (fig. 5.30). There is an increase in erosion rate with an increase in porosity and this is most pronounced for erosion by the hard CDA diamond particles.

The pores act as stress raisers by concentrating and intensifying subsurface stresses and enhance the driving force for lateral crack propagation and initiation. The incidence of transgranular lateral fracture in MgPSZ was greatest in the vicinity of subsurface pores.

THE EFFECT OF ERODENT HARDNESS

When the erodent particles are softer than, or of a similar hardness to, the target materials, an increase in erodent hardness results in an increase in the erosion rate (fig. 5.31). The particles are prone to plastic deformation and/or fracture and the amount of energy available for plastic deformation is decreased. The ease of fracture initiation is a rate controlling factor of erosion and repeated impacts are required for material removal to occur. As the hardness of the particles increases, so does their ability to maintain their integrity on impact and the erosion rate increases. There is a saturation erodent hardness at 2400 H_v, the hardness of the silicon carbide particles which is harder than the ceramic target materials, after which the particles maintain their integrity on impact and an increase in erodent hardness has little effect on the erosion rate. This effect is similar to the findings of Levy and Chik (37), who performed erosion tests on stainless steel using five different erodent types at 30° and 90° (fig. 6.5).

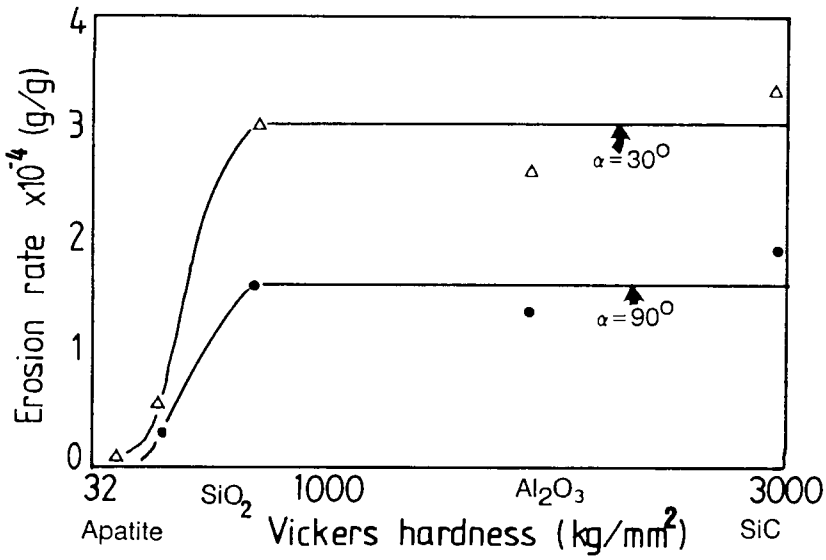

Figure 6.5 *The effect of erodent hardness on the erosion rate of AISI 1020 steel by five different erodents (after Levy and Chik (37)).*

The brittle aluminas become increasingly susceptible to erosion by the softer silica particles as the grain size increases (fig. 5.31). The threshold stresses required to initiate damage in A17 and A16 are lower than expected due to their brittle and defective microstructure and additional parameters come into play: particle flux, grain size and toughness.

6.3 EROSION OF THE TARGET MATERIALS

The erosion mechanisms are discussed in the following pages in order of target hardness. Where the target materials erode by similar mechanisms they have been discussed together.

MgPSZ

The low hardness of the MgPSZ in relation to the erodent particles results in a large central region of irreversible deformation. Thus one would expect a large residual stress field and consequent high driving force for lateral crack propagation and material removal. However the relatively high toughness of the MgPSZ means that firstly, a high critical stress is required for crack initiation and secondly, crack propagation is inhibited. This accounts for the low erosion rates and the high ratio of plastic deformation to fracture seen in the steady state surfaces.

The soft rounded silica erodent particles cause small plastic craters reminiscent of the ploughing-type damage found in metals after impact by spherical particles (fig. 5.2). The silica particles are of a similar hardness to MgPSZ and induce insufficient plastic deformation to initiate cracking. Very little fracture is seen in the steady state surface and the erosion rate is correspondingly low. There was a small amount of asperity crushing in the spent silica particles but no large scale damage was seen.

The impact of the harder, sharper particles on MgPSZ results in a combination of large scale plastic deformation and transgranular concoidal fracture and a secondary, more minor erosion mechanism similar to plastic cutting in metals (fig. 5.8). The alumina and silicon carbide particles remained unchanged after impact, although the CDA particles were prone to large scale fragmentation.

An experiment has been performed to compare the erosion rates of MgPSZ and steel at different impact angles (App. 4). It was found that maximum erosion of MgPSZ occurred at normal impact while that of steel occurred at oblique angles. This suggests that although the steady state surfaces of MgPSZ show extensive plastic deformation, the primary mode of material removal is by brittle fracture.

The average grain size of MgPSZ is larger than the size of the impact events and the morphologies of the individual impact sites are dependent on the orientation of

the grains with respect to the imposed stress fields and the presence of pores and grain boundaries . MgPSZ has a large number of inter- and intra-granular pores which concentrate and magnify the residual stress fields. Transgranular fracture was most prevalent around subsurface pores (fig. 6.6).

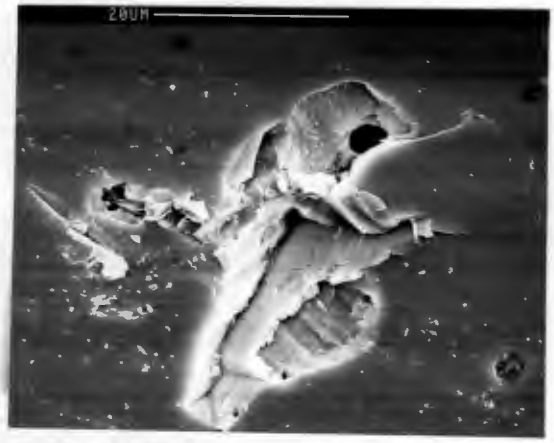

Fig. 6.6 SEM micrograph of a single impact site on a polished MgPSZ surface due to silicon carbide illustrating the initiation of transgranular fracture at sub-surface pores.

A17 ALUMINA

A17 alumina is a low toughness, low hardness ceramic with a relatively large grain size and consequently has a low erosion resistance. Erosion is due to elastic/plastic indentation characterised by central regions of irreversible plastic deformation and compaction, surrounded by extensive intergranular lateral spallation. The steady state erosion surfaces of A17 alumina after erosion by the four erodent types were very similar (figs. 5.11&13), differing only in the ratio of plastic deformation to fracture.

A17 offers little resistance to plastic deformation and consequently the central zones of irreversible deformation are large (fig. 5.3) and set up high residual stresses. The low toughness of A17 coupled with its defective microstructure means that the critical stresses required for crack initiation are small. The low toughness and large grain size offer little resistance to lateral crack propagation and account for the low erosion resistance of this material. In addition, thermomechanical heating in the impact sites results in enhanced plastic deformation.

There was large scale damage in the soft, friable silica particles after impact of alumina. A small amount of damage was seen in the spent alumina particles which are slightly harder but of a similar toughness to alumina A17. No damage was seen in the hard, tough silicon carbide particles but there was large scale fragmentation of the hard, friable CDA diamond particles.

The erosion of A17 alumina by silica particles results in anomalously high mass losses compared to erosion by alumina (Table 5.1) and may be explained in terms of the particle flux. The individual alumina and silica cause damage on a similar scale and few impacts are required to initiate and propagate fracture. The silica particles are much less dense than the alumina particles and, for the standard mass feed rate, the particle flux of silica is higher and thus more silica particles strike the surface and cause damage.

SYALON

Syalon is a strong, fine grained ceramic alloy that work hardens. It has an intergranular phase of yttria aluminium garnet (YAG).

Particle impact causes extensive surface plasticity and material is lost due to intergranular lateral spallation and platelet formation (fig. 5.9). Platelet formation is most pronounced for the impact of the softer rounded silica particles and surface plasticity is most pronounced for the impact of CDA diamond particles on Syalon. Thermomechanical heating may account for the enhanced surface plasticity.

Platelet formation may be explained by the fact that the Syalon is susceptible to work hardening. Repeated impact causes work hardening in subsurface material while concurrent thermomechanical heating causes recovery and softening in the surface layer. The softer surface layer of material is compacted between the impacting particles and the work hardened subsurface layer and results in the detachment of plates of material by a fatigue process (fig. 6.7). Bellman and Levy (12) discuss a similar process for the erosion of metallic surfaces.

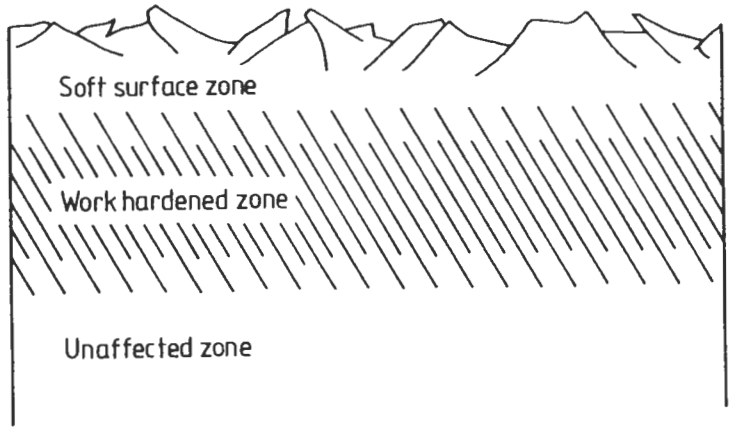

Figure 6.7 *The formation of a soft surface layer overlying a harder, deformed subsurface layer (after Bellman and Levy (12)).*

The high erosion resistance of this material may be explained by its resistance to lateral crack initiation and propagation. Syalon has a relatively high hardness and therefore the residual stresses due to elastic/plastic mismatch are small. In addition, Syalon has a low porosity and a fine grained microstructure and high critical stresses are required for crack initiation. The size of the grains are small in relation to the impact event and Syalon has a polycrystalline toughness response which is higher than the single crystal value. The grains themselves have a high aspect ratio and interlocking of the grains of opposite fracture surfaces inhibits crack extension, further enhancing the toughness (fig. 6.8).

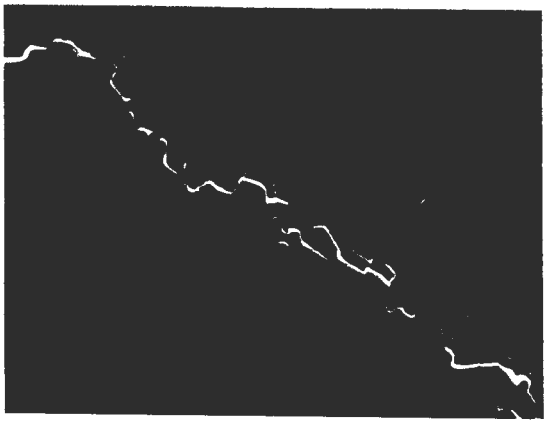

Fig. 6.8 An intergranular crack on a polished Syalon surface illustrating the interlocking of grains between opposing fracture surfaces which results in enhanced toughness.

TZP

The good erosion resistance of TZP may be explained in terms of its high hardness, superior toughness and fine grained microstructure. The amount of irreversible deformation in the impact zone is small and as a consequence the residual stresses are also small. The critical stresses required for the initiation of lateral cracking in TZP's tough, fine grained microstructure are high. Lateral crack propagation is inhibited by its high toughness, fine grain size and transformation of the tetragonal grains. A large amount of fracture surface energy is absorbed in the formation of the fine grained intergranular fracture surfaces (fig. 5.5) and grain interlocking between opposing fracture surfaces further enhances the microtoughness.

Transformation of the tetragonal grains occurs in the tensile stress fields that drive lateral crack formation, and absorbs some of the fracture energy. The volume increase associated with the t-m transformation causes compressive stress fields that counteract the tensile stress and close the crack tips. An example of the transformation of the tetragonal precipitates may be seen in etched

macrohardness indentation (fig. 6.9). Directly beneath the indentation transformation has been suppressed by residual hydrostatic compression.

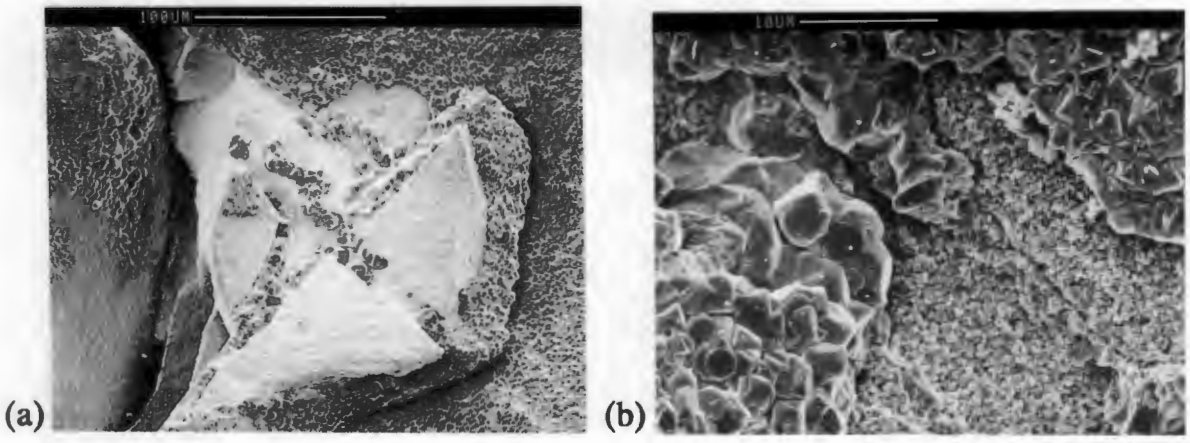

Figure 6.9 *(a) The center of a hardness indent on polished TZP after etching to reveal the microstructure. The central semicircular white area consists of tetragonal grains that have been prevented from transforming by the compressive component of the residual stress field. The larger grains consist of transformed material that has been subjected to residual tensile stress. (b) A close up to compare the size and morphology of the untransformed and larger transformed grains.*

Transformation toughening becomes increasingly more effective in a larger stress field. The impact of harder erodent particles on polished TZP surfaces results in surface rumpling around the impact site due to the 3-5% volume increase associated with the stress-induced t-m transformation. No rumpling was seen after the impact of silica particles (fig. 5.5a) because the size and intensity of the stress field was insufficient to nucleate t-m transformation. CDA diamond particles cause less erosion than silicon carbide particles (fig. 5.31) due to enhanced transformation toughening resulting from the larger stress fields induced by the CDA diamond particles.

A16 AND R-ALUMINA

A16 and R alumina are high purity, high hardness aluminas. Erosion occurs as a result of an elastic/plastic interaction between the particles and target on impact and comprises of plastic deformation and intergranular lateral spallation (figs. 5.6&7). Thermomechanical heating in the impact zones results in enhanced plastic deformation.

A16 is less hard than R alumina and more prone to plastic deformation and the residual stresses arising from elastic/plastic mismatch are higher. In addition, A16 has a larger grain size, higher percentage porosity and lower toughness than

R alumina therefore the critical stresses required for lateral crack initiation are lower and there is less resistance to crack propagation. The erosion rates of A16 are consistently higher than those of R alumina.

The soft rounded silica particles do not impart sufficient energy to the target surface to initiate large scale lateral fracture in A16 and R-alumina (fig. 5.12) and the steady state surfaces are typified by a layer of crushed and deformed erodent/target debris and isolated grain ejection. The erosion rates are correspondingly low.

The impact of the harder, more angular erodent particles results in typical elastic/plastic impact exemplified by zones of irreversible deformation surrounded by intergranular lateral spallation. The ratio of deformation to fracture decreases with increasing particle hardness. This can be explained by the fact that, for the soft particles, repeated impacts are required to initiate fracture and thus there is a higher incidence of plastic deformation on the steady state surfaces. Thermomechanical heating that occurs during the impact of alumina and silicon carbide particles on alumina could account for enhanced plastic deformation in the impact zones and higher residual stresses. Incipient melting could cause a small increase in microtoughness due to crack tip blunting.

AMBORITE AND SYNDITE

The impact of silica particles on the Amborite and Syndite targets caused no evident target damage, although large amounts of loosely attached silica debris suggested extensive erodent damage. No significant mass loss was recorded after erosion by copious amounts of silica. Zeng and Field (67) have recorded mass losses in Amborite and Syndite due to erosion by sand particles travelling a high velocities (75-200 m/s) after long impact durations. Material loss was found to be due to intergranular fracture of the hard diamond and boron nitride phases and extrusion of the softer cobalt, aluminium and aluminium nitride phases. However, for low particle velocities, the amount of energy transferred to the ultrahard target surfaces during the impact of silica particles is too low to initiate damage.

The impact of the harder, more angular particles on the ultrahard materials results in extrusion and compaction of the binder phases and exposure of the crystallites. The alumina particles are sharper than the silicon carbide particles and can fit

between the hard crystallites and attack the softer binder phases more easily which could account for the higher erosivity of the alumina particles.

The silicon carbide particles are harder and stronger than alumina and small mass losses are offset by the embedment of silicon carbide particle tips which penetrate deep into the target surface and are not easily removed by ultrasonic cleaning.

The CDA diamond particles are harder than the CBN phase and cause additional material loss due to the fracture, crushing and ejection of the CBN grains.

The erosion rates of Syndite 025 are consistently higher than those of Syndite 002 and can be explained by the response of the composite microstructure to erosion.

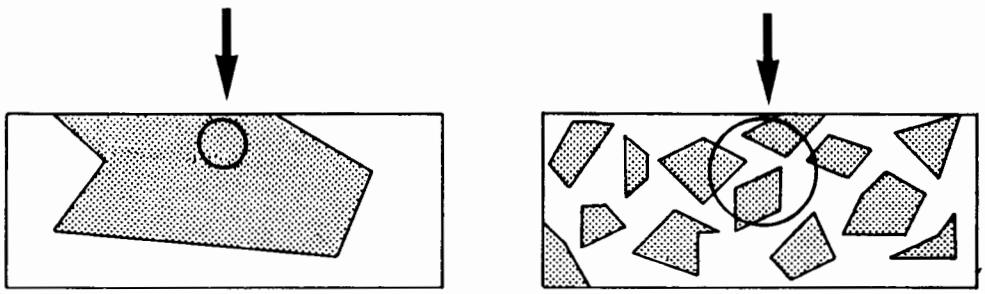

(a) (b)

Figure 6.10 *Schematic representation of the erosion of composite materials where (a) the impact is on the same scale as the microstructure and (b) the impact is much larger than the microstructure (after Hovis et Al (63)).*

The microstructure of Syndite 025 is similar in scale to the impact event and damage may involve plastic deformation of the soft, tough cobalt binder and/or fracture of the hard diamond skeleton. The microstructure of Syndite 002 is much smaller than the area of impacted material and the response involves a combination of the toughness of the cobalt and the hardness of the diamond (fig. 6.10) and the erosion rates will be correspondingly lower. There is also less chance of the particles fitting between the diamond skeleton of Syndite 002 to attack the cobalt phase. The ejection of grains in Syndite 025 will result in a greater volume loss due to its larger grain size.

No melting features were seen in the impact sites and, although there is the possibility of large temperature increases in the impact sites (Table 6.1), the diamond mosaic has a very high conductivity and heat is quickly conducted away

from the impact zone. A small amount of rapid thermomechanical heating in the impact zones may result in fracture of the diamond bridges (66) due to internal stresses arising from thermal expansion mismatch of graphite, diamond and cobalt.

6.4 THERMOMECHANICAL EFFECTS

Melting features were seen in a number of target surfaces after erosion. The following trends arose:-

(i) When the erodent particles are harder than the target material, melting features are accompanied by plastic deformation or compaction of the target surface.

(ii) When the erodent particles are softer than, or of the same hardness as, the target material there is no obvious plastic deformation of the target surface and melting features are often accompanied by adhesion of plastically deformed erodent debris.

(iii) No melting features were seen in eroded target surfaces after impact of CDA diamond particles, although there was large scale deformation in the target surfaces.

(iv) No melting features were seen in MgPSZ target surfaces after erosion by the four different erodent types.

Two theories have been presented to explain heating and melting effects during solid particle erosion and have been treated mathematically in the following pages.

HEATING DUE TO PLASTIC DEFORMATION

Hutchings and Levy (22) assume that the plastic work associated with plastic deformation of a material will be largely dissipated as heat. The temperature rise associated with this heat will be depend on the effects of heat conduction during the impact process. If heat conduction is negligible, the process will be adiabatic and the temperature rise will be determined by the amount of energy dissipated per volume of material which is equal to the mean pressure resisting indentation or the

target hardness (P). The maximum temperature rise (ΔT_{max}) under these conditions may be calculated as (after Hutchings and Levy (22)):-

$$\Delta T_{max} = P/C\rho \qquad \text{(eq. 1)}$$

where ΔT_{max} is the mean adiabatic temperature rise (K)
P target hardness (GPa)
C is the heat capacity of the target material (kJ/kg K)
and ρ is the density of the target material (Mg/m^3).

If the rate of heat conduction away from the impact site is high then ΔT_{max} will be lower than estimated for the adiabatic model (eq. 1). In the extreme case of very high conductivity, the impact is essentially isothermal and no heating occurs. If ΔT_{max} exceeds the melting point of the target material and the conditions are adiabatic, one would expect melting in the impact zone.

Table 6.1 **A summary of the thermal properties and melting temperatures (T_m) of the target materials. ΔT_{max} has been calculated from eq. 1.**

Target material	Hardness (GPa)	Density (Mg/m^3)	Thermal Conductivity (W/mK)	Heat Capacity (kJ/kgK)	Thermal Diffusivity ($X10^{-6}$ m^2/s)	ΔT_{max} (K)	T_m (K)
MgPSZ	10.4	5.7	2.0	0.53	0.662	3470	2800
A17	14.0	3.87	30.0	0.88	8.81	4100	2072
Syalon	15.8	3.3	21.3	0.62	10.4	7700	1830
TZP	15.8	6.1	3.0	0.47	1.05	5520	2800
A16	17.5	3.94	30.0	0.88	8.65	5047	2072
R	18.9	3.98	34.0	0.88	9.71	5396	2072
PCBN	32.0	3.4	100	0.5	58.8	18820	660*
PCD002	50.0	4.2	560	0.52	256	22900	1860*
PCD025	50.0	3.9	560	0.52	276	24650	1860*

* *Melting point of the metal sintering aid*

The thermal properties of the target and erodent materials are listed in Table 6.1. Diffusivity (k) has been calculated from $k = K/(C\rho_t)$ where K is the conductivity, C

the specific heat and ρ the density of the target material (61). The silicon carbide and CDA diamond particles and the ultrahard target materials have high thermal diffusivities. The maximum temperature rise (ΔT_{max}) has been calculated from eq. 1 and is dependent on hardness, heat capacity and density. The hardness of the deformed material ultimately determines the maximum temperature rise and it should be noted that the maximum temperature rise in the soft MgPSZ is only slightly higher than its melting temperature and the maximum temperature rises in the ultrahard materials are an order of magnitude higher than their melting temperatures.

This analysis does not include the effects of heating or heat diffusion in the erodent particles. The thermal properties of the erodent particles are listed in Table 6.2. ΔT_{max} has been calculated from eq. 1. When the erodent particles are softer than the target material one would expect heating to occur due to plastic deformation of the erodent particles. Particles with high heat diffusivities act as heat sinks and the observation of target melting is less likely.

Table 6.2 A summary of the thermal properties of the erodent particles.

Erodent material	Hardness (GPa)	Density (Mg/m^3)	Thermal Conductivity (W/mK)	Heat Capacity (kJ/kgK)	Thermal Diffusivity ($X10^{-6}$ m^2/s)	ΔT_{max} (K)	T_m (K)
silica	11.0	2.63	2.5	0.75	1.27	5580	1710
alumina	18.0	3.99	20.1	0.8	6.3	5640	2350
SiC	25.0	3.21	170	1.0	53	7800	2000
CDA	80.0	3.51	600	0.52	330	43830	3600

From Table 6.2, it can be seen that it is possible for melting features to occur due to the plastic deformation and heating of the erodent particles on impact of a harder target material. The silica and alumina particles are, in general, softer than many of the target materials and have lower thermal diffusivities.

The depth of the zone of plastic deformation, x_p, and the root mean square diffusion distance, x_d, must be compared in order to examine the heat flow during impact. The ratio of x_p/x_d is defined by Hutchings and Levy (22) as:-

$$x_p/x_d = v(r/(3\pi k))^{1/2}(2\rho/(3P))^{1/4} \qquad \text{(eq. 2)}$$

where v is the particle velocity (m/s)
r is the particle radius (m)
k is the thermal diffusivity of the target material (m^2/s)
ρ is the erodent density (kg/m^3)
and P is the target hardness (Pa).

Assuming that the size and velocity of the erodent particles remain constant, eq. 2 may be adapted to define the adiabatic/isothermal boundary ($x_p/x_d = 1$) as a function of the diffusivity and hardness of a given target material, and the density of the specific erodent particles (fig. 6.11).

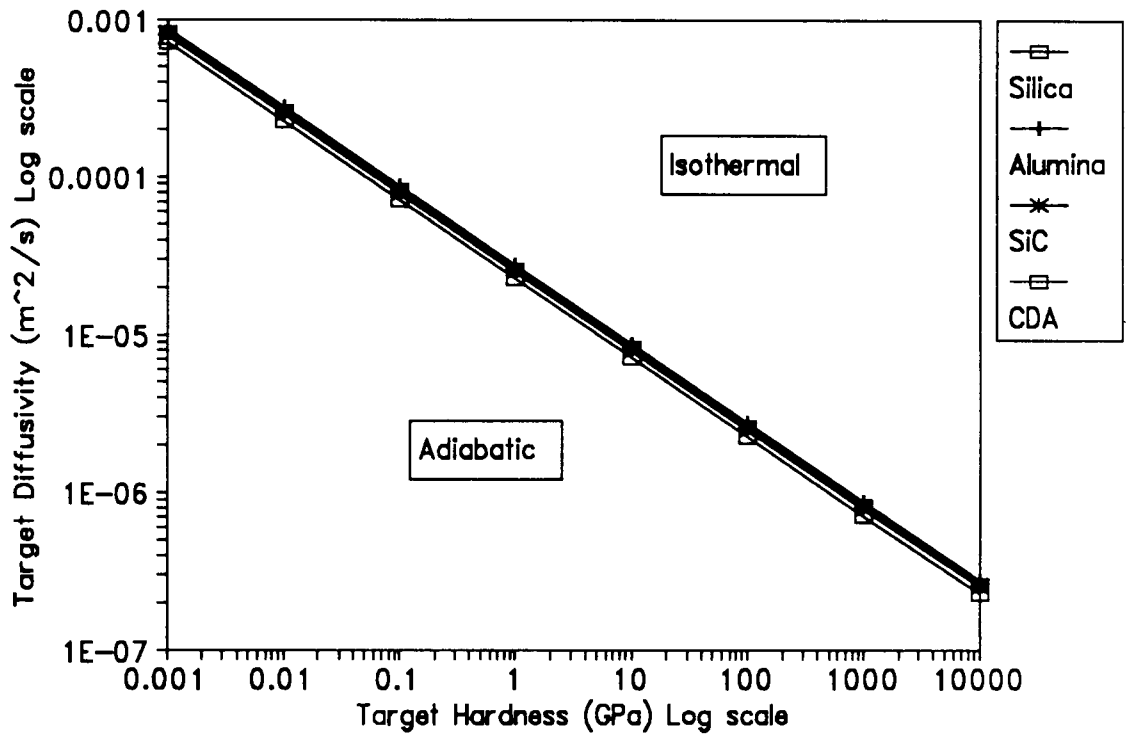

Figure 6.11 *The adiabatic/isothermal boundary calculated for the standardised erosion conditions of erodent particle diameter (100 microns) and particle velocity (40 m/s) (after Hutchings and Levy (22)). The slight variation for each erodent is due to the difference in erodent density.*

The ratios $\Delta T_{max}/T_m$ and x_p/x_d are listed in Table 6.3. It should be noted that for a given target material the ratio $\Delta T_{max}/T_m$ remains constant as ΔT_{max} is dependent on the maximum plastic indentation pressure which is related only to the target hardness. There is a slight variation in the ratio x_p/x_d for a given target material

due to a variation in the erodent densities. The target/erodent combinations for which melting features were seen have been marked (#).

If the ratio x_p/x_d is large, one would expect heating to occur in the impact zone. However, if the ratio x_p/x_d is small, the radius of diffusion exceeds the depth of the plastic zone and heating is not expected to occur. Note that the ratios of $\Delta T_{max}/T_m$ are always greater then one.

Table 6.3 The ratios of $\Delta T_{max}/T_m$ for the target materials and the ratios of x_p/x_d for each erodent/target combination.

Material	$\Delta T_{max}/T_m$	x_p/x_d			
		SiO_2	Al_2O_3	SiC	CDA
MgPSZ	1.24	3.24	3.59	3.40	3.48
A17	1.98	0.83#	0.92#	0.87#	0.89
Syalon	4.23	0.74#	0.82#	0.77	0.79
TZP	1.97	2.32#	2.57#	2.44	2.50
A16	2.43	0.79#	0.87#	0.83#	0.84
R	2.60	0.73#	0.81#	0.76#	0.78
PCBN	28.0	0.26	0.29	0.27	0.28
PCD002	12.3	0.11	0.12	0.12	0.12
PCD025	13.3	0.11	0.12	0.11	0.12

\# *Melting features were seen in some of the impact sites of these erodent/target combinations.*

Where the conditions are adiabatic ($x_p/x_d > 1$) and the ratio $\Delta T_{max}/T_m$ is greater than one, melting of material is expected in the impact sites. The maximum temperatures of the ultrahard materials far exceed their melting points and one would expect heating of material to occur in the impact sites. However, they have very high conductivities, the ratios of x_p/x_d are very low and the impact conditions may be considered isothermal.

The conductivities of the erodent particles have not been taken into account in these calculations and one would assume that some of the heat of plastic deformation will be conducted away by the particles. The silicon carbide and CDA diamond particles have high thermal diffusivities and one would expect the rate of

heat diffusion into the erodent particles to be high and melting is less likely with these erodents.

Thus, where the erodent particles have high diffusivities, the heat flow to the particle during impact becomes important and the equation for x_p/x_d must be adjusted (fig 6.12).

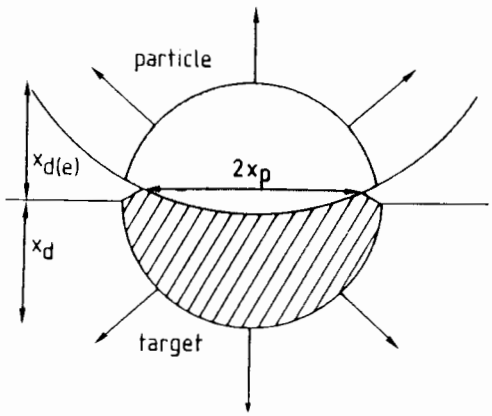

Fig. 6.12 A schematic representation of the heat flow in the target and impacting particle during particle impact.

Melting features were seen in the alumina target materials after the impact of silicon carbide. However, taking into account the heat flow into the erodent particles and the low values of x_p/x_d, one would not expect melting to occur. It has been suggested that the silicon carbide particles are coated with a coherent oxide film (69) which interacts with alumina to form a low melting point eutectic at 1595°C (fig. 6.13) and viscous flow of material would occur at much lower temperatures than anticipated.

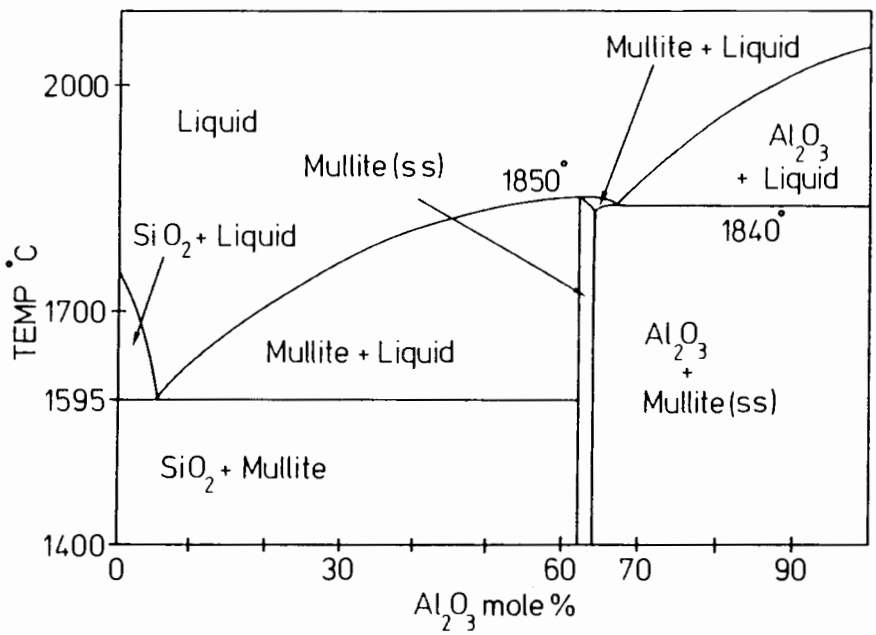

Figure 6.13 The alumina/silicon carbide phase diagram indicating a low melting point eutectic at 1595° C (from Doyle (15).

Melting is anticipated in the impact of MgPSZ as the maximum temperature rise exceeds the melting temperature and the conditions are adiabatic, however, no melting features were seen in the eroded surfaces. This can be explained by the fact that the maximum possible temperature is only slightly greater than the melting temperature and prior to melting the monoclinic phase undergoes a m-t transformation which absorbs some of the energy of plastic deformation in latent heat of transformation.

FRICTIONAL HEATING

Melting features are not always associated with plastic deformation and a theory has been developed to estimate the amount of frictional heat dissipated during purely elastic impact. The true impact angles of the particles are affected by the turbulence created by placing the target in the airstream (fig. 2.10) and most of the impacting particles strike at slightly oblique angles. The maximum indentation pressure and the time of contact for elastic impact of a spherical particle may be calculated from Hertzian equations and thus it is possible to estimate the amount of frictional heating.

The maximum elastic contact pressure (P_E) may be calculated as (from Hutchings (42)):-

$$P_E^5 = (1280/243\,\pi^4)\rho v^2 (1/f(E))^4 \qquad \text{(eq. 1)}$$

where ρ is the density of the sphere (kg/m^3)
and v is the velocity of the sphere (m/s).

f(E), a function of the elastic constants of the particle and target materials, is defined as (from Hutchings (42)):

$$f(E) = (1-\nu_e^2)/E_e + (1-\nu_t^2)/E_t \qquad \text{(eq. 2)}$$

where ν is the Poisson's ratio
E is the Young's Modulus (GPa)
and e,t denote the target and erodent properties.

By symmetry the average elastic contact pressure (P_{av}) exerted by the sphere will be approximately half the maximum elastic loading pressure ($P_{av} = 2P_E$) and, conversely, the total elastic contact time (t_c) will be twice the elastic loading time (t_E):

$$t_E = 1.47\ (5\pi\rho f(E)/4)^{(2/5)} r/v^{(1/5)} \qquad \text{(eq. 3)}$$

where r is the radius of the sphere
and $t_c = 2t_E$.

A sphere striking a surface at an angle (α) will slide a distance (d) before rebounding (fig. 6.14).

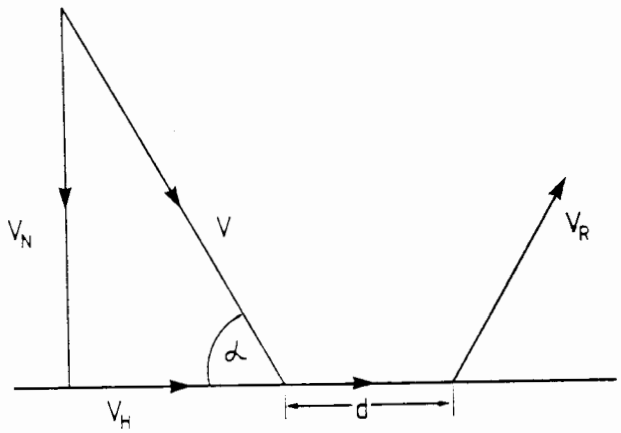

$$d = \cos\alpha\ v\ t_c \qquad \text{(eq. 4)}$$

Figure 6.14 *A schematic representation of the elastic impact of a sphere. The values of v, d and α have been defined.*

The frictional work (W_f) required to slide the sphere a distance (d) under a pressure (P_{av}) may be calculated as:

$$W_f = \mu\ P_{av}\ a\ d \qquad \text{(eq. 5)}$$

where μ is the coefficient of friction
and a is the contact area (m^2).

It is assumed that all of the frictional work is dissipated as heat and the heat diffuses outwards from a central point for the duration of the impact time. The distance (x) diffused by the heat front during the contact time may be calculated as (after Hutchings (42)):-

$$x = (6kt)^{0.5} \qquad \text{(eq. 6)}$$

where k is the thermal conductivity
and t is the diffusion time.

The distance travelled by the heat front will differ according to the thermal diffusivity of the material and for dissimilar erodent and target materials are defined in fig. 6.15.

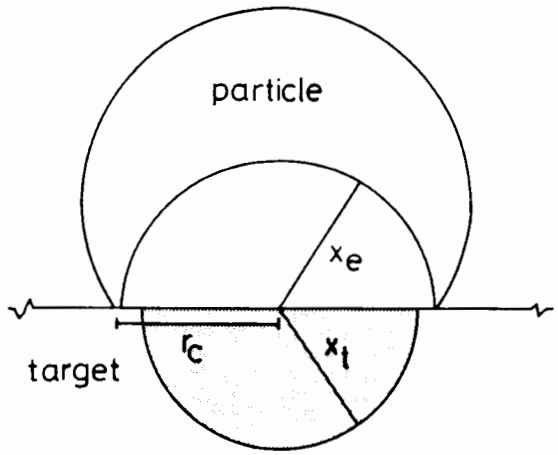

Fig. 6.15 A schematic representation of the thermal diffusion distance of the erodent (x_e) and target (x_t) materials during the elastic contact time (t_c). The radius of contact is r_c.

If the particle and target are treated as two separate hemispheres the masses of material to be heated in each hemisphere may be calculated as:-

$$m = (2/3)\ \pi x^3 \rho \qquad \text{(eq. 7)}$$

where $x = (6kt)^{0.5}$ (from Hutchings (42))
$(2/3)\pi x^3$ is the volume of an hemisphere
and ρ is the density of the material (kg/m^3).

The maximum temperature rise (ΔT) due to frictional heating during elastic impact may be defined as :-

$$\Delta T = W_f/(m_e C_e + m_t C_t) \qquad \text{(eq. 8)}$$

where m is defined in eq. 7
C is the specific heat
and e, t denote erodent and target properties respectively.

The rebound velocity (v_r) of the spherical particle may be calculated from the initial kinetic energy (KE_i) and the energy lost to friction. Thus:-

$$V_r = (2(KE_i - W_f)/m)^{1/2} \qquad \text{(eq. 9)}$$

where $KE_i = 1/2\ mv^2$
$m = (4/3)\rho\pi r^3$ is the mass of a spherical particle
v is the initial velocity
and r is the radius of the sphere.

These calculations have been performed for selected erodent target combinations and the values are listed in Table 6.4.

Table 6.4 **Frictional heating effects of selected erodent/target combinations as calculated from the preceding equations**

Erodent		Alumina	SiC	Alumina	Alumina
Target		Alumina	Alumina	Syalon	MgPSZ
Property	Symbol				
Youngs Modulus (GPa)	E_e E_t	380 380	420 380	380 288	380 205
Poissons Ratio	ν_e ν_t	0.22 0.22	0.18 0.22	0.22 0.23	0.22 0.31
Density (kg/m^3)	ρ_e ρ_t	3990 3990	3210 3990	3990 3230	3990 5740
Impact Angle (^{0})	α	85	85	85	85
Velocity (m/s)	v	40	40	40	40
Contact Area ($X10^{-10}m^2$)	a	3.5	3.5	3.5	3.5
Particle radius ($X10^{-5}$ m)	r	5	5	5	5
Coefficient of friction	μ	0.7	0.3	0.5	0.3
Diffusivity ($X10^{-6}m^2/s$)	k_e k_t	6.3 6.3	53 6.3	6.3 10	6.3 0.66
Specific Heat (kJ/kgK)	C_e C_t	800 800	1000 800	800 620	800 470
f(E) ($X10^{-3}$ 1/GPa)	f(E)	5.0	4.8	5.8	6.9
Max. elastic pressure (GPa)	P_E	14.0	13.9	12.5	10.9
Av. contact pressure (GPa)	P_{av}	7.0	6.95	6.25	5.45
Elastic loading time ($X10^{-8}s$)	t_E	5.05	4.56	5.36	5.75
Total contact time ($X10^{-7}s$)	t_c	1.0	0.912	1.07	1.15
Sliding distance ($X10^{-7}m$)	d	3.5	3.2	3.73	4.0
Frictional work ($X10^{-7}J$)	W_f	6.0	2.3	4.1	2.3
Thermal diffusion distance ($X10^{-6}m$)	x_e x_t	1.94 1.96	5.39 1.86	2.01 2.53	2.08 0.675
Mass of material heated ($X10^{-14}kg$)	m_e m_t	6.1 6.1	105 5.38	6.8 10.9	7.2 0.108
Temperature rise (K)	ΔT	6150	210	3361	3876
Melting temperature of target (K)	T_m	2072	2072	1830	2800
Initial Kinetic Energy ($X10^{-6}J$)	KE_1	1.67	1.34	1.67	1.67
Rebound velocity (m/s)	v_r	32	36	35	37
Melting observed		Yes	Yes	Yes	No

The frictional work absorbs only a fraction of the initial kinetic energy of the particles and realistic rebound velocities are estimated. Hutchings and Levy (42) assume in their analysis of plastic heating that all of the initial kinetic energy of the particles is dissipated as plastic heating and that the particles have zero rebound velocity.

The calculations indicate that the impact of alumina particles on alumina and Syalon results in temperature rises in excess of the melting points. Alumina particles are of a similar hardness to these target materials and do not induce a large amount of plastic deformation and it is therefore unlikely that the melting features seen in these erodent/target combinations arise from plastic heating. Thus it is probable that the melting features seen in the eroded surfaces are due to frictional heating.

A negligible temperature rise is estimated for the impact of silicon carbide particles on alumina, suggesting that the melting features seen in these impact sites cannot be accounted for by frictional heating and must therefore be due to plastic deformation.

No melting features were seen in the impact sites of the softer MgPSZ although a temperature rise in excess of the melting point has been estimated for both frictional heating and heating due to plastic deformation. Prior to melting the monoclinic phase must undergo a reverse m-t transformation and heat energy is absorbed as latent heat of transformation. The transformation temperature is approximately 800-1000ºC depending on the amount of magnesia and the latent heat of transformation is 1.42 kcal /mol (70).

The latent heat of transformation for the mass of material heat during frictional heating has been calculated below. It is assumed that the material in the impact zone is purely monoclinic.

Mass of MgPSZ heated = 1.08×10^{-13} kg (from Table 6.4)
Latent heat of transformation = 48.3 kJ/kg
Energy absorbed by transformation = 5.2×10^{-9} J
Energy available for heating = 2.2×10^{-7} J
Maximum temperature rise = 2030 K
Melting Temperature = 2800 K

Thus the maximum temperature rise is lower than the melting temperature when the latent heat of transformation is taken into account and would explain the

absence of melting features in the MgPSZ specimen. In addition to this, the heat capacity and conductivity increase with increasing temperature (70) and therefore the thermal diffusion distance has been underestimated.

The transformation of the monoclinic phase on heating will cause a recovery process similar to the tempering of metals and would be expected to alter the surface layer. There is a 3-5% volume reduction for the m-t transformation which would result in a residual tensile surface stress and a decrease in toughness. TZP also has a small proportion of monoclinic grains in the deformed surface layers and would be similarly affected.

THE COMBINED THERMOMECHANICAL EFFECTS

The melting features appear to be confined to a thin surface skin and it is probable that heating arises from a combination of friction and plastic deformation of the highly stressed asperity tips. A schematic representation of the most likely mechanism of thermomechanical heating is given in fig. 6.16.

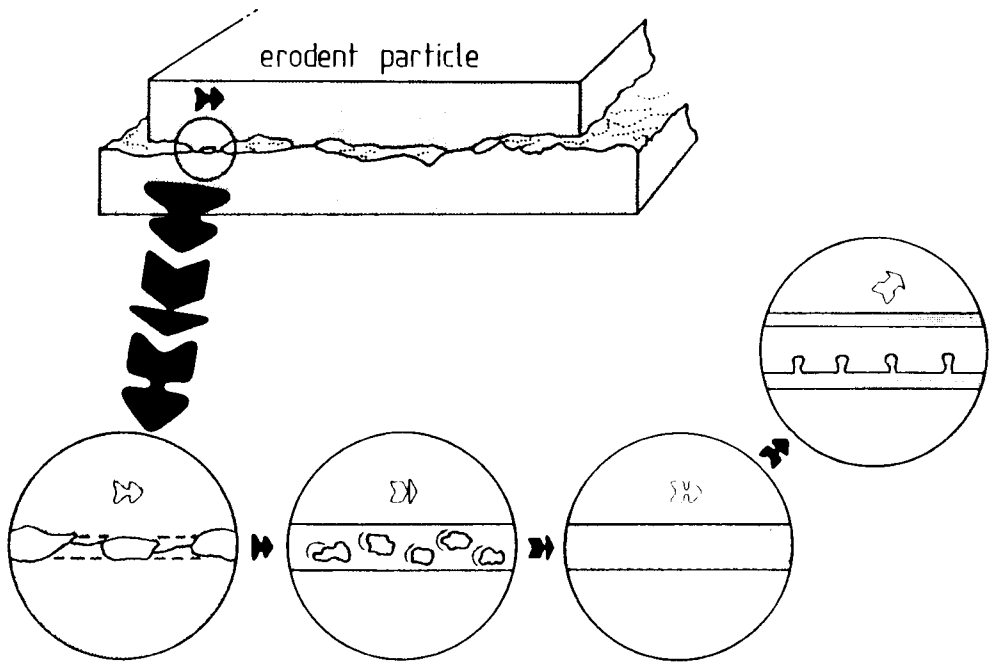

Figure 6.16 *A schematic representation the processes that occur when a softer erodent particle strikes a harder target surface and causes incipient melting of the target and erodent debris.*

On impact the particles slide across the target for a short distance. High contact stresses are generated at the asperity tips and the momentum of the particle causes shear of the asperity tips releasing erodent and target fragments resulting in three body abrasion, high frictional forces and plastic deformation of the debris.

Frictional and plastic work are dissipated as heat and cause melting. A viscous weld layer forms between the particle and the target, which adheres to the particle as it lifts off the surface, resulting in the formation of melting features.

When the erodent particles are much harder than the target material plastic deformation occurs preferentially in the target material and the melting features consist primarily of target debris and vice versa. When the erodent particles and the target material are of a similar hardness and the frictional coefficient is high, little plastic deformation occurs and melting is due to frictional heating.

The heat diffuses into both the target and erodent and the velocity of the heat front is determined by the thermal properties of both materials. If either material has a high thermal diffusivity the rate of heat conduction away from the impact zone will be rapid and the conditions will be isothermal.

It is interesting to note that melting features were seen only in TZP, Syalon and the three alumina targets. These target materials have a common microstructural feature in that they all contain glassy intergranular phases. It is conceivable that the combination of heating and the high compressive contact stresses causes flow of these phases to form a viscous layer between the particle and the surface and that melting of the crystalline ceramics never actually occurs.

LIGHT EMISSION

The low intensity light emitted by the target surfaces during solid particle erosion may be attributed to tribo-induced thermoluminescence. During particle impact frictional and plastic heating cause local hot spots on the target surface which glow red-hot.

The light emitted by the rebounding silicon carbide particles may be explained by the phenomena of triboluminescence (71) which is defined as the light emitted when a material is stressed to the point of fracture. The silicon carbide particles fracture on impact of harder materials and light is emitted due to a dielectric breakdown in the surrounding air as the particle fragments separate. The thermal diffusivity of silicon carbide is high and the rate at which heat is conducted away from the impact zone exceeds the rate at which it is dissipated due to plastic deformation and friction, and local heating cannot account for light emissions in rebounding silicon carbide particles.

CHAPTER SEVEN: CONCLUSIONS

Solid particle erosion in ceramic materials occurs by a process of dynamic elastic/plastic indentation and lateral fracture. The erosion of the ultrahard materials occurs by a complex mechanism of extrusion and plastic deformation of the softer phases and fracture and ejection of the harder crystallites. There is a concurrent weight gain due to the adhesion of plastically deformed particle debris and the embedment of particle fragments.

(a) When the erodent hardness is similar to the target hardness, the ease of lateral crack initiation is the controlling factor in erosion and the relative hardness of the target and particle are important:-

(i) When the erodent is slightly softer than the target material the zones of irreversible deformation are shallow, the residual driving forces for lateral crack propagation are small and the erosion rates are correspondingly low. There is a tendency for soft particles to deform or fracture on impact, the initial kinetic energy is apportioned between the particles and the surface and their ability to concentrate forces in the target surface and initiate fracture diminishes. Repeated impact may be required for damage initiation.

(ii) Hard particles are more likely to maintain their integrity on impact and more initial kinetic energy will be available for damage. The ability to concentrate stresses in the target surface and cause appreciable inelastic deformation to initiate fracture is greatly enhanced and there is a marked increase in the erosion rate.

(b) When the erodent particles are much harder than the target material lateral crack initiation is inevitable and relative hardness does not appear to be important. The particles maintain their integrity on impact and the plastic zones size and residual driving forces remain similar for large changes in erodent or target hardness. The amount of lateral crack propagation becomes the prime controlling factor in erosion. The initial kinetic energy of the particles and their ability to concentrate the energy in the target surface will determine the potential extent of lateral fracture and dense sharp erodents will be most erosive. A material's ability to inhibit lateral crack propagation will determine its erosion resistance and this is ultimately effected by the

toughness, grain size and defect density. A tough, defect free microstructure with a small grain size will more resistant to erosion by very hard particles. Subsurface pores act as stress raisers and increase the ease of crack initiation and lateral fracture.

An ideal erosion resistant material should be harder than the erosive particles and have a high toughness and non-porous, fine grained microstructure. Ceramics, however tend to have low toughnesses and the ultrahard materials, consisting of hard randomly-orientated crystallites and soft tough binder phases offer the most resistance to erosion. TZP, with its high hardness and tough, fine grained microstructure, was found to be the most erosion resistant ceramic material.

Thermomechanical heating is thought to occur due to plastic deformation and friction of the asperity tips under high contact stresses. The maximum temperature rise is determined by amount of heat generated and the rate of heat conduction away from the impact zone. A soft particle striking a hard surface will deform and generate plastic heating and vice versa. When the relative hardness approaches unity the impact conditions are elastic and heating is due to frictional work. The amount of heat generated will depend on the target and erodent hardness, the frictional coefficient and the loading pressures. The rate of heat conduction is determined by the diffusivities, heat capacities and densities of the target and erodent materials. The ultrahard materials and the silicon carbide and diamond erodent particles have high conductivities, heat is rapidly conducted away from the impact zones and no melting occurs.

Thermomechanical heating may cause enhanced plasticity in the impact zones and increase the erosion rates of ceramic materials. Heating may cause monoclinic to tetragonal transformation in the surface layers of MgPSZ and TZP and recovery of work hardened Syalon.

REFERENCES

1 Preece, C.M., and Macmillan, N.H., Ann. Rev. Mat. Sci., 7, (1977), 95-121.

2 Fan, J., Zhou, D., Jin, J., and Cen, K, Wear, 142, (1991), 171-184.

3 Lheude,E. P., and Atkin, M. L., Rep. ARL/ME III, Dept. Supply, Aust. Defense Sci. Serv, (1963).

4 Hibbert, W. A., J. Roy. Aero. Soc., 69, (1965), 769-776.

5 Neilson, J. H., and Gilchrist, A., Wear, 11, (1968), 111-122, 123-143.

6 Raask, E., Wear, 13, (1968), 301-31.

7 "Conducting Erosion Tests by Solid Particle Impingement using Gas Jets", ASTM, G76, (1983), American Society for Testing and Materials, Philadelphia.

8 Finnie, I, Wear, 3, (1960), 87-103.

9 Bitter, J.G.A., Wear, 6, (1963), 169-190.

10 Tilly, G.P., Wear, 23, (1973), 87-96.

11 Levy, A.V., Wear, 108, (1986), 1-21.

12 Bellman, R., and Levy, A.V., Wear, 70, (1981), 1-27.

13 Ponton, C.B., and Rawlings, R.D., Mat. Sci. and Tech., 5, (1989), 865-872.

14 Lawn, B.R., and Marshall, D.B., "Indentation fracture and strength degradation in ceramics", 205-229.

15 Doyle, R.A., MSc. Thesis, University of Cape Town, South Africa, (1989).

16 Head, W.J., and Harr, M.E., Wear, 15, (1970), 1-46.

17 Brown, R., and Edington, J.W., Wear, 73, (1981), 193-200.

18 Sarkar, A.D., Wear, 87, (1983), 173-180.

19 Vaughan, R.A., and Ball, A., Wear of Materials Proc., ASME, Vol. 1, Ludema, K.C., and Bayer R.G. (eds.) (1991), 71-75.

20 Quadir, T., and Shewmon, P., Metall. Trans., 12(A), (1981), 1163-1176.

21 Doyle, R.A, and Ball, A., "Thermomechanical Effects of Erosion", to be published in Wear, Nov. (1991).

22 Hutchings, I.M., and Levy, A.V., Wear, 131, (1989), 105-121.

23 Yust, C.S., and Crouse, R.S., Wear, 51, (1978), 193-196.

24 Ball, A, Wear, 91, (1983), 201-207.

25 Field, J.E., and Hutchings, I.M., "Materials at High Strain Rates", E Blasynski, (ed.), Elsevier Applied Science Publishers Ltd., Essex, England, (1987), Chap. 7.

26 Tilly, G.P., Treatise on Mat. Sci. and Tech., 13, (1979), 287-319.

27 Raask, E., Transactions of ASME, 104, (1982), 858-866.

28 Srinivasan, S., and Scattergood, R.O., Wear, 128, (1988), 139-152.

29 Srinivasan, S., Russ, J.C., and Scattergood, R.O., J. Mat. Res., 5(11), (1990), 2616-2619.

30 Wiederhorn, S.M., and Lawn, B.R., J. Am. Cer. Soc., 62(1-2), (1979), 66-70.

31 Glover, G, PhD dissertation, University of Cape Town, South Africa, (1980).

32 Cook, R.F., and Clarke, D.R., Acta. Metall., 36(3), (1988), 555-562.

33 Srinivasan, S., and Scattergood, R. O., Wear, 142, (1991), 115-133.

34 Marshall, D.B., and Swain, M.V., J. Am. Cer. Soc., 71(6), (1988), 399-407.

35 Cho, S-J, Hockey, B.J., Lawn, B.R., and Bennison, S.J., J. Am. Cer. Soc., 72(7), (1989), 1249-1252.

36 Krstic, V. D., J. Mat. Sci., 23, (1988), 259-266.

37 Levy, A, V, and Chik, P, Wear, 89, (1983), 151-162.

38 Shewmon, P., Wear, 68, (1981), 253-258.

39 Zhou, J. R., and Bahadur, S., Wear, 132 (1989), 235-246.

40 Bahadur, S., and Badruddin, R., Wear, 138, (1990), 189-208.

41 Marshall, D.B., Evans, A.G., Gulden, M.E., Routbort, J.L., and Scattergood, R.O., Wear, 71, (1981), 363-373.

42 Hutchings, I. M., J. Phys. D:Appl. Phys., 10, (1977), L179-L184.

43 Lawn, B.R., and Wilshaw, R., J. Mat. Sci., 10, (1975), 1049.

44 Wiederhorn, S.M., Lawn, B.R., and Hockey, B.J., J. Am. Cer. Soc.,62(11-12), (1979), 639-640.

45 Scattergood, R.O, and Routbort, J.L., Comm. Am. Cer. Soc., (1983), C184-C186.

46 Dosanjh, S., and Humphrey, A. C., Wear, 102, (1985), 309-330.

47 Crowder, R. S., Daily, J. W., and Humphrey, J. A. C., Journal of Pipelines, 4, (1984), 159-169.

48 Tabakoff, W., Hamed, A., and Beacher, B, Wear, 86, (1983), 73-88.

49 Laitone, J. A., Wear, 56, (1979), 239-246.

50 Pourahmadi, F., and Humphrey, J.A.C., PCH PhysicoChemical Hydrodynamics, 4(3), (1983), 191-219.

51 Tabor, D, "The Hardness of Materials", Clareddon Press, Oxford, England, (1951), 132.

52 Hannink, R.H.J.,Murray, M.J., and Scott, H.G., Wear, 100, (1984), 355-366.

53 Evans, A.G., and Heuer, A.H., J. Am. Cer. Soc., 63(5-6), (1981), 241-248.

54 Scott, H.G., J. Mat. Sci., 10, (1975), 1527-1535.

55 Cother, N.E., Materials and Design, 8(1), (1987), 2-5.

56 Fukuura, I., and Asano, T., "Fine Ceramics", Saito, S. (ed.), Elsevier Applied Science Publ., (1985), 165.

57 Pipkin, N.J., Roberts, D.C., and Wilson, W.I., "Ultrahard Materials Applications and Technology", Paul Daniel (ed.), De Beers Industrial Diamond Division (publ.), Berkshire, England, (1982), 72.

58 Juchem, H., Ind. Diamond Rev., 51(542), (1991), 10-13.

59 Clinton, D.J., "A Guide to Polishing and Etching of Technical and Engineering Ceramics", Institute of Ceramics (publ.), Stoke-on-Trent, England, (1986).

60 Evans, A.G., and Charles, E.A., J. Am. Cer. Soc., 59(7-8), (1976), 371-372.

61 Hall, C.,"Polymer Materials: An Introduction for Technologists and Scientists", The MacMillan Press, London, England, (1981), 84.

62 Ruff, A.W., and Ives, L.K., Wear, 37, (1975), 195-199.

63 Hovis, S.K., Talia, J.E., and Scattergood, R.O., Wear, 108, (1986), 139-155.

64 Rice, R.W., Adv. Cer., 22, (1988), 3-56.

65 Lawn, B.R., Evans, A.G., and Marshall, D.B., J. Am. Cer. Soc., 63(9-10), (1980), 574-581.

66 Koenig, W., and Boemcke, A., Fresenius Z. Anal. Chem., 333, (1989), 461-465.

67 Feng, Z. and Field, J.E., "Erosion of Diamond, Syndite and Amborite by Sand Particles", to be published in J. Hard Mat.

68 Forse, C. and Ball, A., "Solid Particle Erosion in Hydraulic Machinery", Proc. 6th Int. Conf. on Erosion by Liquid and Solid Impact, (1983), 61-1.

69 Doyle, R.A., and Ball, A., EMSSA Proc., Durban, (1988).

70 Stevens, R., "An Introduction to Zirconia", Magnesium Elektron (publ.), (1986).

71 Walton, A.J., Advances in Physics, 26(6), 887-948.

72 Wada, S., Watanabe, N., and Tani, T., J. Cer. Soc. Jpn. Edn., 96, (1988), 737.

73 Lankford, J., and Davidson, D. L., J. Mat. Sci, 14, (1979), 1661.

APPENDIX 1

INDENTATION TOUGHNESS MEASUREMENT

Indentation fracture toughness may be calculated from the average radial crack lengths radiating from the corners of an indentation as measured in an optical microscope. The ultimate cracks lengths are strongly dependent on the surface finish and the presence of microstructural flaws. The indentation crack systems were assumed to be of median half-penny geometry and toughness was calculated according to the method of Evans and Charles (60, 13).

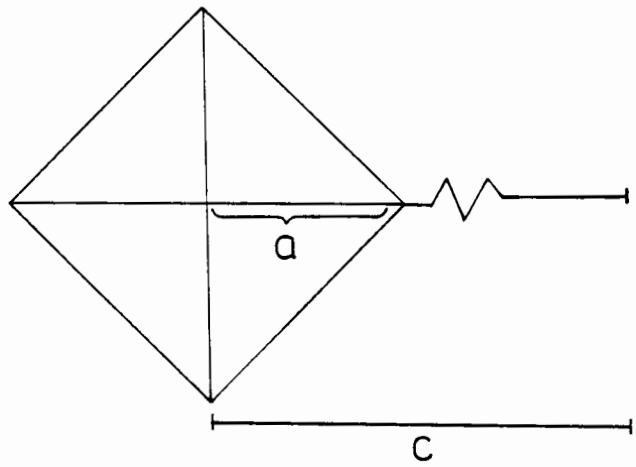

Figure A1

For values of $c/a > 2$, the indentation toughness (K_{IC}) in $MNm^{-3/2}$ and Vickers Hardness (H_V) are calculated as follows:-

$$K_{IC} = 0.1777\ H_V\ a^2/c^{3/2}$$

$$K_{IC} = 0.0824\ P/c^{3/2}$$

$$H_V = 4.636\ P/a^2$$

where P is the indentation pressure in kgf and, a and c are defined in fig. A1.

APPENDIX 2

PARTICLE VELOCITY CALIBRATION

The double rotating disk method of Ruff and Ives (62) was used to calculate the average particle velocity (fig. A2.1).

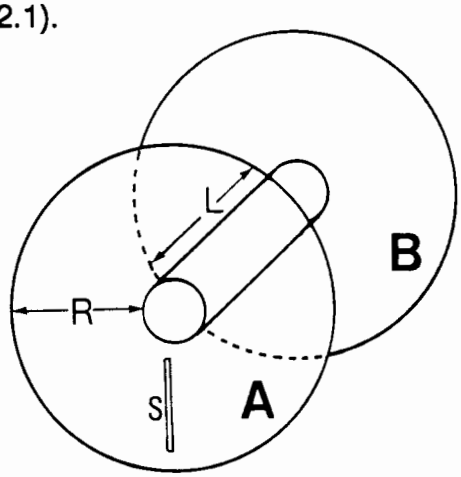

Figure A2.1 *A schematic diagram of the double rotating disk apparatus developed by Ruff and Ives (62).*

The average particle velocity (v_a) is calculated as:-

$$v_a = 4\pi\omega rL/X$$

where r is the radius from the disk center
ω is the rotational velocity of the disk
X is the linear separation of the two marks
and L distance between disk A and B.

The time of flight, and hence the velocity of the particles between the disks, A and B, is calculated from the difference in the angular velocity of two erosion exposures and the resultant angular separation of the two erosion marks.

The average particle velocities of the alumina and silicon carbide erodent particles were measured for air pressures of between 100 and 300 kPa (Table A2). Difficulty was encountered in measuring the separation of the erosion marks of the silica particles, due to their low erosivity, and the CDA diamond particles, due to their high erosivity, because of extensive overlap in the erosion marks. The air stream pressure corresponding to a particle velocity of 40 m/s was assumed to be similar for all the erodent particles.

Table A2 **The average particle velocities of the alumina and silicon carbide erodents as measured by the double rotating disk method (Ruff and Ives 62).**

	Air pressure (kPa)				
Average particle velocity (m/s)	100	150	200	250	300
Alumina	30.4	37.8	46.3	56.0	67.0
SiC	30.0	40.0	53.2	65.0	80.0

The average particle velocity was found to vary linearly between the limits of 100-300 kPa air pressure (fig. A2.2).

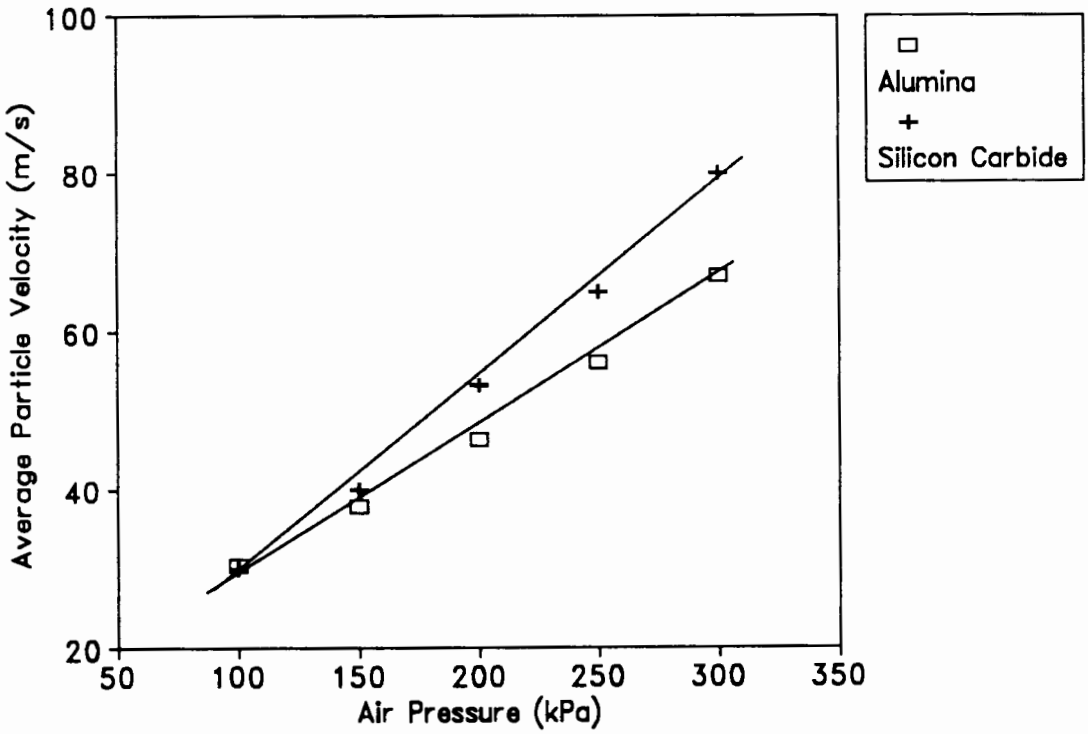

Figure A2.2 *The variation of particle velocity with air pressure for the alumina and silicon carbide erodent particles.*

APPENDIX 3

REPEATABILITY TEST

At the start of the experimental work a repeatability test was performed on two polished specimens of MgPSZ. The specimens were subjected to erosion by 100 micron silicon carbide grit under standard conditions. The cumulative mass loss was plotted for both specimens and the results were compared.

Table A3 **The cumulative mass losses of two MgPSZ specimens (a&b) after erosion by SiC under standardised conditions.**

Mass of SiC used (g)	Cumulative mass loss (a) $X10^{-5}g$	Cumulative mass loss (b) $X10^{-5}g$
0.00	0.00	0.00
5.00	25.00	25.00
10.00	47.00	36.00
15.00	73.00	86.00
20.00	91.00	108.00
25.00	135.00	140.00
30.00	164.00	161.00
35.00	198.00	201.00
40.00	221.00	223.00
45.00	257.00	250.00

A correlation coefficient of 0.994 was obtained for both specimens from a plot of mass loss of target as a function of mass of erodent used (fig. A3). There was a maximum variation of less than 4% between the two samples.

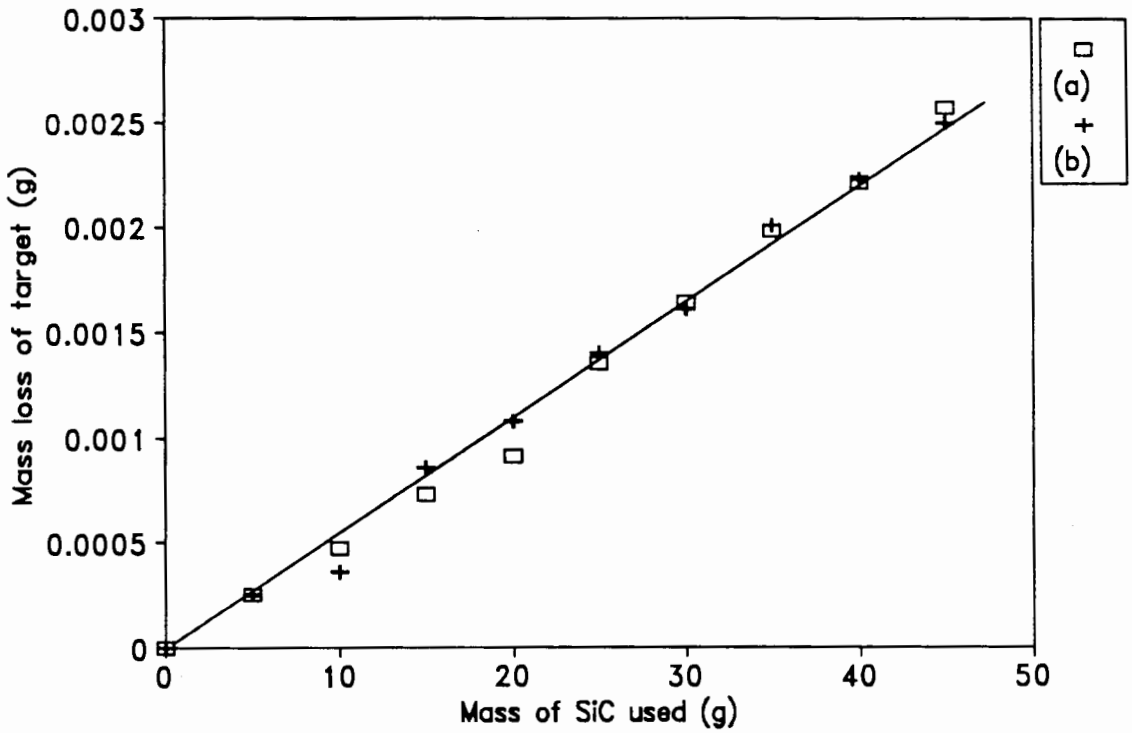

Figure A3 *The cumulative mass loss of two MgPSZ specimens subjected to erosion by silicon carbide erodent particles.*

APPENDIX 4

THE EFFECT OF IMPACT ANGLE ON EROSION

The variation in erosion rate with impact angle was compared for MgPSZ and 432 stainless steel. Tests were performed for angles of 30, 60 and 90° and an airstream pressure of 250 kPa using 120 grit silicon carbide particles. The results are listed in Table A4.

Table A4 **The volumetric erosion rates for MgPSZ and stainless steel for varying erosion angles.**

Impact Angle	Volumetric Erosion rate ($X10^{-5}$ cm^3/g)	
(°)	MgPSZ	Steel
30	0.68	3.37
60	3.18	5.57
90	8.51	3.47

The ceramic target material, MgPSZ, has a maximum erosion rate at normal impact and the metallic target, 431 stainless steel, has a maximum erosion rate at 60° (fig. 4A).

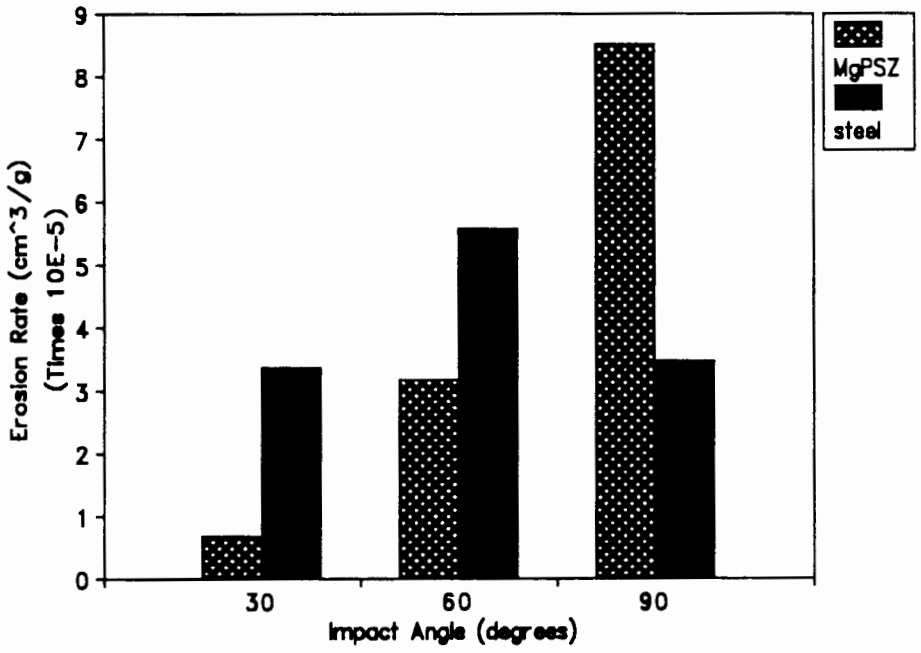

Fig. 4A *The volumetric erosion rates of MgPSZ and steel plotted against the impact angle.*